Mathematical Modelling of the Spatial Dynamics of Oncolytic Viruses in Cancer Tissue

by

Arwa Abdulla Baabdulla

A thesis submitted in partial fulfillment of the requirements for the degree of

Doctor of Philosophy

in

Applied Mathematics

Department of Mathematical and Statistical Sciences
University of Alberta

Abstract

In this thesis, we explore the spatial dynamics of viral infection within tissue through mathematical modeling, aiming to understand the impact of virus spread on both cancerous and healthy tissue. Specifically, we investigate how spatial patterning and heterogeneity influence viral infection levels. Our primary focus is on oncolytic viruses in cancer tissue, where viruses are employed to directly target and eliminate cancer cells while also stimulate the immune system to target virus-infected cells, thereby eradicating cancerous tissue.

In Chapter 2, we employ the Fisher-KPP reaction-diffusion model and the homogenization method to investigate spatial dependencies within virus load data obtained from a checkerboard experiment. Our analysis of the impact of spatial complexity among heterogeneous populations on viral load is based on the application of an innovative cell-printing method introduced by Hesung Now, Ju An Park, Woo-Jong Kim, Sungjune Jung, and Joo-Yeon Yoo. Contrary to a simplistic arithmetic summation of individual cellular activities, our model analysis, confirmed by experimental results, reveals a more intricate relationship in total virus load. Notably, our model not only elucidates observed virus load data but also predicts values not captured in experiments. Furthermore, we employ numerical techniques to examine the spatial distribution of viral load across the periodic domain using our mathematical model. This analysis illustrates how spatial heterogeneity influences cell responses to virus infection, emphasizing the importance of considering spatial arrangement rather than extrapolating measurements solely from isolated cell populations to heterogeneous mixtures of cells.

In Chapters 3 and Chapter 4, we investigate viral spatial oscillation patterns in cancer tissue resulting from a Hopf bifurcation, exploring their clinical relevance and intricate characteristics. Our analysis involves a bifurcation study of a spatially explicit reaction-diffusion model aimed at uncovering spatio-temporal patterns in virus infection. We consider two types of virus-tumor interactions: mass-action (Chapter 3) and Michaelis–Menten kinetics (Chapter 4). The desirable pattern for tumor eradication is the hollow ring pattern, and we identify precise conditions for its occurrence. Furthermore, we determine the minimum speed of traveling invasion waves for both cancer and oncolytic viruses. Our 2-D numerical simulations unveil complex spatial interactions in virus infection, revealing a novel phenomenon characterized by periodic peak splitting in mass-action case.

In Chapter 5, we probe into the oncolytic potential of the reovirus, specifically examining both the wild type T3wt and its mutated variant, SV5. Through in vitro experiments, SV5 demonstrates superior capabilities in spreading within cancer cell cultures, resulting in larger plaque sizes in cell monolayer experiments compared to T3wt. A significant contributing factor to this enhanced performance lies in the reduced binding affinity of SV5 to cells compared to T3wt. To comprehend the interplay between the binding process and virus spread for both variants, we employ a reaction-diffusion model. Our computational results reveal the presence of an optimal binding rate corresponding to an optimal viral invasion wave speed, influencing the overall spread of the virus. This identification provides a rationale for the observed larger plaque size in SV5. Additionally, we investigate the impact of burst size and binding rate on plaque size, revealing the optimal binding rates corresponding to each burst size. This underscores the significance of burst size alongside binding rate, emphasizing that the role of burst size is crucial and cannot be overlooked.

We close with a conclusion (Chapter 6), where we evaluate our results in the context of current scientific development and hint at ideas for future studies.

Preface

The results in Chapter 2 of this thesis have been published in

- A.A. Baabdulla, J.A. Park, W.J. Kim, S. Jung, Yoo, J.Y. Yoo and T. Hillen. Homogenization of a reaction diffusion equation can explain influenza A virus load data. *Journal of Theoretical Biology*, 527:110816, 2021.

with collaboration with Hesung Now, Ju An Park, Woo-Jong Kim, Sungjune Jung and Joo-Yeon Yoo (Pohang University of Science and Technology, Republic of Korea). I was responsible for the formal analysis, methodology, visualization, writing, submitting the manuscript, manuscript editing, and final manuscript approval . Hesung Now, Ju An Park, Woo-Jong Kim, and Sungjune Jung were responsible for data curation. Joo-Yeon Yoo generated the concept of the experiment, participated in the data curation and research support funding. Thomas Hillen participated on the mathematical theory, the formal analysis, support funding, methodology, project administration, resources, writing and manuscript editing.

Parts of Chapter 3 have been published in

- A.A. Baabdulla, and T. Hillen. Oscillations in a Spatial Oncolytic Virus Model. *Bulletin of Mathematical Biology*, 86:93, 2024.

The results in Chapter 5 are based on data collected by Francisca Cristi and Maya Shmulevitz. A manuscript of Chapter 5 is ready for submission to PLOS ONE.

If you set your goals ridiculously high and it's a failure, you will fail above everyone else's success.

– *James Cameron.*

Life is either a daring adventure or nothing at all.

– *Helen Keller.*

I extend my dedication in this thesis to my mother and to my dad's memory, in recognition of their unconditional love. Furthermore, my children, Hind, Khaled, and Sara, as well as my husband, who have been constant sources of inspiration and motivation throughout this scholarly endeavor.

Special acknowledgment is extended to my esteemed colleagues at the United Arab Emirates University, with particular gratitude directed towards Dr. Mohammed Salim and Dr. Mohammed Syam for their valuable contributions and guidance.

Ultimately, this thesis is dedicated to the Almighty Allah, who endowed me with the strength, knowledge, and wisdom required to navigate the challenges inherent in my academic pursuits.

Acknowledgements

I extend my sincere gratitude to my supervisor, Dr. Thomas Hillen, whose unwavering support and guidance have been instrumental in deepening my understanding of my research and fostering the generation of innovative ideas. His encouragement, patience, and enthusiasm played a crucial role in navigating through challenging phases in my research. Without his efforts, the successful completion of my PhD research would not have been possible.

I would also like to express my profound appreciation for the valuable considerations, suggestions, and the time invested by Dr. Gerda de Vries and Dr. Jay Newby as members of my thesis committee. I also extend my sincere gratitude to Dr. Dominik Wodarz for graciously agreeing to serve as an external examiner.

The support and financial resources provided by the United Arab Emirates University are gratefully acknowledged. I extend my thanks to all the professors at the University of Alberta who imparted their knowledge during my PhD studies.

Lastly, I am indebted to the encouragement and support received from friends, colleagues, and my family, particularly my mother and my husband, without whom this academic journey would not have been as enriching and fulfilling.

Table of Contents

List of Tables

List of Figures

Chapter 1

Introduction

1.1 Background and Motivation

Cancer is a major global health concern and a leading cause of death of about 10 million in 2020 [1]. Cancer is a complex group of diseases characterized by the uncontrolled growth and spread of abnormal cells, leading to the formation of tumors or the invasion of nearby tissues [2]. Therefore, cancer is considered as a complex and devastating disease that requires extensive multidisciplinary research. The complexity of cancer process makes it hard to understand the tumor dynamics based on the experimental data alone.

Many therapies have been developed over the last decades including radiotherapy [3], chemotherapy [4], surgery [5], immunotherapy [6] and virotherapy [7–10]. Compared to the conventional treatments that cause normal cell death as well as cancer cell death, new strategies have been developed to overcome this issue. Oncolytic virotherapy is considered one of the new promising target therapies. Oncolytic viruses selectively attack cancer cells and replicate rapidly inside them, thereby inducing tumor cell lysis. Hence, the new virions infect the neighborhood cells and triggering the anti-cancer immune response. Moreover, virotherapy treatment can be used in combination with traditional treatments at different treatment stages with other targeting therapies such as immunotherapy and radiotherapy [11–14].

Simultaneously, viewing mathematics as the language of complex systems, exten-

sive mathematical and computational modeling has been conducted to illuminate cancer formation and treatment. These models have been utilized in various cancer therapies [15–27].

In this thesis, we are interested in analyzing the viral infection pattern in cancerous and healthy tissue using reaction diffusion models. As cancer is spatially heterogeneous (Figure 1.1 (A)), considering the spatial effect will lead to a more realistic model and provide useful information leading to a better understanding of the tumor-virus dynamics.

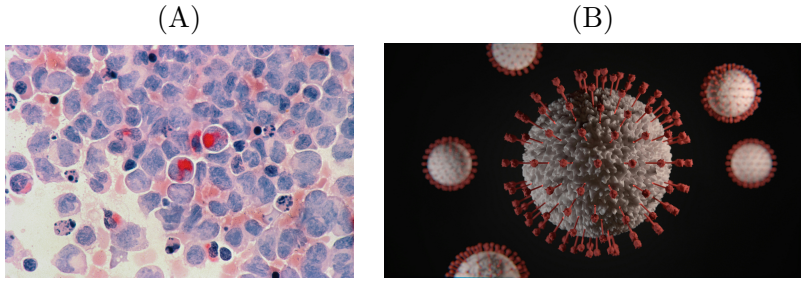

Figure 1.1: An example of cancer cells and a virus particle. **(A)**: Cancer cells in a tissue indicated by red color and **(B)**: COVID-19. Source: https://unsplash.com.

1.1.1 Oncolytic Virotherapy

A virus is a small infectious agent that replicates only inside the living cells of an organism [28–30]. Viruses can infect all types of life forms, from animals and plants to microorganisms, including bacteria and archaea. They are very small and are measured in nanometers. A virus consists of genetic material (either DNA or RNA) enclosed in a protein coat called a capsid. Some viruses also have an outer envelope composed of lipids.

Viruses cannot carry out metabolic processes or replicate on their own. Instead, they rely on the host cells of living organisms to replicate and reproduce [31–33]. Once inside a host cell, viruses hijack the cellular machinery to produce more virus particles. This often leads to damage or death of the host cell. The viral infection

and replication inside the cells is a multilayered processes. First, virions enter the cell through endocytosis. Then, after virion uncoating, the virus (either DNA or RNA) replicates and is reassembled into new virions. Virions are released through a number of processes, such as exocytosis and cell lysis. The number of new virions released from one infected cell is called "*burst size*". In the case of lysis the cell membrane breaks down, releasing virions into the extracellular fluid as shown in Figure 1.2.

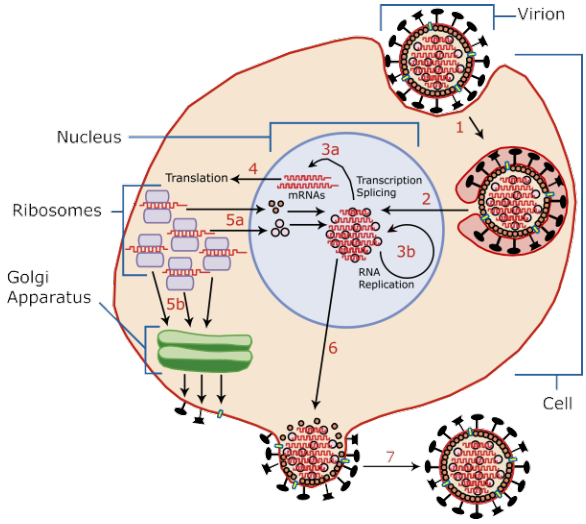

Figure 1.2: An example of virus replication cycle: Step 1: Binding, Step 2: Entry Step, 3: Complex formation and transcription, Step 4: Translation, Step 5: Secretion, Step 6: Assembly and Step 7: Release. Source: https://en.wikipedia.org/wiki/Viral_life_cycle.

Indeed, viruses can have dual roles in our interactions with them. While some viruses, like SARS-CoV-2, which causes COVID-19 (Figure 1.1 (B)), can lead to severe illness and have a significant impact on public health [34], others can be harnessed for therapeutic purpose like virotherapy. Virotherapy is a striking example of how understanding and manipulating viruses can lead to both harmful and beneficial outcomes in the realm of human health. Oncolytic virotherapy was inspired by clinical observations of tumor remissions after natural virus infections [35], prompting further investigation by clinicians and researchers [36, 37]. This opens the door to employing a diverse array of viruses as oncolytic agents for various cancer treatments, including glioma, head and neck, pancreatic, breast cancer, melanoma, cervical, lung carcinoma,

ovarian, and prostate cancers [38, 39].

Clinical trials have employed various oncolytic viruses, including adenovirus [40–43], herpes simplex virus [44, 45], vaccinia virus [46], measles virus [47], reovirus [48–53], and vesicular stomatitis virus (VSV) [54]. Preclinical studies, employing in vitro and in vivo models, have been conducted to assess the safety and efficacy of these genetically modified viruses [10, 55]. However, only two types have obtained licensing for anti-cancer treatments. Shanghai Sunway Biotech introduced adenovirus H101 for treating head and neck cancer in 2005 [56], while the U.S. Food and Drug Administration and European Medicines Agency approved herpes virus talimogene laherparepvec (T-VEC) for advanced melanoma treatment in 2015 and 2016, respectively [57].

The main goal in cancer treatment is tumor control or tumor extinction. However, even with the advances in the pre-clinical and clinical trial results, analyzing and understanding the dynamics of tumor-virus interactions has proven to be difficult by experimentation alone. There are many challenges that virotherapy treatment faces to achieve the best results [58, 59]. For example, what is the balance of antiviral versus anti-tumor immunity? How can combination schedules and doses be optimized to achieve maximum anti-tumor efficacy? What is the best protocol design based on tumor type and oncolytic virus type? How does the spatial distribution of tumor and virus impact viral propagation and tumor control? Answering these questions is time consuming, expensive, and sometimes hard to address experimentally. Mathematical modelling can accelerate the progress of oncolytic virotherapy research by identifying crucial parameters, generating new hypotheses to be tested experimentally, predicting therapeutic outcomes in silico, and optimizing combined treatments.

It is noteworthy that the predominant focus in mathematical modeling has been on the temporal dynamics of tumor-virus or tumor-virus-immune interaction, primarily due to the availability of temporal data. Several of these models rely on ordinary differential equations [60–68], while alternative models are constructed based on delay differential equations [69–73]. Other types of models have been considered, including

a multi-scale model [74, 75] and a stochastic model [76–78].

Fortunately, recent advancements in intravital imaging and viral plaque analysis have contributed valuable data on the spatial spread of tumors and viruses [79, 80]. Numerous experimental studies [79–82] emphasize the significance of spatial distribution in viral proliferation and spread within host cells, leveraging imaging techniques and viral plaque analysis. Consequently, the impact of spatial distribution, both in vitro for tumor-virus and in vivo for tumor-immune-virus interactions, cannot be disregarded. As a result, several spatio-temporal models have been developed to comprehend the spatial dynamics of oncolytic viruses in cancer treatment [74, 75, 81–92].

1.1.2 Modelling Oncolytic Virotherapy

The interest in applying mathematical modeling to virotherapy treatment began in 2001. Among the earliest mathematical models exploring the control of tumors while incorporating spatial tumor-virus dynamics is the work of Wu et al. [83]. In their study, a radially symmetric partial differential equation (PDE) system with a moving boundary condition was formulated to characterize the spatial distribution of ONYX-015 adenovirus and tumor cells. The tumor cells were categorized as uninfected, infected, and necrotic cells. The findings revealed that, for effective tumor control, a threshold condition should be met, contingent on the viral injection strategy. Subsequently, Wu et al. [84] expanded their initial model to account for the influence of the immune response. The results underscored the necessity of immunosuppressive drugs to suppress the immune response, enabling the virus to eliminate the tumor before the immune response becomes active.

In the same year, Wodarz [93] contributed to the field of oncolytic virotherapy with a publication that differed from Wu et al.'s [83] PDE model. Wodarz [93] introduced ordinary differential equation (ODE) models, presenting various scenarios to delineate conditions conducive to optimal virotherapy outcomes. The first scenario involves

tumor cells being killed by viral cytotoxicity, the second scenario entails infected tumor cells being eliminated through the response of cytotoxic T lymphocytes (CTL) against the virus, and the last scenario describes tumor cells being killed after the release of immunostimulatory signals, triggering a tumor-specific CTL response. The analysis of these models reveals the critical conditions regarding virus and tumor cell characteristics required for successful treatment. Notably, key parameters for achieving tumor extinction include the death rate of infected cells, tumor growth rate, virus replication rate, and antiviral CTL response. An optimal value for the death rate of infected cells is identified, and around this value, the maximum reduction in tumor size can be achieved. When this optimal death rate of infected cells is associated with slow tumor growth and a fast virus replication rate, the likelihood of tumor eradication is high.

Following the groundbreaking work of Wu et al. [84], Friedman et al. [82] developed a partial differential equation (PDE) model that incorporates the presence of an immunosuppressant drug. In addition to Wu et al.'s considerations, Friedman et al. [82] introduced innate immune cells in the tumor microenvironment, modeled virus diffusion as Brownian motion, and accounted for viral clearance by the immune system. The primary objective of this study was to investigate the impact of different drug protocols and the increase in viral burst size on tumor growth. The key finding by Friedman et al. [82] suggests that tripling the current viral burst size, coupled with the use of an immunosuppressant drug, can reduce the tumor diameter from 4mm to 1mm. This underscores the significance of the burst size parameter. The immunosuppressant drug is administered iteratively throughout the treatment to ensure the percentage of uninfected cells remains under control, thereby reducing the likelihood of cancer metastasis.

Due to the analytical challenges in solving the model proposed by Friedman et al. [82], Wang and Tian [94] developed a computational model to simulate tumor growth within the framework of Friedman et al.'s model. In their work, Wang and Tian

[94] assumed the tumor's dimension to be spherically symmetric. The computational results not only validated experimental data but also emphasized the significant importance of the burst size as a crucial parameter for achieving successful treatment in the presence of an immunosuppressant drug.

Wodarz and Komarova [95] led the way in introducing a comprehensive framework for depicting the kinetics of oncolytic virotherapy as a basis for experimental validation and model selection. In their model, virus particles were implicitly modeled under the quasi-steady state assumption. The dynamics were classified into two categories based on the position of infected cells. In cases where tumor populations are homogeneous, a specific viral replication rate exists at which the tumor can be effectively controlled. Conversely, when infected cells are clustered, the therapy outcome is contingent on the initial numbers of tumor cells and virus particles. The work of Wodarz and Komarova [95] serves as a foundational framework upon which more complex models can be constructed. Their pioneering efforts in elucidating the kinetics of oncolytic virotherapy provide essential insights and principles that can be expanded and refined in subsequent, more intricate models.

Recognizing the burst size as a pivotal factor in virus replicability and, consequently, virotherapy outcomes, Tian [66] conducted an analysis of the burst size's role through an ordinary differential equation (ODE) model. The analytical findings in Tian [66] revealed two threshold values for the burst size parameter influencing the treatment outcome. Below the first threshold, the tumor grows to its carrying capacity, leading to treatment failure. Once the burst size surpasses the first threshold, a locally stable steady-state solution emerges. Upon reaching or surpassing the second threshold, the system enters the Hopf bifurcation region, where one or three families of periodic solutions exist. In this region, the tumor burden is reduced to an undetectable level.

In the quest to enhance the efficacy of oncolytic viruses, numerous mathematical models have been devised to scrutinize diverse aspects of the viral infection process.

These models delve into elements such as the viral lytic cycle and the cross-phase replication of the virus during different stages of the cancer cell cycle.

Wang, Tian, and Wei [71] introduce a novel mathematical model that expands upon the foundational framework for oncolytic virotherapy. This model incorporates the viral lytic cycle through the construction of a nonlinear system of delay differential equations. Two crucial parameters characterize the viral lytic cycle: the time period of the cycle and the viral burst size. The model unveils a noteworthy revelation regarding the interplay between the burst size and the critical value of the viral lytic cycle period, providing compelling evidence for the paramount importance of this parameter in determining the outcome of virotherapy. An extended model incorporating spatial effects is presented in [96].

Crivelli et al. [69] are pioneers in exploring the dynamics of viral infection and replication within cancerous cells across various phases of the cell cycle. They introduce systems of differential equations with time delays to model these processes. Through a detailed analysis and simulation of their proposed model, Crivelli et al. [69] elucidate the impact of changes in both the minimum cycling time and the parameters regulating viral dynamics on the stability of the cancer-free equilibrium.

Another factor investigated by Bhatt et al. [97] is the sensitivity of tumor cells to viral infection. Bhatt et al. [97], employed an immersed boundary method and a 2-D Voronoi and 3-D spatial interactions model. Bhatt and his colleagues [97] identified three primary reasons for treatment failures: a high death rate of infected cells, which is consistent with Wodarz result in [93], resulting in faster viral clearance; the emergence of virus-resistant cancer cells; and a viral spread rate that is too low. Understanding these factors is crucial for developing strategies to overcome virotherapy challenges and improve overall treatment effectiveness.

In addition to the factors previously discussed, Morselli et al. [91] highlighted the importance of considering the influence of spatial constraints and the tumor microenvironment on viral spread. They introduced a stochastic agent-based model to

investigate how these factors impact viral spread within solid tumors. The study encompassed two types of viral movements: undirected random movements and pressure-driven movements, and it explored how this choice influenced the outcome of virotherapy. The 2-D patterns observed in the agent-based model simulations conducted by Morselli et al. [91] were consistent with patterns previously observed in studies by Wodarz et al. [81] and Kim et al. [98]. This consistency reinforces the relevance of spatial patterns in comprehending the dynamics of virotherapy within solid tumors.

An intriguing model introduced by Paiva et al. [74] delves into the realm of virotherapy for cancer. Based on a multiscale approach and conducting extensive simulations, the model unveils undamped oscillatory dynamics within tumor cells and virus populations, highlighting the necessity for new quantitative experiments in vivo and in vitro to detect this oscillatory response. Additionally, considering the discrete and stochastic nature of cells and their responses, the model predicts an optimal range for viral cytotoxicity. Virotherapy may hinder if the oncolytic virus takes either too short or too long to eliminate the tumor cell. This suggests that the pursuit of viruses capable of rapidly destroying tumor cells may not necessarily translate to more effective control of tumor growth.

The first mathematical model for radiovirotherapy was developed by Dingli et al. [27]. Their model demonstrated that a combined treatment approach involving virotherapy and radiation yields more successful outcomes compared to virotherapy alone. The study identified an optimal window for radio-iodine administration and an optimal dose to achieve the best results. Interestingly, the results indicated that increasing the viral dose does not provide substantial benefits. Moreover, Dingli et al.'s [27] model revealed a novel observation in virotherapy dynamics that had not been reported in Wodarz's paper [99]. Specifically, the model exhibited lower equilibrium tumor burden associated with oscillations characterized by reduced damping and higher frequency. A unique dynamic behavior, termed a stable quasi-heteroclinic

cycle, was identified under specific parameter combinations. This cycle manifested as oscillations with sharp and limited growth of peaks in both tumor burden and viral population, followed by subsequent dips. Remarkably, the magnitude of these dips increased proportionally with the growth of the preceding peaks, and they eventually reached values smaller than one cell, suggesting the potential eradication of the tumor. While this dynamic behavior could signify a successful treatment strategy, the organism's ability to tolerate fluctuations in tumor burden and viral load becomes a critical factor for the efficacy of this therapeutic approach. The study underscores the need for further experimentation and analysis to validate and refine these findings, ensuring their applicability in real-world clinical scenarios.

In an effort to comprehend the underlying principles governing the spread of the virus within a target tumor cell population, Wodarz et al. [81] devised an agent-based model grounded in in vitro experiments of adenovirus conducted in a 2D setting of human embryonic kidney cells. The spatial dynamics were considered in a restricted domain, assuming that free viruses maintain a quasi-steady state. Experimental findings revealed three distinct spatial patterns: "*hollow ring structure* ", "*filled ring structure*", and "*dispersed patterns*." The computational model results emphasized that, for successful treatment, the hollow ring structure proved to be the most favorable pattern. This structure was associated with either the extinction of target cells or a low-level persistence of target cells.

Numerous mathematicians have drawn inspiration from these influential studies on the dynamics of oncolytic virotherapy, leading to increased attention on the mathematical modeling of virotherapy. Consequently, numerous papers have been dedicated to exploring and discussing the mathematical modeling of spatial virotherapy.

One of these mathematicians is Rioja. After four years of Wodarz agent-based model, Rioja et al. [70] developed a continuum version with a radial symmetry coordinate. In contrast to Wodarz et al.'s assumption of quasi-steady-state for free viruses, Rioja et al. [70] explicitly expressed virus dynamics and considered that

free viruses were not in quasi-steady state. Additionally, they assumed that infected cells remain stationary, and both susceptible tumor cells and free viruses decrease due to infection. The radial symmetry assumption in Rioja et al.'s model limited their analysis to radially symmetric patterns. The corresponding kinetic ordinary differential equation (ODE) system of Rioja et al.'s model was further studied in [66].

In 2021, Pooladvand et al. [88] introduced a spatio-temporal model capturing the dynamics of cancer-virus interactions, specifically adenovirus, within a solid tumor in 3-D spherical symmetric coordinates. In their model, Pooladvand et al. [88] incorporated the ability for susceptible cells, infected cells, and virus particles to move. Additionally, they accounted for the loss of free viruses due to infection of susceptible and infected cells.

The focus of Pooladvand and her colleagues [88] was on evaluating the impact of the infectivity parameter on treatment outcomes when the virus was injected at the center of the tumor mass. Bifurcation analysis was employed, and the results indicated that enhancing infectivity did not lead to complete eradication of the tumor. These findings align with experimental results, highlighting that virotherapy treatment alone may not be sufficient in many cases.

It was clear that from the previous studies, the negative impact of the adaptive immune response against the virus, which can lead to ineffective treatment. Therefore, infection of all tumor cells before the adaptive immune response is initiated is crucial to obtain an effective virotherapy treatment. From the observation on tumor patients, it showed that there is a window of 5-7 days before the accumulation of the adaptive immune response interferes with the viral spread leading the infection to wane. Okamoto, Priyanga, and Ian [65] used the *prey-predator apparent competition theory* and apply it in virotherapy treatment. This theory involves an indirect negative interaction between two prey species, namely normal cells and tumor cells, mediated by a common predator, which, in this case, is a virus. In this scenario, infecting normal cells with the virus leads to an increase in the virus population, sub-

sequently raising the likelihood of infecting tumor cells. The central inquiry becomes, "How can we maximize the infection of tumor cells while minimizing the infection of normal cells to achieve optimal virotherapy treatment?" To address this question, Okamoto et al. developed an ordinary differential equations model and applied it to three oncolytic viruses. The discovery suggests that viruses capable of infecting specific normal cells may offer a potential balance between the conflicting objectives of eliminating tumors and minimizing impacts on normal cell populations. This becomes particularly relevant when the infected tissues have the ability to regenerate. By tempering, rather than entirely eliminating, the capacity of oncolytic viruses to infect and lyse normal cells. While this idea may be intelligent, it's improbable to gain approval from health agencies due to the virus's ability to infect healthy tissues.

Given the undeniable significance of the immune response, various experimental studies have been conducted to explore its role, as documented in several works such as those by Bridle et al. [100], and Breitbach et al. [101], and Alemany et al. [102]. Based on the sequential treatment concept, Bridle et al. [100] designed an experiment using two viruses which carried the same tumor associated antigen. An adenovirus was used as a vaccine to trigger the immune response against the tumor antigen, while a vesicular stomatitis virus (VSV) was used as an oncolytic virus that boosts the anti-tumor immune response and kills the tumor. The results showed that the secondary immune response against tumor antigens dominated the response against viral antigens. However, this improvement was temporary as the tumor regrew. To reproduce similar results, Eftimie et al. [103] constructed an ordinary differential equations system based on two compartments of immune cells. The first compartment was lymphoid tissue which contains the effector and central memory immune cells. The second compartment was the peripheral tissue which contains the tumor cells (uninfected and infected) and the effector cells. A simplified version of the model was explored by Eftimie et al. [62] using only the lymphoid tissue compartment. Eftimie et al. focused their analysis on the role of the oncolytic virus (VSV) to study the

dynamics of a tumor-virus-immune system.

Another groundbreaking study was conducted by Storey et al. [68], where they developed an ordinary differential equation (ODE) framework model. This model aimed to explore the influence of innate and adaptive immune responses on virotherapy for glioblastoma multiforme, employing the Herpes Simplex Virus as the therapeutic agent.

In Storey at al. [68] model, the innate immune response serves as a first responder, attacking virus-infected cells and stimulating the adaptive immune system (T-cells). Storey et al. [68] observed that, under virotherapy alone, the innate immune system's virus clearance effect dominates, leading to rapid virus removal, while the impact of the adaptive immune response remains small. To enhance the adaptive immune response, a combination of virotherapy and immunotherapy in the form of a PD-1/PD-L1 inhibitor was considered. The PD-1/PD-L1 pathway, identified as a central mechanism allowing cancer cells to silence effector T-cells, was inhibited to prolong the activity of the adaptive immune response, resulting in a more potent effect on cancer cells. Storey et al. [68] clearly demonstrated the benefits of this combination therapy. Once again, Storey et al. [68] demonstrated findings analogous to those of Wu et al. [84].

In a subsequent study by Storey and Jackson [92], the model was extended to a spatially explicit agent-based model. The findings suggested that for effective treatment, the viral dose should be injected in the location with the highest tumor density rather than the tumor center. This spatial consideration added valuable insights to optimize the delivery of virotherapy in the presence of the immune system.

The incorporation of the innate and adaptive immune systems in the spatial cancer-virus therapy with moving boundary condition was first introduced by Timalsina et al. [104]. The utilization of a computational model has proven instrumental in exploring various scenarios, including investigating delays in the adaptive immune response, repeated viral doses, and the impact of varying model parameters. Key

parameters influencing the efficacy of virotherapy treatment include the burst size and adaptive immune killing rate, with increased values yielding significant improvements. Implementing regular intervals for viral dose repetition also contributes to enhanced treatment outcomes. It is worth noting that a prolonged delay in the adaptive immune response can have adverse effects on the long-term effectiveness of the treatment. However, a limitation of the model arises from the assumption of spherically symmetric geometry and the homogeneous nature of the tumor cell population, which may not fully capture the complexity of real-world scenarios.

Despite the remarkable findings from the aforementioned research, it is regrettable that many of the spatial models discussed above carry a substantial computational intensity, thereby constraining further exploration of their pattern-forming capabilities. In this thesis I am planning to go deeply into the analysis to determine the conditions that lead to these patterns in vitro. Furthermore, we consider the role of the binding process in the oncolytic viral spread in plaque size.

1.1.3 Goal of This Thesis

The primary goal of my thesis is to address inquiries concerning spatial viral infections and cancer treatment by employing mathematical modeling, with a specific focus on virotherapy. Considering the well-established spatial heterogeneity of cancer [105], the incorporation of spatial dynamics is crucial for developing effective treatment strategies. The interaction between cancer cells and virus particles resembles a prey-predator relationship, resulting in an oscillation pattern within the Hopf bifurcation region—a widely documented outcome [66, 88]. In a spatial context, these oscillations can give rise to various spatio-temporal phenomena, such as hollow-ring patterns, target patterns, and dispersed patterns. This thesis continues the systematic analysis of these spatial oscillations and explores their relevance in the clinical context.

In our capacity as mathematicians, we strive to employ mathematical approaches to address queries posed by biologists through the analysis of experimental data.

Additionally, we aim to formulate innovative hypotheses to optimize outcomes. For example, we investigate the impact of spatial and population heterogeneity on viral load and explore how the binding process in oncolytic viruses during viral spread in cell cultures can potentially lead to larger plaque sizes—a result that could enhance the potency of oncolytic viruses.

Given that many spatial models discussed in Section 1.1.2 predominantly involve computational frameworks, our focus shifts to examining viral infection patterns within healthy and cancerous tissue using a reaction-diffusion formulation. This methodology aims to identify the conditions for the most effective viral spread pattern.

In this thesis, I integrate methods from established research areas, including classical theories in reaction-diffusion systems such as invasion fronts (crucial for spatial analysis) and the homogenization method. Additionally, I incorporate the tumor control probability (TCP) technique, widely used in cancer treatment to measure the expected success of a given treatment when cancer cells are at an undetectable level. Since much of my work is based on experimental data, methods like the likelihood function and data fitting are utilized to estimate parameters in our models. In Section 1.2, I will elucidate the fundamental mathematical tools that have been utilized in my thesis.

1.2 Mathematical Tools

Within this section, I will delineate crucial definitions and methodologies that have been employed in my thesis. For a more in-depth understanding of these methods, I recommend referring to the following authoritative sources: [106–110].

1.2.1 Reaction Diffusion Equations

Reaction Diffusion Systems (RDS) refer to the class of partial differential equations where the right hand side of a time dependent equation can be split into a local (in

space) "reaction" component and a non-local transport due to "diffusion" component. The reaction diffusion equation is generally expressed in the following form:

$$\frac{\partial u}{\partial t} = D\nabla^2 u + f(u), \tag{1.1}$$

where u is the local population density, D is the diffusion coefficient, ∇ is the spatial gradient, and $f(u)$ describes the net population change from birth and death.

The application of reaction-diffusion models to tackle biological challenges has a rich historical foundation. In 1937, Fisher [111] pioneered the use of the 1-D reaction-diffusion equation in genetics problems, as documented in his influential paper titled *"The wave of advance of advantageous genes".* Fisher used the logistic growth of the form

$$f(u) = \mu u \left(1 - \frac{u}{K}\right), \quad K > 0, \tag{1.2}$$

where μ is the population growth rate and K is the carrying capacity to present the reaction kinetics. Simultaneously, Kolmogorov, Petrovsky, and Piskunov [112] explored the analysis of the reaction-diffusion equation in two dimensions during the same year, investigating a more generalized monostable reaction term. Skellam [113] employed reaction-diffusion equations in ecology to depict the spread of muskrats in central Europe, while Turing [114], Swindale [115], and Murray [116] focused on modeling pattern formation. Additionally, Kendall [117] applied these models in the context of epidemics. The issues addressed by reaction-diffusion models include critical patch size [118, 119], biological invasions [106, 107], predator-prey systems [120–123] and pattern formation [124].

As I mentioned above, reaction diffusion equations can not only describe the biological motion but also can produce a variety of patterns that are similar to those often seen in nature. Alan Turing was the first to develop reaction diffusion model

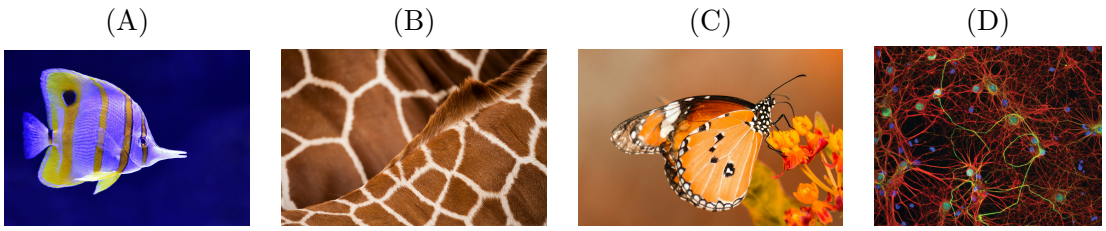

Figure 1.3: Examples of pattern formation and excitable system in biology. Source: (A)-(C): https://unsplash.com and (D): https://opentextbc.ca/introductiontopsychology/chapter/3-1-the-neuron-is-the-building-block-of-the-nervous-system

in his pioneer paper, *"The chemical basis of morphogenesis"* [114]. Turing suggested that, under certain conditions, adding the diffusion to the reaction kinetics can lead to spatial pattern formation as diffusion can drive instability to spatially homogeneous steady states, which is known as *Turing instability*. The interaction between short range activation and long range inhibition (i.e. $D_{inhibitor} >> D_{activator}$) can lead to pattern formation. Therefore, *bifurcation theory* must be applied to decide which parameters arise as a bifurcation parameter [110]. Reaction diffusion in *excitable* systems can lead to pattern formation as well. An excitable system is a system with two states: all or nothing response to stimulus; if the stimulus is superthreshold, the system exhibits large response (excursion) from rest while being quiescent under subthreshold stimulus. Following the response, there is a refractory period where the system doesn't response to any stimulus even a superthreshold one until the system recovers the excitability [125]. A famous example in biology of reaction diffusion in excitable systems is the FitzHugh–Nagumo model in electrophysiology, a simplified model for the propagation of electrical signals of the Hodgkin–Huxley model in nerve fibres [126, 127]. Figure 1.3 (A)-(C), are examples of pattern formation in nature, while Figure 1.3 (D) is a nerve system which is a famous example of excitable system in physiology.

It is notable to highlight that reaction-diffusion equations found important applications in the field of chemistry. Prominent instances include the Belousov-Zhabotinsky

reaction-diffusion model, which elucidates ion-catalyzed oxidation reactions, and the Gray-Scott reaction-diffusion model, which characterizes autocatalytic reactions [128, 129]. The Belousov-Zhabotinsky model specifically exemplifies the reaction-diffusion dynamics of a chemical oscillator within an excitable system [130].

1.2.2 Travelling Wave Analysis

Solutions of reaction diffusion equations can arise as travelling waves and as self-organized patterns. In this thesis, I use travelling wave analysis in Chapter 3, 4 and 5. A traveling wave solution refers to a wave that propagates through space over time while maintaining its overall shape with a constant velocity. The travelling wave solution is expressed as $U(z)$ with $z = x - ct$. Here $c > 0$ denotes the *wave speed*, the variable $z := x - ct$ is the *wave variable*, and the function $U(z)$ is the *wave profile* [108]. When $c = 0$, we have a *stationary wave* that does not propagate and is usually observed when inducing a fixed boundary conditions. Travelling waves have different forms. When $U(-\infty) \neq U(+\infty)$, we have the *wave front*, while when $U(-\infty) = U(+\infty)$, we have what is called *pulse wave* [131]. Another form of travelling wave is a *spatially periodic wave,* which is accrued when $U(z + p) = U(z)$ for some $p > 0$. A famous example of wave fronts are solutions of the Fisher-KPP equation [108], while FitzHugh–Nagumo model is an example for pulse waves in nerve systems [126, 127, 132].

The standard analysis approach to find a travelling wave solution is to find a non-negative orbit in the phase space connecting two steady states. If this path connects two different steady states it's called *heteroclinic orbit*, while it called *homoclinic orbit* if the start and the end of the orbit are the same [132]. We are interested in the case where the steady states are not equal i.e a heteroclinic orbit.

To find such heteroclinic orbit, the standard technique is to derive a system of ordinary differential equations (ODE), where

$$U' = \psi$$
$$\psi' = U'' = \frac{-c\,\psi - f(U)}{D}$$

with $U(-\infty) \neq U(\infty)$, and $\psi(-\infty) = \psi(\infty) = 0$.

Using the linearization around the two steady states and studying the local stability of them, we find the condition for c such that a non-negative orbit exists, and hence a travelling wave exists [108].

It is important to mention that the wave speed c is not necessary to be unique as in case of Fisher-KPP equation. Therefore, the wave speed is chosen to be the minimum i.e c^* for which the wave front solution exists. From a biological standpoint, our attention is directed towards identifying the wave speed value at which virus particles can effectively invade a cancerous tissue.

It is good to point out that there is a scenario in which a unique wave speed exists, as exemplified by the well-known case of the strong Allee effect equation [133], formulated as follows

$$\frac{\partial u}{\partial t} = D\frac{\partial^2 u}{\partial x^2} + \mu u\,(u-a)\,(1-u)\,, \tag{1.3}$$

where $0 < a < \frac{1}{2}$.

The Allee effect describes the situation where the populations long term survival depends on the initial population density. If the initial population is below the Allee threshold, the population will go to extinction, while the population will survive if the initial population is above this threshold. The unique wave speed of eqn (1.3) for $0 < a < \frac{1}{2}$ is

$$c = \left(\frac{1}{2} - a\right)\sqrt{2\mu D}.$$

Going back to the minimum wave speed, one of the pioneer results I would like to present here is the minimum wave speed c^* of the general Fisher equation which is called Fisher-KPP since it will be used in Chapter 2.

Lemma 1.2.1 *[108] For any 1-D equation of the form*

$$\frac{\partial u}{\partial t} = D\frac{\partial^2 u}{\partial x^2} + f(u), \tag{1.4}$$

for $K > 0$ and differentiable f. If $f(u)$ satisfies the following conditions:

$$\begin{aligned} &f(0) = 0, \quad f(K) = 0, \\ &f(u) > 0 \quad \text{for all} \quad 0 < u < K, \\ &f'(0) > 0, \quad f'(K) < 0, \\ &f'(0)u > f(u) \quad \text{for all} \quad 0 < u < \infty, \end{aligned}$$

then the minimal wave speed is

$$c^* = 2\sqrt{Df'(0)}. \tag{1.5}$$

Unfortunately, it is often difficult to find such a result if the system has more than one equations. Therefore, an easier technique can be used to determine the minimum wave speed of the wave front. This method is called the *leading edge method.* The leading edge method focuses on the behaviour of the front profile of the invasion near the extinction steady state, which shows exponential decay of the form $\varepsilon e^{-\lambda z}$, where $\lambda > 0$ is denoted as exponential decay rate and $\varepsilon \neq 0$ is a small constant. Thus, the solution of $u(x,t)$ can be in the form

$$u(z) = \varepsilon e^{-\lambda z}. \tag{1.6}$$

Substituting eqn (1.6) in eqn (1.1), we get

$$c\lambda\varepsilon e^{-\lambda z} = D\lambda^2\varepsilon e^{-\lambda z} + f(\varepsilon e^{-\lambda z}),$$

which can be written in the form

$$D\lambda^2\varepsilon e^{-\lambda z} - c\lambda\varepsilon e^{-\lambda z} + f(\varepsilon e^{-\lambda z}) = 0.$$

Applying Taylor expansion on f about $\varepsilon = 0$, and using $f(0) = 0$, we get

$$\begin{aligned} f(\varepsilon e^{-\lambda z}) &= f(0) + f'(0)\varepsilon e^{-\lambda z} + O(\varepsilon^2) \\ &= f'(0)\varepsilon e^{-\lambda z} + O(\varepsilon^2). \end{aligned}$$

Thus, we obtain

$$D\lambda^2\varepsilon e^{-\lambda z} - c\lambda\varepsilon e^{-\lambda z} + f'(0)\varepsilon e^{-\lambda z} = 0.$$

which is equivalent to

$$\varepsilon e^{-\lambda z}\left(D\lambda^2 - c\lambda + f'(0)\right) = 0.$$

Since $e^{-\lambda z} \neq 0$ and $\varepsilon \neq 0$, the leading order is

$$D\lambda^2 - c\lambda + f'(0) = 0, \tag{1.7}$$

which is called the *characteristic equation*. Solving (1.7) for λ, we get

$$\lambda_{1,2} = \frac{c \pm \sqrt{c^2 - 4Df'(0)}}{2D}. \tag{1.8}$$

Since $\lambda > 0$, we have $c^2 - 4Df'(0) \geq 0$, hence

$$c^* = 2\sqrt{Df'(0)} \quad \text{with corresponding decay rate } \lambda^* = \frac{c^*}{2D}. \tag{1.9}$$

To illustrate the idea of the leading edge method, let us consider the case when f is the logistic form in Fisher equation as in eqn (1.2). Thus, we have

$$
\begin{aligned}
&D\lambda^2\varepsilon e^{-\lambda z} - c\lambda\varepsilon e^{-\lambda z} + \mu\varepsilon e^{-\lambda z} - \frac{\mu}{K}\varepsilon e^{-2\lambda z} = 0 \\
&e^{-\lambda z}\left(D\lambda^2\varepsilon - c\lambda\varepsilon + \mu\varepsilon - \frac{\mu}{K}\varepsilon e^{-\lambda z}\right) = 0.
\end{aligned} \tag{1.10}
$$

At the leading edge $z \to \infty$, we have $\frac{\mu}{K}e^{-\lambda z} \approx 0$. Hence to leading order we obtain the characteristic equation

$$
D\lambda^2 - c\lambda + \mu = 0, \tag{1.11}
$$

and

$$
\lambda_{1,2} = \frac{c \pm \sqrt{c^2 - 4D\mu}}{2D}. \tag{1.12}
$$

Thus, we get

$$
c^* = 2\sqrt{D\mu} \quad \text{with corresponding decay rate } \lambda^* = \frac{c^*}{2D}. \tag{1.13}
$$

Therefore, the solution around the extinction steady state behaves like $e^{-\frac{c^*}{2D}z}$ for $z \to \infty$. To get a good estimation of the minimum wave speed, it is good enough to measure the decay rate λ of the wave profile for large x, a method called *linear conjuncture* [134].

1.2.3 Homogenization Method

I would like to introduce another valuable approach, known as the homogenization method, which I employ in Chapter 2. In numerous practical scenarios, spatial or temporal scales exhibit variations due to the inherent heterogeneity of the medium or the intricacies of a dynamical system. The homogenization method, a robust technique widely employed in physics and engineering, particularly in areas such as heat transfer in composite materials [135], proves instrumental in tackling problems involving multiple scales in partial differential equations. Its application extends to ecological contexts, addressing spatial heterogeneity issues like seed dispersal [136],

the spread of feline leukemia virus [137], dispersal in heterogeneous habitats [138], and the propagation of wildlife diseases across landscapes [139].

At the core of the homogenization method lies a fundamental strategy: the construction of micro-scale (local scale) models. These models serve as the foundation for deducing macro-scale (global scale) laws and constitutive relations through proper averaging over the micro-scale [140]. The analytical framework for this upscaling process is commonly referred to as homogenization, as illustrated in Figure 1.4. Notably, in Chapter 2, we use the homogenization theory in the field of microbiology, expanding the scope of this method beyond its conventional domains.

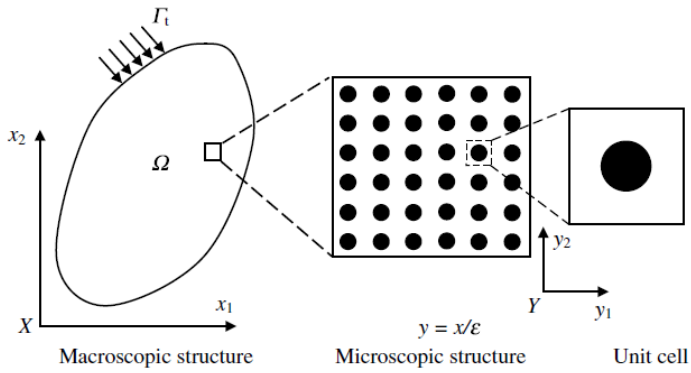

Figure 1.4: A scheme illustrating the homogenization technique in periodic 2-D. Here $X = (x_1, x_2)$ is the macroscopic scale, while $Y = (y_1, y_2)$ represents the microscale. The two scales are related by a small parameter $\varepsilon > 0$ such that $(y_1, y_2) = (\frac{x_1}{\varepsilon}, \frac{x_2}{\varepsilon})$ [141].

1.2.4 Stability and Hopf Bifurcation

In general, analyzing the dynamical system of a reaction-diffusion model involves an analysis of the kinetic dynamics using *dynamical system theory* [110]. This approach finds widespread application in mathematical biology, shedding light on the intricacies of the system through the lens of ordinary differential equations. Dynamical systems theory plays a crucial role in unraveling the qualitative changes in the behavior of such systems over time. Here are some of the key definitions that have been employed throughout the thesis.

Definition 1.2.2 *Consider a nonlinear autonomous ODE in* $\mathbb{R}^n$

$$x' = f(x), \tag{1.14}$$

where $f \in C(E) \to \mathbb{R}^n$ *and* E *is open subset of* $\mathbb{R}^n$. *A vector* $\overline{x} \in \mathbb{R}^n$ *is an equilibrium or steady state of (1.14) if* $f(\overline{x}) = 0$.

Under certain conditions, the solutions of (1.14) do not intersect which is when the function f is continuous and Lipschitz.

Definition 1.2.3 *A function* $f : E \to \mathbb{R}$ *and* E *is open subset of* $\mathbb{R}^n$ *is called Lipschitz continuous if there is a constant* $L > 0$ *such that* $\mid f(x) - f(y) \mid \leq L \mid x - y \mid$ *for all* $x, y \in E$.

Theorem 1.2.4 (Picard-Lindelöf.) *Assume the function* $f : E \to \mathbb{R}^n$ *is Lipschtiz continuous. Let the initial condition* $x(0) = x_0 \subset E$. *Then there exists an* $\varepsilon > 0$, *such that the initial value problem*

$$\frac{dx}{dt} = f(x), \quad x(0) = x_0 \tag{1.15}$$

has a unique solution $x(t)$ *for* $0 \leq t \leq \varepsilon$.

Now, after defining the steady states and the conditions for obtaining a unique solution, it is the time to define when these steady states are stable.

Definition 1.2.5 *Let* x *be the solution of (1.14) with initial condition* x_0. *Then*

1. *A steady state* $\overline{x}$ *is stable if for all* $\varepsilon > 0$, *there exists* $\delta > 0$ *such that solutions with* $\| x_0 - \overline{x} \| < \delta$ *satisfy* $\| x - \overline{x} \| < \varepsilon$ *for all time* $t > 0$. *This means the steady state* $\overline{x}$ *is stable if the solutions which starts nearby stays nearby.*

2. *A steady state $\overline{x}$ which is not stable is called unstable. This means there is at least one solution which diverges from $\overline{x}$.*

3. *$\overline{x}$ is asymptotically stable if $\overline{x}$ is stable and there exists a $\delta > 0$ such that all solutions with $\| x_0 - \overline{x} \| < \delta$, satisfy $\lim_{t\to\infty} \| x - \overline{x} \| = 0$. This means a steady state $\overline{x}$ is asymptotically stable if $\overline{x}$ is stable and all solutions near $\overline{x}$ converges to $\overline{x}$.*

Finding the explicit solution for nonlinear ODE system is almost impossible, instead, we can solve the linear system part, which can illustrate the qualitative behaviour of the nonlinear system around the steady states. To do so, we need first to linearize the system about these steady states with $f \in C^1$ to get

$$x' = J\,x,$$

where

$$J = \begin{bmatrix} \frac{\partial f_1}{\partial x_1} & \frac{\partial f_1}{\partial x_2} & \frac{\partial f_1}{\partial x_3} \cdots \frac{\partial f_1}{\partial x_n} \\ \frac{\partial f_2}{\partial x_1} & \frac{\partial f_2}{\partial x_2} & \frac{\partial f_2}{\partial x_3} \cdots \frac{\partial f_2}{\partial x_n} \\ \vdots & \vdots & \vdots \\ \frac{\partial f_n}{\partial x_1} & \frac{\partial f_n}{\partial x_2} & \frac{\partial f_n}{\partial x_3} \cdots \frac{\partial f_n}{\partial x_n} \end{bmatrix} \quad \text{and} \quad x = \begin{bmatrix} x_1 \\ x_2 \\ \vdots \\ x_n \end{bmatrix}.$$

The matrix J is called Jacobian matrix, substituting the steady state $\overline{x}$ values on the Jacobian matrix J, we get the linear system

$$x' = A\,x, \tag{1.16}$$

where $A = J(\overline{x})$ is a matrix with constant entries.

The nonlinear system (1.14) has similar behaviour to the linearized system (1.16) in a small neighborhood if the steady states are hyperbolic. Below is the definition of hyperbolic steady state and Hartman-Grobman theorem that utilizes this hypothesis.

Definition 1.2.6 *The steady state $\overline{x}$ is called hyperbolic if all eigenvalues of the A have nonzero real parts.*

Theorem 1.2.7 (Hartman-Grobman) *Assume that $\overline{x}$ is a hyperbolic steady state. Then, in a small neighborhood of $\overline{x}$, the phase portrait of the nonlinear system (1.14) is equivalent to that of the linearized system (1.16).*

The stability behavior of a steady state depends upon the existence of real and imaginary components of the eigenvalues, along with the signs of the real components and the distinctness of their values. The following is a summary of the relationship between the eigenvalues and the stability of a steady state.

1. If the eigenvalues are complex i.e $\lambda = a + bi$ with $b \neq 0$, we have three cases:

    - When the real part a is positive, the steady state of (1.14) is unstable and the system behaves as a spiral away from the steady state.
    - When the real part a is negative, the steady state of (1.14) is stable and the system behaves as a spiral toward the steady state.
    - When the real part is zero, then the linearized system (1.16) has a continuous family of concentric periodic orbits around zero. In this case, the steady state is non-hyperbolic and according to Hartman- Grobman theorem, we cannot make any statement about the qualitative behavior of the nonlinear system (1.14) near the steady state.

2. If the eigenvalues are real, we have three cases:

    - If all the eigenvalues are positive, the steady state of (1.14) is an unstable node.
    - If all the eigenvalues are negative, the steady state of (1.14) is a stable node.

- If some of the eigenvalues are positive and some of them are negative, the steady of (1.14) is called a saddle node.

At the same time, mathematical models have many parameters where the changes in their values can change the qualitative behaviour of the solution. If this is the case, we call it *bifurcation.*

Consider a scalar ODE depending on a scalar parameter μ of the form

$$x' = f(x, \mu), \quad x \in \mathbb{R}, \, \mu \in \mathbb{R},$$

where μ is the parameter, and $f : \mathbb{R}^2 \to \mathbb{R}$ is continuously differentiable. Then we say that $\overline{x}$ is a bifurcation point and $\overline{\mu}$ is a bifurcation value if

$$f(\overline{x}, \overline{\mu}) = 0 \quad \text{and} \quad \frac{\partial}{\partial x} f(\overline{x}, \overline{\mu}) = 0.$$

There are four common bifurcations which are saddle-node bifurcation, transcritical bifurcation, pitchfork bifurcation and Hopf bifurcation. To make it simple, a saddle-node bifurcation can be described as a single branch of steady states that undergoes a change in stability, from being stable to unstable or reversed. A transcritical bifurcation appears when there is an exchange of stabilities between two steady states. A Pitchfork bifurcation can be described as a branch of steady states which changes stability type at the bifurcation point and is intersected there by a stable (or unstable) branch. Finally, we get a Hopf bifurcation, when there is a local birth or death of a periodic solution from a steady state as the parameter crosses a critical value. This happens when a complex conjugate pair of eigenvalues of the linearized system at a steady state becomes purely imaginary which implies that a Hopf bifurcation can only occur in systems of dimension two or higher.

We are interested in Hopf bifurcation as it is related to the prey-predator oscillation in cancer-virus dynamics. Liu [142] found a criterion of Hopf bifurcations without using eigenvalues. His theorem is presented below:

Definition 1.2.8 (Hopf Bifurcation) *Consider a system*

$$x' = f_\mu(x), \quad x \in \mathbb{R}^n,\ \mu \in \mathbb{R}^1,\ n \geq 2, \tag{1.17}$$

with a equilibrium (x_0, μ_0)*, and* $f \in C^\infty$*. Assume that*

1. *The Jacobian matrix* $D_x f_{\mu_0}(x_0)$ *has a simple pair of purely imaginary eigenvalues and other eigenvalues have negative real parts. Then there is a smooth curve of equilibria* $(x(\mu), \mu)$ *with* $x(\mu_0) = x_0$*. The eigenvalues* $\lambda(\mu), \overline{\lambda}(\mu)$ *of* $J(\mu) = D_x f_\mu(x(\mu))$ *which are purely imaginary at* $\mu = \mu_0$ *vary smoothly with* μ*. Moreover, if*

2. $\frac{d(Re(\lambda(\mu_0)))}{d\mu} \neq 0,$

then there is a simple Hopf bifurcation. By simple Hopf bifurcation we mean that there exists a small neighborhood of the bifurcation value such that no further Hopf bifurcation arises in this neighborhood.

Later in the thesis I will use a characterisation of a Hopf bifurcation by Liu [142]. Following Liu [142], the characteristic polynomial of the Jacobian matrix $J(\mu)$ denoted by

$$p(\lambda; \mu) = p_0(\mu) + p_1(\mu)\lambda + p_2(\mu)\lambda^2 + \cdots + p_n(\mu)\lambda^n, \tag{1.18}$$

where every $p_i(\mu)$ is a smooth function of μ, $p_n(\mu) = 1$ and $p_0(\mu) > 0$. Let

$$L_n(\mu) = \begin{pmatrix} p_1(\mu) & p_0(\mu) & 0 & 0 & \cdots & 0 \\ p_3(\mu) & p_2(\mu) & p_1(\mu) & p_0(\mu) & \cdots & 0 \\ \vdots & \vdots & \vdots & \vdots & \cdots & \vdots \\ p_{2n-1}(\mu) & p_{2n-2}(\mu) & p_{2n-3} & p_{2n-4} & \cdots & p_n(\mu) \end{pmatrix},$$

where $p_i(\mu) = 0$ if $i < 0$ or $i > n$. Consider

$$
\begin{aligned}
D_1(\mu) &= det(L_1(\mu)) = p_1(\mu) > 0, \\
D_2(\mu) &= det(L_2(\mu)) = det \begin{pmatrix} p_1(\mu) & p_0(\mu) \\ p_3(\mu) & p_2(\mu) \end{pmatrix} > 0, \\
&\vdots \\
D_n(\mu) &= det(L_n(\mu)) > 0.
\end{aligned}
$$

Theorem 1.2.9 *Assume there is a smooth curve of equilibria $(x(\mu), \mu)$, with $(x(\mu_0), x_0)$ for system (1.17). Conditions (1) and (2) for a simple Hopf bifurcation are equivalent to the following conditions on the coefficients of the characteristic polynomial $p(\lambda; \mu)$:*

1. $p_0(\mu_0) > 0$, $D_1(\mu_0) > 0, \cdots, D_{n-2}(\mu_0) > 0$, $D_{n-1}(\mu_0) = 0$,
2. $\frac{d\, D_{n-1}(\mu_0)}{d\mu} \neq 0$.

A simplified version of Liu [142] for characteristic polynomial of order 3 is introduced by Jehadi et al. [143].

1.2.5 Tumor Control Probability

In cancer treatment, the effectiveness of any therapeutic approach relies on either eradicating the cancer or, at the very least, bringing the tumor under control. This involves addressing situations where the density of tumor cells approaches zero. In such instances, we enter a domain where stochastic events become prominent, and a deterministic description may fall short. The exploration of stochastic models for cancer eradication initiated with the inception of cancer radiation therapy [144]. Consequently, a novel method has been introduced based on stochastic processes to quantify the anticipated success of a given treatment, known as tumor control probability (TCP). These TCP models are grounded in various stochastic approaches, including the Poisson process, general birth–death process, branching process, and others. In this section, I will provide only the TCP based on a *Poisson process*, as it is the

one that is specifically utilized in my work, particularly in Chapter 3 and 4. Poisson process is a stochastic process which is continuous in time and with a discrete state space.

Consider $N(t)$ to be a random variable that represents the number of cells at time t. Let $p_k(t)$ be the probability that the random variable $N(t) = k$, i.e

$$p_k(t) = Pr\{N(t) = k\} \quad \text{with} \quad \sum_{k=0}^{\infty} p_k(t) = 1.$$

Thus the family $\{p_k(t)\}$ represents the probability distribution of the cell number $N(t)$ for every value of t and the family of random variables $\{N(t),\, t \geq 0\}$ is stochastic process [145]. Furthermore, $N(t)$ follows Poisson distribution with mean λ, where λ is constant if the following conditions are satisfied:

1. The events are independent of each other.
2. The average rate of occurrence through time is constant.
3. Two events cannot occur at the same time.

Thus, we have the probability of $N(t) = k$ to be

$$p_k(t) = \frac{\lambda^k e^{-\lambda}}{k!},$$

where $\lambda > 0$ is a parameter.

Now, assume that the initial number of tumor cells N_0 is large, that the cell survival is a rare event, and that the event of tumor cell death is stochastically independent. Then, the survival fraction is $S(t) = \frac{N(t)}{N_0}$ and hence the tumor control probability can be evaluated as the following

$$TCP(t) = p_0(t) = e^{-\lambda}, \tag{1.19}$$

where $\lambda = N_0\, S(t)$ is the expected number of surviving tumour cells.

1.2.6 Parameter Estimation Methods

Determining model parameters is a crucial stage in optimizing the model to closely align with the observed data. There are several prevalent methods for parameter estimation include maximum likelihood, least squares estimation, and Bayesian estimation. In this discussion, emphasis will be placed on maximum likelihood and least squares estimation, both of which were employed in Chapter 2 and Chapter 5.

Assume the parameter of the model to be estimated is $\hat{p}$ with a quality measure $q(\hat{p}|\, data)$ that is the measure of how well the model with parameter $\hat{p}$ fits the observed data. Furthermore, assume the data are typical in the sense that these data represents a common or normal set of observations. Then, we move from the quality of the parameter value under given data to the probability of the data under given parameter, which is called the likelihood of the parameter. Thus, we define

$$q(\hat{p}|\, data) = p(data|\, \hat{p}),$$

and our task is to find the maximum likelihood estimator.

Definition 1.2.10 *Let $\hat{p} \in \mathbb{R}^n$ be the parameter vector of a given model. The function*

$$\mathcal{L} : \mathbb{R}^n \to \mathbb{R}_+,$$

that maps a parameter set $\hat{\pi} \in \mathbb{R}^n$ to the probability to find given data is called the likelihood. The log-likelihood is the logarithm of the function,

$$\mathcal{LL} : \mathbb{R}^n \to \mathbb{R}, \quad \mathcal{LL}(\hat{\pi}) = ln(\mathcal{L}(\hat{\pi})).$$

Definition 1.2.11 *A parameter vector $\overline{\pi}$ that maximizes $\mathcal{L}$ is called a maximum likelihood estimation of $\hat{p}$.*

After defining the likelihood function, log-likelihood and the maximum likelihood estimator, we derive the least square method. Considering our data a time series

measurement with time points $t_1, ..., t_k$ and corresponding data points $x_1, ..., x_k$, we assume our model predicts these data via a function $q(t_i; \hat{p})$ such that $x_i \approx q(t_i; \hat{p})$, where $\hat{p}$ denotes a set of parameters. As we are working with deterministic models, we are expecting to have a measurement error. In addition, due to the universality of the normal distribution, we assume that the data is normally distributed with expectation (mean) $\lambda = q(t_i; \hat{p})$ and unknown variance σ^2. In this case, the data x_i considered as a random variables X_i that are independent and distributed according to

$$X_i \sim N(q(t_i; \hat{p}), \sigma^2). \tag{1.20}$$

Then we derive the maximum likelihood of normally distributed data as the following

$$\mathcal{L}(\hat{p}) = p(x_i = X_i, i = 1, ..., k|\hat{p} = (\lambda, \sigma)) = \prod_{i=1}^{k} \frac{1}{\sqrt{2\pi}\sigma} e^{-} \frac{(x_i - q(t_i; \hat{p}))^2}{2\sigma^2}.$$

Thus, the log-likelihood becomes

$$\mathcal{LL}(\hat{p}) = -\sum_{i=1}^{k} \ln(\sqrt{2\pi}\sigma) - \frac{1}{2\sigma^2} \sum_{i=1}^{k} (x_i - q(t_i; \hat{p}))^2.$$

For any given σ, maximizing $\mathcal{LL}$ is equivalent to minimizing

$$\text{least square error}(\hat{p}) := \sum_{i=1}^{k} (x_i - q(t_i; \hat{p}))^2.$$

The least square error has been used in Chapter 2 and Chapter 5.

1.3 Thesis Outline

This thesis is structured around three distinct projects. In Chapter 2, we employ the Fisher-KPP reaction-diffusion model and the homogenization method to explore the spatial dependencies within virus load data from a checkerboard experiment. Our investigation into the impact of spatial complexity among heterogeneous populations

on viral load involves the application of an innovative cell-printing method introduced by Hesung Now, Ju An Park, Woo-Jong Kim, Sungjune Jung, and Joo-Yeon Yoo. Contrary to a simplistic arithmetic summation of individual cellular activities, as confirmed by our model analysis, the experimental results reveal that the total virus load exhibits a more intricate relationship. Remarkably, our model not only elucidates the observed virus load data but also predicts values not captured in the experiments. Furthermore, we employ numerical techniques to ascertain the spatial distribution of viral load across the periodic domain using our mathematical model. Our analysis serves as a notable illustration of how spatial heterogeneity influences cell responses to virus infection, underscoring the importance of considering spatial arrangement rather than extrapolating measurements solely from isolated cell populations to heterogeneous mixtures of cells.

In Chapter 3 and Chapter 4, we extend our systematic examination of spatial oscillation patterns resulting from Hopf bifurcation, exploring their clinical relevance and intricate characteristics. Our analysis involves a bifurcation study of a spatially explicit reaction-diffusion model aimed at uncovering spatio-temporal patterns in virus infection. We consider two types of virus-tumor interactions: mass-action and Michaelis–Menten kinetics. The targeted pattern for tumor eradication is the hollow ring pattern, and we identify precise conditions for its occurrence. Furthermore, we determine the minimum speed of traveling invasion waves for both cancer and oncolytic viruses. Our 2-D numerical simulations unveil complex spatial interactions in virus infection, revealing a novel phenomenon characterized by periodic peak splitting in mass action case.

In Chapter 5, we probe into the oncolytic potential of the reovirus, specifically examining both the wild type T3wt and its mutated variant, SV5. Through in vitro experiments, SV5 demonstrates superior capabilities in spreading within cancer cells, resulting in larger plaque size in cell monolayer experiments as compared to T3wt. A significant contributing factor to this enhanced performance lies in the reduced

binding affinity of SV5 to cells when compared to T3wt. To comprehend the interplay between the binding process and virus spread for both variants, we employ a reaction-diffusion model. Our computational results reveal the presence of an optimal binding rate that corresponds to an optimal viral invasion wave speed, influencing the overall spread of the virus. This identification provides a rationale for the observed larger plaque size in SV5. Moreover, we explore the influence of burst size and binding rate on plaque size. Our investigation reveals the existence of an optimal binding rate corresponding to each burst size. This underscores the significance of burst size alongside binding rate, emphasizing that the role of burst size is crucial and cannot be overlooked as mentioned in section 1.1.2.

In Chapter 6, we consolidate the research projects and highlight their key findings. Additionally, we engage in a discussion about potential directions for future work.

Chapter 2

Homogenization in Microbiology

The material of this Chapter has been published as

- A.A. Baabdulla, J.A. Park, W.J. Kim, S. Jung, Yoo, J.Y. Yoo and T. Hillen. Homogenization of a reaction diffusion equation can explain influenza A virus load data. *Journal of Theoretical Biology*, 527:110816, 2021.

2.1 Introduction

Viruses are responsible for a diverse range of human illnesses, encompassing the common cold, influenza, HIV/AIDS, COVID-19, and various others. Consequently, the prevention of viral infections is a critical aspect of virology. Ongoing research in virology aims to deepen our understanding of viral biology and develop more effective strategies for prevention and treatment. Consequently, numerous experiments, conducted in vitro or in vivo, focus on evaluating viral load, a crucial parameter for understanding the progression and severity of viral infections, as well as for monitoring treatment efficacy.

Simultaneously, the field continues to explore mathematical modeling of viral load, an area of active investigation [146–149]. While many models rely on ordinary differential equations, some methodologies incorporate spatial modeling techniques [70, 81, 148].

In the realm of cellular populations, there exists inherent heterogeneity. However,

conventional experimental approaches often overlook this diversity by treating populations as homogeneous mixtures of cells. Snijder et al. [150] were among the first to delve into the significance of this heterogeneity and its correlation with virus infection patterns. Yet, despite these advancements, the impact of spatial complexity within such populations remains largely unexplored. Consequently, there is a burgeoning interest in investigating whether viral susceptibility varies with the spatial distributions of heterogeneous sub-populations.

To tackle this inquiry, we developed a new mathematical model rooted in the Fisher-KPP equation, employing homogenization methods for the first time in microbiology. Our model was informed by viral load data obtained from a checkerboard experiment, where an innovative cell-printing technique introduced by Hesung Now, Ju An Park, Woo-Jong Kim, Sungjune Jung, and Joo-Yeon Yoo was used [151]. This technique enabled them to precisely manipulate cell arrangements and observe resulting viral dynamics.

In Park et al.'s study [151], the experimental setup comprised equal proportions of A549 human alveolar lung epithelial cells and HeLa cervical cancer cells. Notably, these cell lines exhibit varying levels of infectivity towards influenza A, with A549 cells demonstrating "strong" infectivity and HeLa cells displaying "weak" infectivity [152, 153]. Surprisingly, the total viral load did not simply correspond to an arithmetic summation of individual cellular activities.

A similar experiment was conducted on mouse embryonic fibroblasts (MEF) exposed to influenza A [154]. Here, we investigate how spatial heterogeneity influences the response of MEF to influenza A [154]. MEF of the $Ube1L^{-/-}$ type encompass two distinct sub-populations: one robustly supports significant viral infection (i.e., "strong" infectivity), while the other sustains a lesser viral load (i.e., "weak" infectivity). We offer novel insights into the dynamics of viral load infection in $Ube1L^{-/-}$ MEF, organized in a checkerboard pattern with varying inner square sizes (see Figure 2.1 (A)). Similar to Park et al.'s findings [151], the total viral load one day post-

inoculation demonstrates significant dependence on the sizes of these inner squares (see Figure 2.1 (B)). Employing a reaction-diffusion model, we elucidate this observation, demonstrating how mathematical homogenization can explain spatial disparities.

Our analysis reveals that, as individual patches increase in size, both the growth rate and carrying capacity represent arithmetic means across patches. However, as patches become finer, the average growth rate remains an arithmetic mean, while the carrying capacity transitions to a harmonic mean. Through fitting our model to experimental data, we anticipate that deviations in viral load would become imperceptible within half a day. Furthermore, we predict viral load variations across unmeasured inner squares in our experiment and estimate the distance virions can traverse within a day.

We outline Chapter 2 as the following: In the next section (Section 2.2) we explain the experimental set up and the data collection. In Section 2.3 we introduce the mathematical model. We chose a very classical Fisher-KPP reaction-diffusion equation [106], which is quite sufficient for our purpose. We then perform the spatial homogenization as it is relevant for our problem. From this analysis the dichotomy between arithmetic and harmonic means arises. In Section 2.4 we fit our model to our virus-load data using a log-likelihood method, thereby explaining the observed virus load dependence on the spatial arrangement. In Section 2.5 we present numerical solutions of the corresponding model, which show the spatial distribution of the viral infection across the checkerboard pattern. We close with a discussion in Section 2.6.

2.2 Influenza A Infection Experiments

We investigate mouse embryonic fibroblast (MEF) cells lacking Ube1L ($Ube1L^{-/-}$), a ubiquitin-like modifier activating enzyme crucial for ISGylation protein function, which conjugates Interferon (IFN) stimulated gene 15 (ISG15) to target proteins. The $Ube1L^{-/-}$ genotype represents null mutations of Ueb1L, resulting in the deactivation of Ueb1L production. Our examination revealed that $Ube1L^{-/-}$ populations

exhibit bimodal characteristics, displaying two sub-populations with varying degrees of antiviral activity [154]. We denote these subpopulations as $Ube1L^{-/-}(S)$ and $Ube1L^{-/-}(W)$, representing those with "strong" and "weak" infectivity, respectively. Details of viral infection data for each population in isolation are provided in the supplementary material (Appendix A Tables A.1 and A.2).

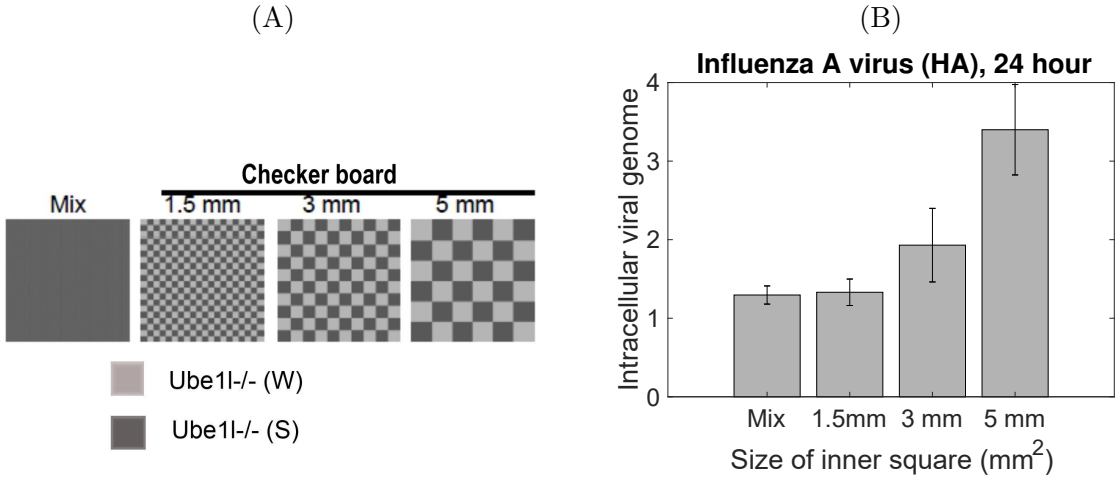

Figure 2.1: **(A):** Design of cell-printing pattern, **(B):** Viral load measurement after 24h.

To explore the impact of spatial distribution patterns on the overall virus load of the population, the Korean group employed inkjet bioprinting to arrange $Ube1L^{-/-}(S)$ and $Ube1L^{-/-}(W)$ cells in a regular checkerboard pattern [151]. The size of the checkerboard squares was kept constant at 30×30 mm^2, while the size of inner squares was varied, with side lengths of 1.5 mm, 3 mm, 5 mm, and fully mixed (Figure 2.1 (A)). In Figure 2.1 (A), the cells printed alternatively in the checkerboard with light gray represent the $Ube1L^{-/-}(W)$ cells, while those in dark gray represent the $Ube1L^{-/-}(S)$ cells. Consequently, the geometric separation between $Ube1L^{-/-}(S)$ and $Ube1L^{-/-}(W)$ cells increased as the size of the inner squares enlarged. A mixed scenario with a 50/50 ratio of $Ube1L^{-/-}(S)$ and $Ube1L^{-/-}(W)$ cells served as the control group. In each experiment, both checkerboard-patterned and mixed plates were infected with Influenza A virus and subsequently incubated for 24 hours. To

ensure uniformity, the inoculation was evenly distributed across the entire domain to mitigate spatial heterogeneities during the process. Infected cells were harvested, and the total intracellular viral genome was quantified using real-time quantitative PCR (Figure 2.1 (B)). The results from Figure 2.1 (B) suggest that the maximum viral load is achieved with the inner square of 5 mm, followed by the 3 mm square. Conversely, the lowest viral load is observed on the mixed plate. Additionally, the inner square of 1.5 mm demonstrates a viral load similar to that of the mixed plate.

All experiments utilized the inkjet printing method as described by [151]. For the cell cultures in isolation, experiments were repeated twice for each cell type, with each case involving inoculation of three plates at a density of approximately 6×10^6 cells/mL. Homogeneous cell populations were printed using the same setup as the 1.5 mm checkerboard printing, with each square containing cells of the same type (all black or all white, respectively). Results for homogeneous populations are presented in Tables A.1 and A.2, while checkerboard measurements were replicated three times, with results detailed in Appendix A Table A.3.

The Livak method (Delta Delta CT) was employed to determine the relative quantification (gene expression), calculated as:

$$RQ = 2^{-(\Delta\Delta CT)}, \tag{2.1}$$

where CT represents the cycle number at which the fluorescence generated by the PCR of the influenza A gene becomes discernible from the background noise cycle threshold (CT) of the sample. ΔCT is measured using the formula:

$$\Delta CT = CT(\text{target gene}) - CT(\text{reference gene}). \tag{2.2}$$

In this study, the target gene is the influenza A hemagglutinin (HA) gene, and the reference gene is the mouse glyceraldehyde 3-phosphate dehydrogenase (mGAPDH) gene. Thus, $\Delta\Delta CT$ can be computed as:

$$\Delta\Delta CT = \Delta CT(\text{experimental sample}) - \Delta CT(\text{control sample}). \tag{2.3}$$

The full data set is shown in A.1 and A.2 for the homogeneous populations and in A.3 for the checkerboard data. The data from A.3 are shown in Figure 2.1 (B).

Examining the virus load data in Figure 2.1 (B), it's evident that there's a significant discrepancy in viral load depending on the inner square size, progressing from mixed, to 1.5 mm, to 3 mm, and to 5 mm. Interestingly, each experiment maintains the same ratio and mass of $Ube1L^{-/-}$ (W) and (S) cells. This observation suggests that the antiviral activity of the cell population as a whole does not merely sum up the individual cellular activities.

2.3 A Mathematical Model

Reaction-diffusion equations (RDEs) serve as a potent tool whenever the spatial spread of a population becomes significant. Among these equations, one of the simplest examples is the Fisher-KPP equation

$$\frac{\partial}{\partial t}v(x,t) = D\frac{\partial^2}{\partial x^2}v(x,t) + \mu(x)v(x,t)\left(1 - \frac{v(x,t)}{K(x)}\right), \tag{2.4}$$

where $v(x,t)$ is the viral density at time t and location x, D is the diffusion coefficient, describing the spatial spread of the virions, μ is the population growth rate of the virus, and K is the population carrying capacity.

The process of viral infection and replication within cells involves multiple layers [31–33]. Initially, virions enter the cell via endocytosis. Following virion uncoating, the virus RNA undergoes replication and is subsequently reassembled into new virions. These virions are then released through various mechanisms, including exocytosis and cell lysis. In the case of lysis, the breakdown of the cell membrane releases virions into the extracellular fluid. Biologically, the virion growth rate parameter μ in our model

integrates an effective growth rate, encompassing the complexities of viral replication within cells. Meanwhile, the diffusion coefficient describes the spread of free virions. Given that the model aims to describe spatially varying checkerboard patterns, we propose that the growth rate $\mu(x)$ and the virus carrying capacity $K(x)$ are spatially dependent.

We assume that the transport of virus from cell to cell remains consistent across all cell types, thereby assuming that D is not spatially dependent and remains constant. Although the model could accommodate spatially varying $D(x)$ as well (see [155–157]), for our purposes, a model with constant D suffices to explain our data. Additionally, we lack biological evidence to justify differential diffusivities, hence we presume their equality.

We opted for the Fisher-KPP equation for our modeling problem for several reasons. Firstly, the available data on virus load on checkerboard patterns are limited to total virus load at a few time points (0, 6h, 12h, 24h). No microscopic measurements are conducted, hence details on virus replication inside cells, cell bursting, the number of released virions, virion transport within the cell tissue, and cell death are unavailable. While incorporating these details into a more sophisticated modeling framework would be ideal, it is currently neither feasible nor necessary. We find that the simple Fisher-KPP approach adequately accounts for the phenomenon at a macroscopic level.

A second reason for employing Fisher-KPP is its proven utility in numerous applications, its simplicity, and the well-understood behavior of this model [106]. Certain characteristics of the model can be immediately useful. For example, the invasion speed of the Fisher-KPP model (2.4) is

$$c = 2\sqrt{D\mu}. \tag{2.5}$$

The parameters of the Fisher-KPP equation (2.4) D, μ, K will be estimated based on the data from the experiments which we presented in the previous Section 2.2.

The experimental arrangement outlined above is a paradigm for a homogenization problem. It involves varying the microscopic scale (represented by inner squares) successively finer until, ultimately, a homogeneous mixture is achieved. What sets this experiment apart is our ability to not only measure the distinct separated and fully mixed states but also several intermediate values representing different mixture types. While homogenization is a widely recognized scaling technique in physical applications [109, 140], its application to ecological issues has only recently emerged [139, 158–160]. To our knowledge, this method has not previously been employed in the microbiological context under consideration here.

Given the problem's symmetry, we choose to present the argument in a one-dimensional context. Although the scaling method extends to higher dimensions, focusing on one dimension serves our purpose adequately. To replicate the checkerboard pattern, we partition the real line into uniform intervals, effectively distinguishing between populations with weak and strong infectivity (refer to Figure 2.2). Within this periodic domain, we examine the spatially dependent Fisher-KPP equation (2.4), wherein the virus's growth rate $\mu(x)$ and the carrying capacity of the virus load $K(x)$ vary across cell types, i.e.

$$
\begin{aligned}
K(x) &= \begin{cases} K_W, & x \in \text{ patch of type weak} \\ K_S, & x \in \text{ patch of type strong} \end{cases} \\
\mu(x) &= \begin{cases} \mu_W, & x \in \text{ patch of type weak} \\ \mu_S, & x \in \text{ patch of type strong.} \end{cases}
\end{aligned}
\tag{2.6}
$$

We use W to indicate the $Ube1L$ sub-population of weak infectivity and S for strong infectivity. For the general analysis we simply consider periodic functions $K(x)$, $\mu(x)$.

We differentiate between two pertinent spatial scales: the scale of individual patches, denoted by y and represented by the inner squares, and the global scale of the entire experiment, denoted by x and represented by the checkerboard printing. Additionally,

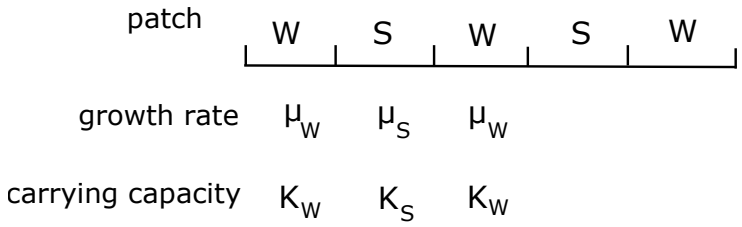

Figure 2.2: Sketch of a periodic patchy environment of two cell types.

we introduce a small parameter $\varepsilon > 0$

$$y = \frac{x}{\varepsilon},$$

where ε represents the ratio between the local and global scales. In the experiment,

$$\varepsilon = \frac{\text{the size of inner square}}{\text{the size of the checker board}}.$$

Thus, we can compute the ε for the 5 mm, 3 mm, and 1.5 mm inner squares as $\varepsilon = 1/6, 0.1, 0.05$, respectively.

We use standard assumptions in homogenization (see e.g. [109]) and assume that the growth rate $\mu(y)$ and the carrying capacity $K(y)$ change only on the small scale y and they do not vary on the large scale x. The virus load depends on both scales, $v(x, y, t)$ and the partial derivatives change as

$$\frac{d}{dx}v(x, y(x), t) = \frac{\partial}{\partial x}v(x, y, t) + \frac{1}{\varepsilon}\frac{\partial}{\partial y}v(x, y, t)$$

If we introduce this assumption into (2.4) we get the multiscale reaction-diffusion equation

$$\begin{aligned}\frac{\partial}{\partial t}v(x, y, t) = &\frac{D}{\varepsilon^2}\frac{\partial^2}{\partial y^2}v(x, y, t) + \frac{2D}{\varepsilon}\frac{\partial^2}{\partial x \partial y}v(x, y, t) + D\frac{\partial^2}{\partial x^2}v(x, y, t) \\ &+ \mu(y)v(x, y, t)\left(1 - \frac{v(x, y, t)}{K(y)}\right). \end{aligned} \tag{2.7}$$

We are seeking here a leading order approximation (v_0) to compute the viral load which is valid for small ε. To analyze this equation we use a perturbation expansion

in the small parameter $\varepsilon \ll 1$:

$$v(x,y,t) = v_0(x,y,t) + \varepsilon v_1(x,y,t) + \varepsilon^2 v_2(x,y,t) + \cdots , \tag{2.8}$$

where all functions $v_j(x,y,t), j = 0,1,2,\ldots$ are assumed to be periodic in y of period 1.

We substitute this expansion (2.8) into (2.7) and collect terms of equal order in ε. The leading order term is of order ε^{-2}:

- ε^{-2} : We obtain $0 = D\frac{\partial^2}{\partial y^2} v_0(x,y,t)$, which leads to a general form

  $$v_0(x,y,t) = c_1(x,t)y + c_2(x,t)$$

  Since $v_0(x,y,t)$ is periodic in y, the first term $c_1 = 0$ and we find that v_0 does not depend on y. We write $v_0(x,t)$ instead of using $c_2(x,t)$.

- ε^{-1} : In this case we find

  $$0 = D\frac{\partial^2}{\partial y^2} v_1(x,y,t) + 2D\frac{\partial^2}{\partial x \partial y} v_0(x,t).$$

  Since v_0 does not depend on y, the second term is zero. Hence the first term is zero as well. Again arguing with periodicity, we find that also v_1 is independent of y and we write $v_1(x,t)$.

- ε^0 : Here we find

  $$\begin{aligned}\frac{\partial}{\partial t} v_0(x,t) = & D\frac{\partial^2}{\partial y^2} v_2(x,y,t) + 2D\frac{\partial^2}{\partial x \partial y} v_1(x,t) + D\frac{\partial^2}{\partial x^2} v_0(x,t) \\ & + \mu(y) v_0(x,t)\left(1 - \frac{v_0(x,t)}{K(y)}\right).\end{aligned} \tag{2.9}$$

  Instead of solving this equation for v_2 we simply integrate over one period $y \in [0,1]$: Since v_0 and v_1 do not depend on y, and since v_2 is periodic, several terms simplify. We find the homogenized equation:

  $$\frac{\partial}{\partial t} v_0(x,t) = D\frac{\partial^2}{\partial x^2} v_0(x,t) + \int_0^1 \mu(y)dy \; v_0(x,t) - \int_0^1 \frac{\mu(y)}{K(y)} dy \; v_0^2(x,t). \tag{2.10}$$

To understand (2.10) we introduce the *arithmetic mean* and the *harmonic mean* as

$$\langle \mu \rangle_a = \int_0^1 \mu(y)dy, \qquad \langle K \rangle_h = \left(\int_0^1 \frac{1}{K(y)} dy \right)^{-1}$$

and we consider three cases:

Case 1: Consider $K(y) = K$ constant. Then (2.10) becomes a standard Fisher-KPP equation

$$\frac{\partial}{\partial t} v_0 = D \frac{\partial^2}{\partial x^2} v_0 + \langle \mu \rangle_a v_0 \left(1 - \frac{v_0}{K} \right), \tag{2.11}$$

where the homogenized growth rate $\langle \mu \rangle_a = \frac{1}{2}(\mu_S + \mu_W)$ is the arithmetic mean of $\mu(y)$.

Case 2: Consider $\mu(y) = \mu$ constant. In this case (2.10) becomes

$$\frac{\partial}{\partial t} v_0 = D \frac{\partial^2}{\partial x^2} v_0 + \mu v_0 \left(1 - \frac{v_0}{\langle K \rangle_h} \right), \tag{2.12}$$

where the carrying capacity arises as harmonic mean of $K(y)$:

$$\langle K \rangle_h = \frac{1}{\frac{1}{2}\left(\frac{1}{K_S} + \frac{1}{K_W} \right)}.$$

Case 3: We can also write the general homogenized equation (2.10) as a Fisher-KPP equation, however, with less intuitive average terms as

$$\frac{\partial}{\partial t} v_0 = D \frac{\partial^2}{\partial x^2} v_0 + \langle \mu \rangle_a v_0 \left(1 - \frac{v_0}{\langle \mu \rangle_a \left(\langle \frac{\mu}{K} \rangle_a \right)^{-1}} \right). \tag{2.13}$$

Here the effective growth rate and effective carrying capacity are

$$\tilde{\mu} = \langle \mu \rangle_a, \qquad \tilde{K} = \frac{\langle \mu \rangle_a}{\langle \frac{\mu}{K} \rangle_a}. \tag{2.14}$$

As illustrated in Figure 2.3, the fine printing of the virus hosts in patches of different sizes leads to different averaging. If the individual patches are large, then they can be considered as almost independent, and the growth rate and the carrying capacity will be the arithmetic means $\langle \mu \rangle_a, \langle K \rangle_a$ of the patches. On the other hand, for finer

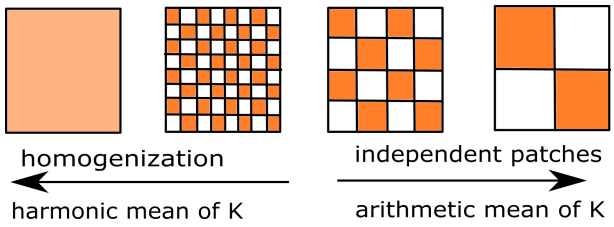

Figure 2.3: Sketch of a period patchy environment and the homogenization limit.

and finer patches we have shown that the average growth rate is still the arithmetic mean $\langle \mu \rangle_a$, however, the carrying capacity uses the harmonic mean. For example in Case 2 above it is $\langle K \rangle_h$ and it is known that

$$\frac{1}{\frac{1}{2}\left(\frac{1}{K_S}+\frac{1}{K_W}\right)} = \langle K \rangle_h \leq \langle K \rangle_a = \frac{1}{2}(K_S + K_W), \tag{2.15}$$

where equality is satisfied when $K_S = K_W$. Hence a reduction of the overall carrying capacity for finer patches is a direct consequence of the averaging procedure.

2.4 Application to the Fibroblast Experiments

Employing the homogenization method on the Fisher-KPP equation (2.4) yields three distinct cases. It is imperative to select the case that accurately represents the experimental data concerning the mouse embryonic fibroblasts.

In Case 1, $K(y)$ remains constant, rendering it inadequate for describing the observed data. This is because the averaging of the growth rate remains unchanged from coarse to fine experiments. However, Cases 2 and 3 can account for the observed phenomenon. Given that Case 2 is encompassed within Case 3 and is adequate for explaining the observed data, our analysis centers on Case 2. Here, the virus growth rate μ remains (almost) constant between the two cell types, while the carrying capacities exhibit significant differences:

$$\mu = \mu_S = \mu_W, \qquad \text{and} \qquad \langle K \rangle_h = \frac{1}{\frac{1}{2}\left(\frac{1}{K_S}+\frac{1}{K_W}\right)}.$$

As we determine which case to apply, it's essential to calibrate our model to the data. However, the formulas (2.15) only provide information about the mixed case and the

most separated case. They do not offer insights into intermediate scales, such as the 1.5 mm and 3 mm experiments. To incorporate these data points, we utilize the Fisher-KPP model (2.4). For a detailed numerical solution, please refer to Section 2.5.

We employ a least-squares approach to estimate the error:

$$E = \sum_{i=1}^{4} (M_i \text{ value} - PDE_i \text{ value})^2, \tag{2.16}$$

where i = 1,2,3,4 represent the inner square sizes: mix, 1.5 mm, 3 mm, and 5 mm, respectively. Here, M_i denotes the measurement value and PDE_i represents the integral of the solution curve of the partial differential equation (PDE).

Based on the above calculations it is straight forward to simply compare the arithmetic means and harmonic means with the available data. In Table 2.1 we show the virus load data at $t = 24\,\text{h}$ that correspond to the data shown in Figure 2.1 (B). The raw data are in Table A.3.

Inner Square	**Mix**	**1.5 mm**	**3 mm**	**5mm**
Mean	1.2957	1.3305	1.9304	3.3996
Stand. Dev.	0.2002	0.2917	0.8111	0.9968
Stand. Error	0.1156	0.1684	0.4683	0.5755
Error Bar	[1.1801, 1.4113]	[1.1621, 1.4989]	[1.4621, 2.3986]	[2.8241, 3.9751]

Table 2.1: Virus load data, standard deviation, standard error and error bars.

Since the largest inner square is the 5 mm plate, we assume, for now, it corresponds to the separated case, i.e., $\langle K \rangle_a = 3.3996$, while the mixed case corresponds to the harmonic mean $\langle K \rangle_h = 1.2957$. To find K_S and K_W, we then simply solve the two equations for the means (2.15) to obtain:

$$K_W = 0.7252, \quad \text{and} \quad K_S = 6.0740.$$

To investigate the agreement with the intermediate cases of 1.5 mm and 3 mm, we solve the full PDE (2.4). For this, we also require the diffusion constant D and

the virus growth rate μ. From the data in Tables A.1 and A.2, we determined a range of values for the growth rate of the virus in weak and strong infectivity cells. Specifically, $\mu_W \in [0.1155, 0.3547]$ and $\mu_S \in [0.1155, 0.4722]$. Consequently, we opt for the intermediate value $\langle \mu \rangle_a = 0.23$ per hour.

We lack direct information from the data to estimate the value of the diffusion coefficient D. Rioja et al. [70] employed a similar spatial virus model for cancer viral therapy and utilized a diffusion coefficient of $D_{\text{Rioja}} = 0.0144$ mm^2 per hour. This corresponds to an invasion speed of $c = 0.115$ mm per hour, resulting in a distance traveled in 24 hours of 2.76 mm. However, this seems too small for our scenario. If the travel distance is only 2.76 mm in 24 hours, then the 3 mm and 5 mm cases would not effectively communicate viral load values over a 24-hour period. Therefore, to account for the observed homogenization effect, we anticipate a significantly larger diffusion coefficient than 0.0144.

Another way to evaluate the diffusion coefficient D is by applying the Stokes-Einstein equation for the diffusion coefficient D of a spherical particle of radius r in a fluid of dynamic viscosity η at absolute temperature T [161], which in our case becomes

$$D = \frac{k_B T}{6\pi\eta r} = 0.02\,\text{mm}^2 \text{ per hour},$$

where k_B is Boltzmann's constant, $r = 50\,\text{nm}$ is a typical virus radius size, and $\eta = 0.00094\ pa.\,s$ is the viscosity of DMEM (10 % FBS) medium at $T = 25^o C$ [162]. However, the simulation results show that this value is very low and it does not fit the data. We believe that a reason for this discrepancy is the formation of capillaries between cells that are touching along cell membranes. [163] showed that depending on the capillary pore size, the diffusivity could increase by orders of magnitude. Again, in our case we have no information about the pore sizes between the cells in our experiments.

Consequently, we treat the diffusion coefficient as an unknown variable and com-

pute the error (2.16) relative to the measurements.

In Table 2.2, we vary the virus diffusion coefficient D from 0.02 to 0.6 mm^2 per hour and solve the Fisher-KPP equation (2.4) as outlined in Section 2.5. We observe that as D increases, the fit for the 1.5 mm case improves, the 3 mm case fits consistently well, and the fit for the 5 mm case deteriorates. Ultimately, this naive procedure fails to yield a usable fit. We present the data for the case of $D = 0.5$ as a red curve in Figure 2.4 (A).

D	**0.02**	**0.05**	**0.1**	**0.3**	**0.5**	**0.6**	**Measurements**
Mix	1.2365	1.2365	1.2365	1.2365	1.2365	1.2365	1.2957 ± 0.1156
1.5mm	2.3060	2.0169	1.7582	1.4590	1.3800	1.3590	1.3305 ± 0.1684
3mm	2.5734	2.4397	2.2762	1.9069	1.7304	1.6737	1.9304 ± 0.4683
5mm	2.6757	2.6031	2.5175	2.2945	2.1431	2.0830	3.3996 ± 0.5755
Fitting Data	No	No	No	No	No	No	

Table 2.2: Simulated virus load data when D is varied at t=24 hour.

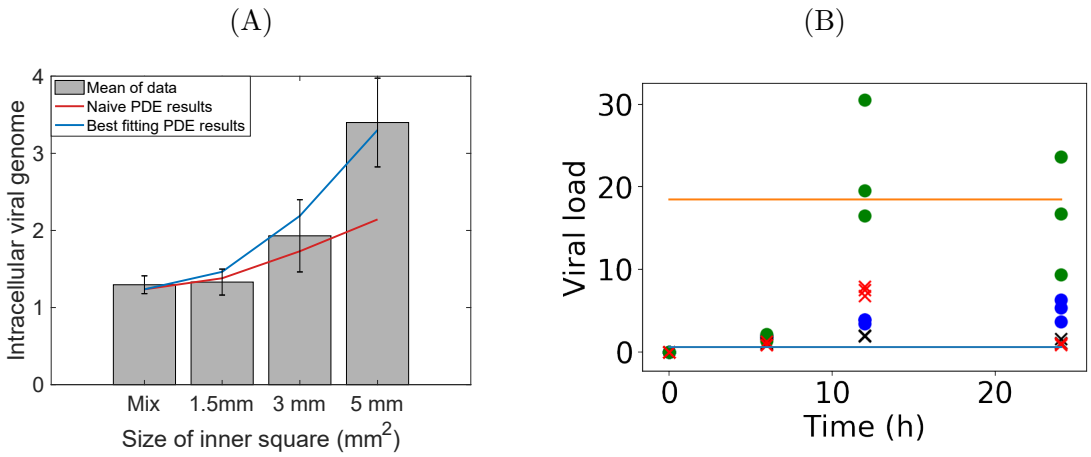

Figure 2.4: **(A):** Measurement values of virus load for the various checker board patterns. Overlaid is the naive fit for $D = 0.5$ in red and the best fit using a hypothetical 15 mm experiment in blue, **(B):** Comparison of the estimated carrying capacities K_W, K_S with the virus load data of each cell type in isolation. The horizontal lines indicate the levels $K_W = 0.6713$ (blue), and $K_S = 18.529$ (orange). The data from Tables A.1 and A.2 are presented as (X,black)= weak cells experiment 1, (X,red)= weak cells experiment 2, (circle,blue)= strong cells experiment 1 and (circle,green)=strong cells experiment 2.

2.4.1 Calibration II: Extension to a 15 mm Case

The discrepancy observed for the 5 mm plate may be attributed to the fact that the 5 mm squares are still relatively mixed, possibly not corresponding to the fully separated state. To test this hypothesis numerically, we introduce a hypothetical 15 mm case, where the cell types are segregated into one compartment for cells of weak infectivity and another compartment for cells of strong infectivity.

Although the corresponding virus load has not been measured due to technical limitations of the bio-printing method, we can still solve the PDE for this case. We set a maximum error tolerance of $E_{\max} = 0.1$, which corresponds to the smallest error bar from the data (see Table 2.1). Varying D within the range $[0.02, 0.6]\,\mathrm{mm}^2$ per hour and $K_{15\mathrm{mm}}$ within $[5.5, 12]$, we observe in Figure (2.5 (A)) that the error decreases with increasing D and $K_{15\mathrm{mm}}$. The first value below the error tolerance of 0.1 is achieved with $D = 0.5$ (indicated by the red marker in Figure 2.5 (A)). For larger values of D, the error can still be decreased. However, a full minimization is not very meaningful since the fitting errors become much smaller than the measurement errors of the data. With D fixed at 0.5, we find a suitable range of values for $K_{15\mathrm{mm}}$. A clear minimizer is found at $K_{15\mathrm{mm}} = 9.6$ with an error of $E = 0.0974$ (see Figure 2.5 (B)). Hence, for the purpose of our modeling, we choose

$$D = 0.5 \qquad \text{and} \qquad \langle K \rangle_a = K_{15\mathrm{mm}} = 9.600, \tag{2.17}$$

which, using (2.15) leads to

$$K_W = 0.6713, \qquad \text{and} \qquad K_S = 18.529. \tag{2.18}$$

These results suggest that strong infectivity cells can support about 25 times more virus than weak infectivity cells.

In Table 2.3 and Figure 2.4 (A), we compare the measured values to the optimized PDE results and also record the error and relative error when $K_{15\mathrm{mm}} = 9.6$ at $t = 24$. We observe that the model results closely match the measurements, falling well within

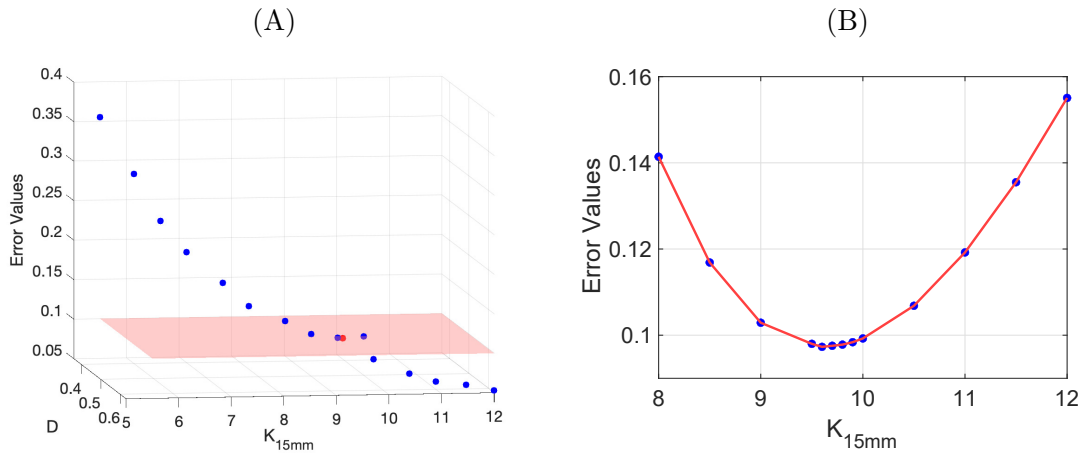

Figure 2.5: **(A)**: Error values at $24h$ when $K_{15\text{mm}}$ and D are varied. The red marker indicates $D = 0.5$ and $K_{15\text{mm}} = 9.6$ which we chose as most suitable model parameter, **(B):** Optimization of $K_{15\text{mm}}$ for fixed $D = 0.5$.

the error bars. Achieving such a high level of accuracy in fitting biological data is quite rare, bolstering our confidence that the chosen PDE model effectively explains the data. We summarize the calibrated model parameters in Table 2.4.

Size of Inner Square	**Measurement**	**PDE**	**Error^2**	**Relative Error**
Mix	1.2957	1.2365	0.0035	4.6 %
1.5mm	1.3305	1.4635	0.0177	10 %
3mm	1.9304	2.1889	0.0669	13.4 %
5mm	3.3996	3.3033	0.0093	2.8 %
Least Square Error			0.0974	

Table 2.3: Comparison of the measurements with the optimized PDE model.

We further utilize our optimized PDE model to investigate the virus load after 12 hours as well. For the mix, 1.5 mm, 3 mm, and 5 mm cases, we find simulated virus load numbers of 0.7372, 0.7643, 0.8183, and 0.8766, respectively. Although there is a slight increase from mixed to separated, the difference is small and would not be observable within measurement tolerances. Hence, the homogenization effect would not be observed after 12 hours, a finding corroborated by the experiments (experimental values not shown). The typical replication process of the virus inside

Parameter	Description	Value	Unit
D	Diffusion coefficient	0.5	mm^2 per hour
$\langle\mu\rangle_a$	Arith. mean growth of rate	0.23	per hour
K_W	Carrying capacity of weak infectivity cells	0.6713	viral load
K_S	Carrying capacity of strong infectivity cells	18.529	viral load
$K_{\text{Mix}} = \langle K\rangle_h$	Carrying capacity of mixed plate	1.2957	viral load
$K_{15\text{mm}} = \langle K\rangle_a$	Carrying capacity of 15 mm printed plate	9.600	viral load

Table 2.4: Summary of calibrated model parameters.

cells takes between 5 and 12 hours [164]. Therefore, at the 12-hour mark, only a few cells would have released their virus contents, and the homogenization effect will not yet have taken effect.

Furthermore, we compare these results (2.18) with the experiments of viral load infections on each cell type in isolation. In Figure 2.4 (B), we plot the virus load data from Tables A.1 and A.2 as functions of time. Symbols and colors distinguish between the cell types and experiments: (X, black) denotes weak cells experiment 1, (X, red) denotes weak cells experiment 2, (circle, blue) denotes strong cells experiment 1, and (circle, green) denotes strong cells experiment 2. Additionally, we plot the estimated K_W and K_S from (2.18) as horizontal lines.

We observe a substantial difference in the virus load data between experiments 1 and 2 for each of the weak and strong cases. Hence, the data do not appear to be directly comparable. The virus load of the strong responders is certainly one or two orders of magnitude larger than those of the weak responders, and our estimates reflect this fact nicely. However, the data do not permit a quantitative comparison.

2.5 Numerical Analysis of the PDE Model

In this section, we present the numerical scheme used to solve the homogenized equation and for the spatially printed plates.

2.5.1 Mix Plate

Since $\mu_S = \mu_W$, we can solve the homogenized equation (2.12) for Case 2 using a Forward-Time-Central-Space method [165]. As μ and K are constant and the initial condition is non-negative, the solution should converge to the carrying capacity $K_{\text{Mix}} = \langle K \rangle_h = 1.2957$, which has been confirmed numerically, as shown in Figure 2.6 (F).

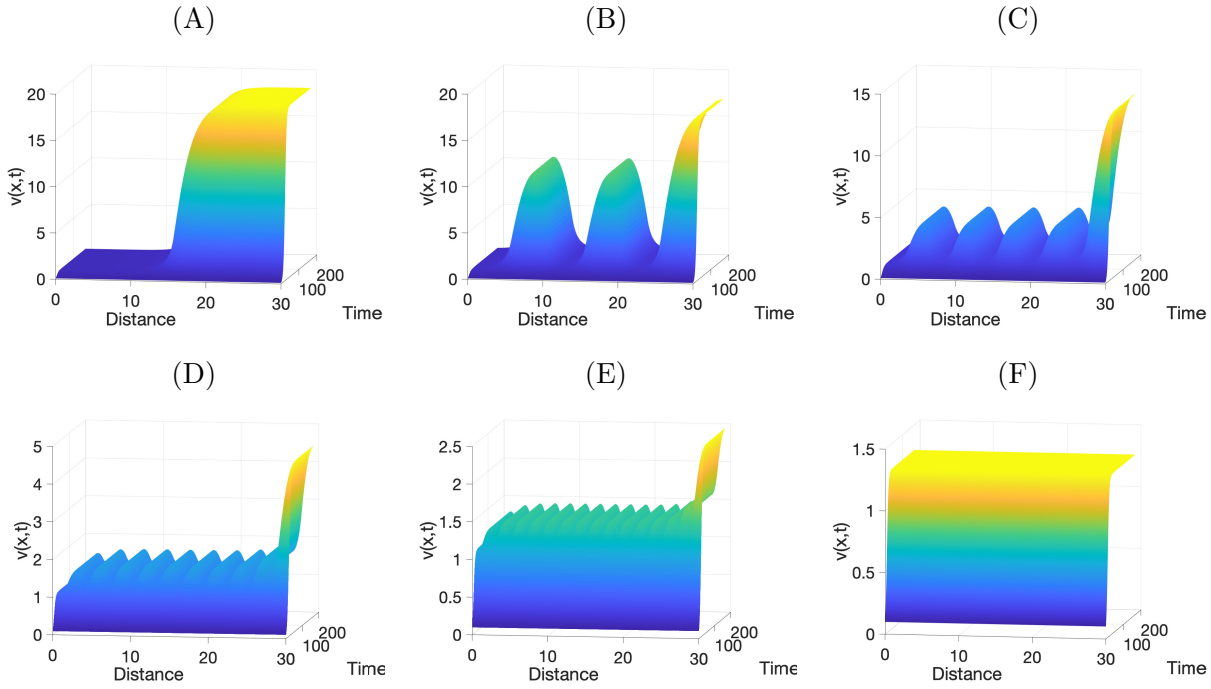

Figure 2.6: Numerical simulation when $\mu_S = \mu_W = 0.23$ and $D = 0.5$ with $v(x,0) = 0.1$, and $v_x(0,t) = v_x(30,t) = 0$ for **(A):** 15 mm intervals, **(B):** 5 mm intervals, **(C):** 3 mm intervals, **(D):** 1.5 mm intervals, **(E):** 1 mm intervals, **(F):** mix plate. Note that the z-axis changes between these figures.

2.5.2 Spatially Printed Plates

For the spatially printed plates, we consider two patch types, "strong" which represent strong infectivity cells and "weak" which represent weak infectivity cells. Accordingly, the carrying capacity is spatially constant within a patch but different between patches. While, the diffusion coefficient D and growth rate μ are the same in the two

patches. We partition the entire interval into sub-intervals ('patches') (y_{i-1}, y_i), $i \in \mathbb{N}$. Thus, we have

$$\frac{\partial v_i}{\partial t} = D\frac{\partial^2 v_i}{\partial y^2} + \mu_i v_i \left(1 - \frac{v_i}{K_i}\right), \text{ for } y \in (y_{i-1}, y_i).$$

Since the diffusion coefficient does not vary between the patches, the flux is continuous across an interface

$$\partial_y v(y_i^+, t) = \partial_y v(y_i^-, t).$$

Here, y_i^+ and y_i^- denote right and left sided limits at y_i. The probability of a virion at interface y_i moving to the right or left is the same and equal to 0.5. Thus

$$v(y_i^+, t) = v(y_i^-, t),$$

which ensures continuity of the solution at the interfaces.

The simulations in Figure 2.6 confirm our model assumption as only in the 15 mm case (Figure 2.6 (A)) the carrying capacity of $K_S = 18.529$ of the strong infectivity cells is reached. In the other simulations (B)-(F), the inner maxima, corresponding to the strong cell type, are much lower than the carrying capacity of 18. We see the homogenization effect in action, as the relative differences between local maxima and local minima are flattened for decreasing inner interval sizes. We also observe an overshoot at the right boundary, which is due to the chosen Neumann boundary conditions.

2.6 Conclusion

In this chapter, we employ the method of homogenization to analyze a spatially structured Fisher-KPP model concerning the virus-load in cell cultures during viral infections. While the method of homogenization is well-established in physics ([109]) and ecology ([139, 160]), our novel application focuses on microbiological data analysis. We have identified a biological scenario where the choice of averaging method is crucial. Both arithmetic and harmonic means offer valid insights into viral load,

yet they yield distinct results. Remarkably, this marks the first instance where the averaging method significantly impacts the infectivity assessment of cell populations.

These insights stem from groundbreaking inkjet bioprinting technology pioneered by Park et al. [151]. Beyond conventional checkerboard-patterns, this technique enables the generation and analysis of diverse patterns, such as the Eiffel Tower, facilitating the modeling of heterogeneous tissues like lung tissue.

Utilizing a calibrated PDE model, we have simulated scenarios not feasible experimentally, such as the 1 mm and 15 mm cases, and observed the homogenization effect after 12 hours. Notably, the viral load within the 1 mm inner square experiences a significant reduction compared to the 5 mm and 15 mm cases, closely aligning with mixed case measurements. Furthermore, employing the Fisher wave speed formula (2.5), we calculated the invasion speed in our experiment. For specific parameters, $D = 0.5$ and $\mu = 0.23$ we determined an invasion speed of $c = 2\sqrt{D\mu} = 0.68$ mm per hour, indicating virions cover a substantial distance within 24 hours, consistent with the homogenization assumption of considering two spatial scales.

While our observations derive from meticulously controlled experiments with well-defined geometric setups and cell types, the implications of population mixing versus segregation on total viral load likely extend to more natural tissue settings, such as viral therapy for cancer [70, 81]. We identified an eightfold increase in viral load from mixed to fully segregated populations, potentially impacting tissue response and patient health significantly. This finding underscores the potential relevance of our results, particularly in contexts such as COVID-19 mortality prediction, where even modest changes in viral load can influence outcomes significantly [166]. For example, in the recent study by [166] (Supplement Figure S1), on SARS-CoV-2 infection in France, a threshold of 10^6 was identified as a predictor of COVID-19 mortality. A factor 8, as we found here, can easily make a difference in the infection outcome. The spatial distribution of SARS-CoV-2 virus in tissue has been studied in [167], again, identifying to a highly heterogeneous lung tissue.

It's worth noting that although our model is one-dimensional spatially, while experiments are two-dimensional, we justify this simplification based on model symmetry, which adequately captures experimental trends within error tolerances.

However, there's room for refinement. While our model aligns with available data, incorporating additional viral infection dynamics like endocytosis, viral reproduction, and cell death could enhance its predictive power. Similarly, a more detailed formulation of virion transport, considering cellular membranes, fluid dynamics, and intracellular connections which are know to transport virions as well ([168]), might offer deeper insights. Nevertheless, our surprising biological finding suggests that spatial separation among cell sub-populations during viral infections might not be advantageous for overall cell population fitness, indicating that nature favors mixed populations to enhance fitness.

Chapter 3

Spatial Oscillations in Oncolytic Virotherapy

The material of this Chapter has been published as

- A.A. Baabdulla, and T. Hillen. Oscillations in a Spatial Oncolytic Virus Model. *Bulletin of Mathematical Biology*, 86:93, 2024.

3.1 Introduction

In Chapter 2, we investigate the impact of spatial heterogeneity on the viral load within heterogeneous cell populations. Continuing this exploration, the present chapter delves into the dynamics of viral infection within cancer cells, focusing on a treatment strategy known as virotherapy. Numerous mathematical models in virotherapy reveal oscillatory dynamics similar to predator-prey interactions, originating from an underlying Hopf bifurcation [66, 88]. Within a spatial framework, these oscillations give rise to a variety of spatio-temporal phenomena, such as *hollow-ring*, *target*, and *dispersed patterns* [81].

In this chapter, we further explore the systematic analysis of spatial oscillations and their significance in clinical applications. Through bifurcation analysis of a spatially explicit reaction-diffusion model, we aim to elucidate various spatio-temporal virus infection patterns previously mentioned. Specifically, our focus lies on identifying the hollow ring pattern, deemed optimal for tumor eradication, and determining precise

conditions for its manifestation. We opt for these interaction forms due to their widespread utilization in mathematical modeling, offering comprehensive insights into the dynamics of virotherapy.

Moreover, we derive the minimal speed of travelling invasion waves for the cancer and for the oncolytic virus. Our numerical simulations in 2-D reveal complex spatial interactions of the virus infection and a new phenomenon of a periodic peak splitting. An effect that we cannot explain with our current methods.

We start our analysis by employing Pooladvand et al.'s [88] adenovirus infection model in glioblastoma to investigate the propagation of the viral invasion wave and explicitly determine the minimum speed of the viral wave. Also, we will understand how the spatial distribution impacts the existence of a tumor free state. Furthermore, we relax the assumption of radial symmetry and we determine the conditions under which we can obtain the favorable viral infection pattern. We again find the spatial patterns of hollow ring, target patterns and dispersed patterns, which were reported in Wodarz [81] using an individual based model. We observe that during spatial oscillations, the number of cancer cells is close to 0 in certain parts of the domain. For these parts we compute the tumor control probability (TCP), which shows that a hollow ring structure can lead to a TCP close to 1, i.e. likely treatment success.

The structure of this chapter unfolds as follows: In Section 3.2, we introduce the mathematical model, expanding upon Pooladvand's reaction-diffusion model and conducting a non-dimensionalization process to simplify parameters. Moving to Section 3.3, we initially explore the ODE-version of our model, delineating steady states, their stability, and pinpointing two pertinent bifurcations: a transcritical bifurcation and a Hopf bifurcation. Subsequently, we establish the minimal invasion speed for the one-dimensional PDE version of the model. Section 3.4 is dedicated to an extensive numerical investigation, encompassing both 1D and 2D simulations. Here, we set base parameter values guided by Pooladvand's work [88] and compute tumor control probability for ODE simulations to gauge treatment outcomes. Confirming the theo-

retical wave speed from Section 3.3, we conduct simulations in 1D. In 2D simulations, intriguing viral spread patterns emerge, including coexistence steady states, hollow ring formations, and intricate spatio-temporal interactions. Finally, in Section 3.5, we offer concluding remarks, contextualizing our findings within the broader landscape of mathematical modeling and cancer research.

3.2 The Basic Assumptions and the Mathematical Model

In this section, we will study an extension of Pooladvand et al. [88] reaction diffusion model on a rectangular or smooth domain $\Omega \subset \mathbb{R}^n$ with the mass-action kintetics:

$$\begin{aligned} \frac{\partial C}{\partial t} &= D_C \Delta C + \tau C \left(1 - \frac{C+I}{L}\right) - \beta C V, \\ \frac{\partial I}{\partial t} &= D_I \Delta I + \beta C V - \alpha I, \\ \frac{\partial V}{\partial t} &= D_V \Delta V + \alpha b I - \omega V, \end{aligned} \tag{3.1}$$

where the density of susceptible tumor cells, infected tumor cells, and free viruses is denoted by $C(x,t)$, $I(x,t)$, and $V(x,t)$, respectively. The tumor growth rate is τ and L is the carrying capacity of tumor cells. The mass action term βCV describes the interaction between virus particles and the tumor cells. The infection rate is denoted by β. The death rate of infected cells is denoted by α. The burst size of the virus in infected cells is denoted by b, and ω is viral clearance rate. The diffusion coefficients of susceptible cells, infected cells, and viruses are denoted by D_C, D_I, D_V, respectively. The symbol Δ denotes the Laplacian, i.e. the sum of all second order derivatives.

In contrast to Pooladvand et al. [88], we deviate by relaxing the assumption of radial symmetry and Pooladvand et al. use a viral-loss term associated with the infection of cancer cells. We absorb this term in the viral clearance term ωV. We assert, in alignment with numerous other authors, that the quantity of virions binding to a cancer cell is significantly minor compared to the total count of free virus particles.

We consider system (3.1) with the initial conditions:

$$C(x,0) = C_0(x) > 0, \quad I(x,0) = 0, \quad V(x,0) = V_0(x) > 0, \tag{3.2}$$

and homogenous Nuemann boundary conditions on $\partial\Omega$:

$$n \cdot \nabla C(x,t) = n \cdot \nabla I(x,t) = n \cdot \nabla V(x,t) = 0, \qquad \text{for all} \quad x \in \partial\Omega,$$

where n denotes an outward normal at x at $\partial\Omega$. In the case of a rectangular domain some points will have several outer normal vectors. In that case we require the above boundary conditions for all normal vectors.

To simplify our analysis, we apply the non-dimensionalization method by considering

$$\hat{C} = \frac{C}{L}, \quad \hat{I} = \frac{I}{L}, \quad \hat{V} = \frac{\beta}{\tau}V, \quad \hat{t} = \tau t, \text{ and } \hat{x} = x\sqrt{\frac{\tau}{D_V}}.$$

After dropping the hat, we get the non-dimensional system:

$$\begin{aligned} \frac{\partial C}{\partial t} &= D_c \Delta C + C\,(1 - C - I) - CV, \\ \frac{\partial I}{\partial t} &= D_i \Delta I + CV - aI, \\ \frac{\partial V}{\partial t} &= \Delta V + \theta I - \gamma V, \end{aligned} \tag{3.3}$$

where

$$D_c = \frac{D_C}{D_V}, \quad D_i = \frac{D_I}{D_V}, \quad a = \frac{\alpha}{\tau}, \quad \theta = \frac{\alpha\beta b L}{\tau^2}, \text{ and } \gamma = \frac{\omega}{\tau}. \tag{3.4}$$

In the upcoming sections, our bifurcation parameter will be the effective viral production rate, denoted as θ. This parameter encompasses several crucial factors, including the death rate of infected cells (α), the burst size (b), the carrying capacity (L), and the cancer growth rate (τ). This comprehensive parameterization has been consistently highlighted in numerous mathematical modeling studies [66, 82, 93, 94, 97], signifying its importance in understanding the dynamics of virotherapy.

3.3 Analysis of the Model

3.3.1 Analysis of the Kinetic Part

We initially examine the aforementioned model in the spatially homogeneous scenario, where all spatial dependencies are disregarded. Consequently, the system governing $C(t), I(t), V(t)$ simplifies to:

$$\begin{aligned} \frac{dC}{dt} &= C\,(1 - C - I) - CV, \\ \frac{dI}{dt} &= CV - aI, \\ \frac{dV}{dt} &= \theta I - \gamma V. \end{aligned} \tag{3.5}$$

Similar systems have been extensively analyzed in existing literature [66, 81], where a Hopf bifurcation and subsequent oscillations are anticipated. Here, we provide a summary of these findings.

The system (3.5) has three steady states which are the trivial steady state $E_0 = (0, 0, 0)$, the pure cancer state $E_1 = (1, 0, 0)$ and a coexistence steady state

$$E_+ = (C^*, I^*, V^*) = \left(\frac{a\gamma}{\theta}, \quad \frac{\gamma(1 - C^*)}{\theta + \gamma}, \quad \frac{\theta(1 - C^*)}{\theta + \gamma} \right),$$

which exists in the positive quadrant for $0 < C^* < 1$. If θ is increased, the coexistence steady state arises through a transcritical bifurcation at

$$\theta_t = a\gamma. \tag{3.6}$$

We begin our analysis by computing the basic reproduction number, denoted as R_0. This metric serves as an epidemiological measure used to quantify the contagiousness or transmissibility of infectious agents, offering valuable insights into their spread dynamics. To determine R_0, we apply the next generation matrix method [169], utilizing the following approach:

$$F = \begin{bmatrix} 0 & 1 \\ \theta & 0 \end{bmatrix}, \qquad Z = \begin{bmatrix} a & 0 \\ 0 & \gamma \end{bmatrix}$$

where F is the transmission matrix and Z is the transition matrix. Thus, $R_0 = \frac{\theta}{a\gamma}$ is the spectral radius of FZ^{-1}. The coexistence steady state E_+ exists in the positive quadrant iff $\theta > a\gamma$, which is equivalent to $R_0 > 1$.

Now, we are prepared to investigate the stability of the steady states. We begin by computing the Jacobian matrix of system (3.5) as follows:

$$J = \begin{bmatrix} 1 - 2C - I - V & -C & -C \\ V & -a & C \\ 0 & \theta & -\gamma \end{bmatrix} \tag{3.7}$$

1. The Jacobian matrix of $E_0 = (0, 0, 0)$ is

$$J(E_0) = \begin{bmatrix} 1 & 0 & 0 \\ 0 & -a & 0 \\ 0 & \theta & -\gamma \end{bmatrix}$$

Therefore, the eigenvalues are $\lambda_1 = 1 > 0$, $\lambda_2 = -a < 0$, and $\lambda_3 = -\gamma < 0$. Thus, $E_0 = (0, 0, 0)$ is always unstable saddle.

2. The Jacobian matrix of $E_1 = (1, 0, 0)$ is

$$J(E_1) = \begin{bmatrix} -1 & -1 & -1 \\ 0 & -a & 1 \\ 0 & \theta & -\gamma \end{bmatrix}$$

with the characteristic equation $(\lambda + 1)(\lambda^2 + (a + \gamma)\lambda + a\gamma(1 - R_0) = 0$. The first eigenvalue is $\lambda_1 = -1 < 0$, the sign of second and third eigenvalues are determined by the value of R_0 of $\lambda^2 + (a + \gamma)\lambda + a\gamma(1 - R_0) = 0$.

Proposition 3.3.1 *The stability of steady state $E_1 = (1, 0, 0)$ with trace $= -(a + \gamma) < 0$, and determinant $= a\gamma(1 - R_0)$ is determined as the following:*

(a) If $R_0 < 1$, then λ_2 and λ_3 have the same sign since $\lambda_1\lambda_2 = a\gamma(1 - R_0) > 0$, but the trace is negative, therefore, λ_2 and λ_3 are both negative. Thus, E_1 is locally stable.

(b) If $R_0 > 1$, then λ_2 and λ_3 have different signs since $\lambda_1\lambda_2 = a\gamma(1-R_0) < 0$, therefore E_1 is always saddle.

3. The Jacobian matrix of $E_+ = (C^*, I^*, V^*)$ is

$$J(E_+) = \begin{bmatrix} -C^* & -C^* & -C^* \\ \frac{\theta(1-C^*)}{\theta+\gamma} & -a & C^* \\ 0 & \theta & -\gamma \end{bmatrix}$$

Proposition 3.3.2 *Consider system (3.5)*

1. *When $R_0 < 1$, we have two steady states E_0 and E_1 in the non-negative quadrant where E_0 is a saddle and E_1 is locally asymptotically stable.*

2. *When $R_0 > 1$, we have three steady states E_0, E_1, and E_+ in the non-negative quadrant where E_0 and E_1 are saddles.*

3. *The equilibrium point $E_+ = (C^*, I^*, V^*)$ is locally asymptotically stable if $\theta > \theta_t$ and $\kappa(\theta) > 0$, where $\kappa(\theta) = -\theta^3 + m\theta^2 + \gamma m\theta + a\gamma^3$, and $m = (a+\gamma)^2 + a(\gamma+1)$.*

4. *There exists a value $\theta_H > \theta_t$ with $\kappa(\theta_H) = 0$ such that system (3.5) undergoes a Hopf bifurcation at θ_H.*

Proof. The third and fourth items are not so obvious and we give some details here. The Jacobian at E_+ is

$$J(E_+) = \begin{bmatrix} -C^* & -C^* & -C^* \\ \frac{\theta(1-C^*)}{\theta+\gamma} & -a & C^* \\ 0 & \theta & -\gamma \end{bmatrix}$$

with the characteristic equation given by $\lambda^3 + P_2\lambda^2 + P_1\lambda + P_0 = 0$, where

$$\begin{aligned} P_2 &= C^* + a + \gamma, \\ P_1 &= C^*\left(a + \gamma + \frac{\theta(1-C^*)}{\theta+\gamma}\right), \\ P_0 &= \theta C^*(1-C^*). \end{aligned}$$

Based on Routh-Hurwitz criterion, the equilibrium point $E_+ = (C^*, I^*, V^*)$ is locally asymptotically stable if $\theta > \theta_t$ and the following conditions hold:

$$P_2 > 0;\ P_1 > 0;\ P_1P_2 - P_0 > 0;$$

It is clear that P_2, P_1, and P_0, are positive when $0 < C^* < 1$. It remains to show that $P_2P_1 - P_0 > 0$. We find

$$P_2P_1 - P_0 = C^* \left[C^*(a+\gamma) + (a+\gamma)^2 + \frac{\theta(1-C^*)(C^*+a-\theta)}{\theta+\gamma} \right] \tag{3.8}$$

Substituting $C^* = \frac{a\gamma}{\theta}$ in equation (3.8), and after simplifications and re-arrangements, we get

$$\begin{aligned} & P_2P_1 - P_0 = \frac{a\gamma}{\theta^2(\theta+\gamma)}\kappa(\theta), \\ \text{with} \quad & \kappa(\theta) = -\theta^3 + m\theta^2 + \gamma m\theta + a\gamma^3, \text{ and } m = (a+\gamma)^2 + a(\gamma+1) > 0. \end{aligned} \tag{3.9}$$

Since $\frac{a\gamma}{\theta^2(\theta+\gamma)} > 0$, and $\theta \neq 0$, the stability of the coexistence steady state E_+ is determined by the sign of $\kappa(\theta)$ after fixing the parameters a and γ.

To show the Hopf-bifurcation in item 4, we define

$$H(\theta) := P_2(\theta)P_1(\theta) - P_0(\theta)$$

and use Liu's criterion [142, 143] Theorem 1.2.9, which states: Assume that $P_0 \neq 0$. A Hopf bifurcation occurs at $\theta = \theta_H$ for the system (3.5) when the two following conditions are satisfied: $H(\theta_H) = 0$, and $\frac{dH}{d\theta}|_{\theta_H} \neq 0$. From (3.9) we have

$$H(\theta) = \frac{a\gamma}{\theta^2(\theta+\gamma)}\kappa(\theta).$$

Thus, $H(\theta) = 0$ iff $\kappa(\theta) = 0$. Based on Descartes' rule of signs, we have one positive real root and 2 or zero negative real roots. Since θ is a positive real number, there is a unique value of $\theta = \theta_H$, where $H(\theta_H) = 0$. We also note that the leading order term in $H(\theta)$ is negative. This means for all $\theta > \theta_H$ we have $\kappa(\theta) < 0$, which implies $\theta_t < \theta_H$.

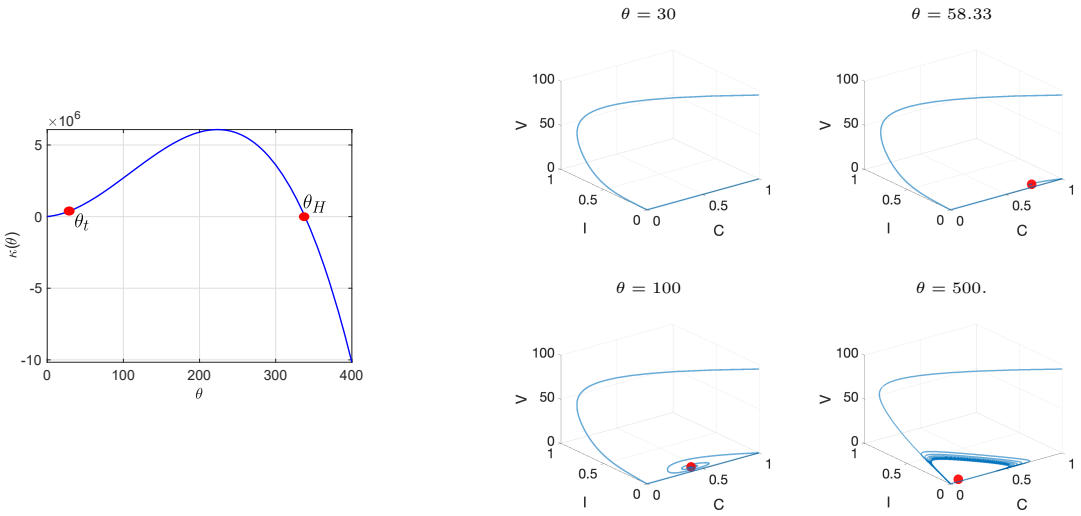

Figure 3.1: Left: Plot of the function $\kappa(\theta)$ from (3.9) for parameter values from Table 3.1. The two bifurcation points $\theta_t = 44.45$ for transcritical and $\theta_H = 338.45$ for Hopf bifurcation are indicated. Right: Numerical simulation of model (3.3) with different θ values with initial conditions C=1, I=0, and V=95. The coexistence steady state is indicated in red.

To obtain the direction of bifurcation we differentiate $H(\theta)$ as

$$\frac{dH}{d\theta} = -\frac{a\gamma[(\gamma+m)\theta^3 + 2m\gamma\theta^2 + (3a\gamma^3 + m\gamma^2)\theta + 2a\gamma^4]}{\theta^3(\theta+\gamma)^2}.$$

$\frac{dH}{d\theta} = 0$ iff $(\gamma+m)\theta^3 + 2m\gamma\theta^2 + (3a\gamma^3 + m\gamma^2)\theta + 2a\gamma^4 = 0$. Again, using Descartes' rule of signs, we find all the coefficients of θ's are positive. Therefore, we have a no positive real roots. Thus, $\frac{dH}{d\theta} \neq 0$ for any θ. Satisfying the Hopf bifurcation conditions. □

We plot $\kappa(\theta)$ and the two bifurcation points θ_t and θ_H in Figure 3.1 with parameters from Table 3.1. In Figure 3.1 we also show some typical simulations of (3.5) with parameters from Table 3.1, for increasing values of θ. In this case $\theta_t = 44.45$ and $\theta_H = 338.45$. We see that as θ increases past θ_t the coexistence steady state shows up (red dot), which becomes unstable to oscillations as we pass θ_H.

3.3.2 Wave Fronts of Glioma and Virus

In this section, we compute the invasion wave front of the spatial oncolytic virus model (3.3) in one spatial dimension by using a leading edge analysis. The domain is $(-\infty, \infty)$ and we consider first the tumor in isolation

$$\frac{\partial C}{\partial t} = D_c \frac{\partial^2 C}{\partial x^2} + C(1 - C), \tag{3.10}$$

with boundary conditions

$$C(-\infty, t) = 1, \qquad \text{and} \qquad C(\infty, t) = 0.$$

The standard traveling wave problem is to ask for a tumor invasion front into healthy tissue by considering a self-similar solution of the form $C(z)$ with $z = x - c_c t$ that solves (3.10) [108]. Here $c_c \geq 0$ denotes the wave speed. Using the above wave ansatz, we derive a coupled ODE system for $C(z)$ and $C'(z)$ and our task is to find a heteroclinic connection from $(1, 0)$ to $(0, 0)$ in phase space. To find such a connection we linearize at $(0, 0)$ and obtain a relationship between the wave speed c_c and an exponential decay rate λ_c, which is called the characteristic equation and can be written as

$$G(\lambda_c; c_c) = 0 \quad \text{with} \quad G(\lambda_c; c_c) = D_c \lambda_c^2 - c_c \lambda_c + 1. \tag{3.11}$$

The minimum wave speed is the value such that $G = 0$ still has a real solution, i.e.

$$c_c^* = 2\sqrt{D_c}. \tag{3.12}$$

For later use we also linearize at the point $(1, 0)$ in phase space. This point is a saddle point, i.e. it has a stable manifold along which solutions converge to $(1, 0)$. The wave speed $\tilde{c}_c$ and the exponential decay rate on the stable manifold $\tilde{\lambda}_c$ are related as

$$D_c \tilde{\lambda}_c^2 - \tilde{c}_c \tilde{\lambda}_c - 1 = 0. \tag{3.13}$$

Note the opposite sign of the 1-term as compared to (3.11). For $\tilde{\lambda} > \sqrt{D_c}^{-1}$ this equation has a solution for $\tilde{c}_c$. However, in phase space for (C, C') the unstable

manifolds of $(1,0)$ do not connect to the other steady state $(0,0)$. In fact, going backwards in time they diverge to ∞ or $-\infty$ and are not suitable solutions to our problem. Hence the condition (3.13) does not lead to a suitable invasion front.

To consider the invasion of the virus population into an established tumor, we linearize (3.3) in one dimension at the homogeneous steady state $(1,0,0)$ and obtain

$$\begin{aligned} \frac{\partial C}{\partial t} &= D_c \frac{\partial^2 C}{\partial x^2} - C - I - V, \\ \frac{\partial I}{\partial t} &= D_i \frac{\partial^2 I}{\partial x^2} - aI + V, \\ \frac{\partial V}{\partial t} &= \frac{\partial^2 V}{\partial x^2} + \theta I - \gamma V. \end{aligned} \tag{3.14}$$

We now make an explicit ansatz of an exponentially decaying self-similar wave solution as

$$(C(x,t), I(x,t), V(x,t)) = \left(\epsilon_c\, e^{-\lambda z}, \epsilon_i\, e^{-\lambda z}, \epsilon_v\, e^{-\lambda z}\right), \quad \text{where} \quad z = x - ct. \tag{3.15}$$

Here c denotes the wave speed and λ the exponential decay rate at the wave front. Substituting ansatz (3.15) into system (3.14), we get

$$\begin{aligned} c\lambda\epsilon_c e^{-\lambda z} &= D_c\lambda^2\epsilon_c e^{-\lambda z} - \epsilon_c e^{-\lambda z} - \epsilon_i e^{-\lambda z} - \epsilon_v e^{-\lambda z}, \\ c\lambda\epsilon_i e^{-\lambda z} &= D_i\lambda^2\epsilon_i e^{-\lambda z} - a\epsilon_i e^{-\lambda z} + \epsilon_v e^{-\lambda z}, \\ c\lambda\epsilon_v e^{-\lambda z} &= \lambda^2\epsilon_v e^{-\lambda z} + \theta\epsilon_i e^{-\lambda z} - \gamma\epsilon_v e^{-\lambda z}, \end{aligned}$$

which after simplification can be written as a linear system

$$\begin{bmatrix} D_c\lambda^2 - c\lambda - 1 & -1 & -1 \\ 0 & D_i\lambda^2 - c\lambda - a & 1 \\ 0 & \theta & \lambda^2 - c\lambda - \gamma \end{bmatrix} \begin{bmatrix} \epsilon_c \\ \epsilon_i \\ \epsilon_v \end{bmatrix} = \begin{bmatrix} 0 \\ 0 \\ 0 \end{bmatrix}. \tag{3.16}$$

The characteristic equation of (3.16) is

$$\left(D_c\lambda^2 - c\lambda - 1\right)\left[D_i\lambda^4 - c(D_i+1)\lambda^3 + (c^2 - D_i\gamma - a)\lambda^2 + c(\gamma + a)\lambda + a\gamma - \theta\right] = 0. \tag{3.17}$$

The first factor of (3.17) is the same as (3.13) and corresponds to unsuitable orbits in phase space. Hence we can focus on the second factor

$$\Phi(\lambda; c) = D_i\lambda^4 - c(D_i + 1)\lambda^3 + (c^2 - D_i\gamma - a)\lambda^2 + c(\gamma + a)\lambda + a\gamma - \theta. \qquad (3.18)$$

From $\Phi(\lambda; c) = 0$ we can find the wave speed values $c(\lambda)$ as functions of λ. To find the minimum wave speed of the virus, we use implicit differentiation

$$\frac{d}{d\lambda}\Phi(\lambda; c(\lambda)) = 0$$

to find conditions for $c'(\lambda) = 0$. We have

$$\begin{aligned} 0 &= \frac{d}{d\lambda}\Phi(\lambda; c(\lambda)) \\ &= \left(2\lambda^2 c + (\gamma + a)\lambda - (D_i + 1)\lambda^3\right) c'(\lambda) \\ &\quad + 4D_i\lambda^3 - 3c(D_i + 1)\lambda^2 + 2(c^2 - D_i\gamma - a)\lambda + c(\gamma + a), \end{aligned}$$

which can be solved for c' as

$$c'(\lambda) = \frac{\Psi(\lambda; c)}{2c\lambda^2 - (D_i + 1)\lambda^3 + (\gamma + a)\lambda},$$

with

$$\begin{aligned} \Psi(\lambda; c) &= 2\lambda c^2 + \eta_1 c + \eta_0, \\ \eta_1 &= \gamma + a - 3(D_i + 1)\lambda^2, \\ \eta_0 &= 4D_i\lambda^3 - 2(D_i\gamma + a)\lambda. \end{aligned}$$

Thus, $c'(\lambda) = 0$, iff $\Psi(\lambda; c) = 0$.

Hence the minimum wave speed c^* arises at the intersection of the two manifolds

$$\{\Phi(\lambda; c) = 0\} \quad \text{and} \quad \{\Psi(\lambda; c) = 0\}.$$

For the parameter values from Table 3.1 we plot these two curves in a (λ, c)-diagram in Figure 3.2. In that case we find a unique intersection at

$$\lambda^* \approx 1.5728 \qquad \text{and} \qquad c^* \approx 0.9299, \qquad (3.19)$$

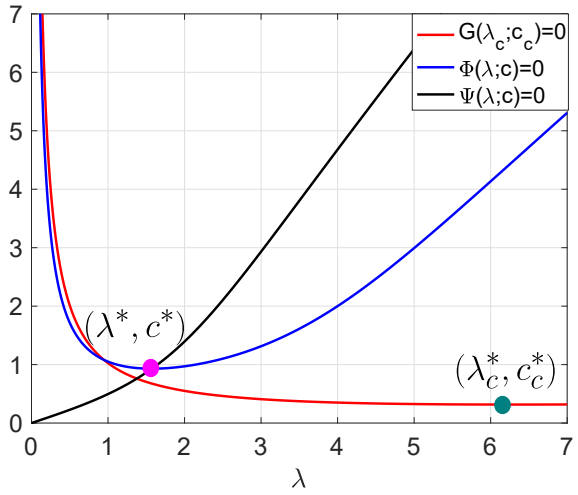

Figure 3.2: The characteristic equation of the tumor and virus as implicit function with respect to λ and c. The green circle is the minimum decay rate and corresponding minimum wave speed of tumor cells. The pink circle is the minimum decay rate and corresponding minimum wave speed of the virus particles. The parameters values are in Table 3.1.

which is indicated in Figure 3.2. These values should be compared to the tumor invasion speed in isolation, which according to (3.12) is

$$c_c^* = 2\sqrt{0.025} = 0.3162.$$

3.4 Numerical Analysis

In this section, we present the numerical outcomes of our model. Initially, we elucidate the rationale behind selecting model parameters in Section 3.4.1. Subsequently, in Section 3.4.2, we depict the bifurcation trajectory of the ODE model (3.3). The trivial steady state becomes unstable to a transcritical bifurcation at θ_t, followed by oscillations post a Hopf bifurcation at θ_H. In Section 3.4.3, we delve into the discussion of the tumor control probability (TCP), demonstrating that after one oscillation cycle, the tumor can be deemed eradicated. In Section 3.4.4, we examine the aforementioned model (3.3) within a one-dimensional context, confirming the theoretical

wave speeds previously derived. Moving on to Section 3.4.5, simulations conducted on a two-dimensional domain are presented. Herein, we observe the anticipated spread patterns including uniform spread, and hollow-ring patterns, as reported previously. Furthermore, beyond the Hopf point, for values of θ substantially distant, unpredictable and chaotic patterns emerge, attributable to spatial interactions of coupled oscillators via spiral waves and oscillating target patterns. Here we only touch on the rich variety of patterns that our system can generate and we leave a more complete analysis of this pattern regime for future work.

3.4.1 Parameter Values

The parameters values that have been used in the simulations are presented in Table 3.1. These parameter values were used by Pooladvand et al. [88] in their study of adenovirus infections of a solid tumor. Based on Lodish [170], Pooladvand et al. [88] consider the carrying capacity of a solid tumor of radius 1 mm is about $L = 10^6$ cells/mm^3, which is also the initial density of uninfected tumor cells $C_0(x)$ in our model. Based on Kim's et al [41] experiments on adenovirus in a glioblastoma U343 cell line, a tumor growth rate is estimated as $\tau = 0.3$ per day, and a tumor diffusion coefficient as $D_C = D_I = 0.006\text{mm}^2$ per day. The initial condition for the amount of adenovirus virions is $V_0 = 1.9 \times 10^{10}$ virions per mm^3. For the viral diffusion coefficient, Pooladvand et al. [88] used the same value that has been employed in [74] which is $D_V = 0.24$ mm^2 per day. Since the infected cells lyse on average after 24 hours of injection [171], the death rate of infected cells is about $\alpha = 1$ per day. The clearance rate of the virus has been estimated from [172] to be $\omega = 4$ per day. The infection rate parameter β has been estimated based on Friedman's et al. [82] paper to be $\beta = 1.5 \times 10^{-9}$ per (virus $\times$ day). Due to the importance of this parameter, Pooladvand et al. [88] varied the values of β from low to high, i.e $\beta \in [10^{-9}, 5 \times 10^{-9}]$ to investigate its impact on the treatment outcome. Shashkova et al. [173] estimated the adenovirus burst size b and found it varied between 1,000-100,000 virions per cell.

Recently, Chen et al. in their paper [174] measured the burst size of adenovirus to be 3500 virions per cell, which is the value Pooladvand et al. [88] and we consider.

In the virotherapy treatment the crucial parameters for successful treatment are the infection rate β and the viral burst size b. Therefore, in this paper, we will focus on the effective virus production rate parameter θ from (3.4), which includes these two parameters. Thus, using the values in Table 3.1, we have the base value of $\theta = 58.33$. However, we will use θ as a bifurcation parameter in our study. Therefore, fixing the parameters L, τ, α, and w, as in Table 3.1, and varying β and b, we find the effective virus production rate θ is ranged between 11.1111-5555.55.

Parameter	**Value**	**Units**	**Description**
$C_0(x)$	10^6	cells per mm^3	Initial density of uninfected cells
$V_0(x)$	1.9×10^{10}	viruses per mm^3	Initial density of virus particles
D_C	0.006	mm^2 per day	Diffusion coefficient of susceptible cells
D_I	0.006	mm^2 per day	Diffusion coefficient of infected cells
D_V	0.24	mm^2 per day	Diffusion coefficient of viruses
τ	0.3	per day	Growth rate of tumor cells
L	10^6	cell per mm^3	Carrying capacity of tumor cells
β	1.5×10^{-9}, variable	per (virus $\times$ day)	Infection rate of mass action case
α	1	per day	Death rate of infected cells
b	3500, variable	virus per cell	Burst size of viruses
ω	4	per day	Clearance rate of viruses

Table 3.1: Summary of model (3.1) parameters. All the parameters values used from reference [88].

After rescaling (3.4), the parameter values for model (3.3) are given in Table 3.2.

Rescaled Parameter	Meaning	Value
D_c	cancer diffusion coefficient	0.025
D_i	infected cells diffusion	0.025
a	infected death rate	3.33
γ	virus decay rate	13.33
θ	effective virus production rate	[0,500]

Table 3.2: Base parameter values of the rescaled model (3.3) using the rescaling (3.4). These parameters are unitless.

3.4.2 ODE Model

We start by examining the ODE system (3.3) with θ as a bifurcation parameter, derived from (3.4), where θ denotes the effective virus production rate. Figure 3.1 illustrates the dynamic behavior of model (3.3) utilizing parameters from Table 3.2 while varying θ. The initial conditions across all four simulations are set to $(C(0), I(0), V(0)) = (1, 0, 95)$. In Figure 3.3, we present cases for $\theta = 58.33, 100, 500$ plotted as functions of time. The transcritical bifurcation manifests at $\theta_t = 44.45$, leading to a coexistence steady state for $\theta > \theta_t$. The Hopf bifurcation occurs at $\theta_H = 338.45$ and we obtain periodic orbits beyond that point. Oscillations arise already for $\theta < \theta_H$. Biologically, the cancer-virus dynamic resembles a predator-prey system, where periodic orbits and Hopf bifurcations are common characteristics of such models.

It's noteworthy that the trivial steady state $(0, 0, 0)$ is consistently unstable in all scenarios. Consequently, from a mathematical standpoint, complete eradication of the cancer is unattainable. However, the periodic orbits closely approach $(0, 0, 0)$, to the extent that a stochastic viewpoint utilizing the tumor control probability, as discussed in Section 3.4.3, becomes pertinent.

Before we proceed further, we briefly explore the influence of other model parameters.

In Figure 3.4, we vary the virus decay rate γ from its baseline value of $\gamma = 13.33$,

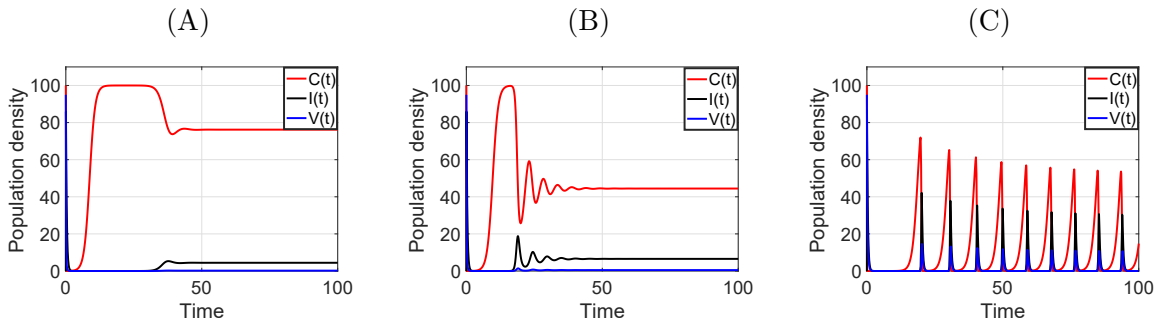

Figure 3.3: Numerical simulation with different θ values with initial conditions (1, 0, 95). Here, the susceptible and infected cells are re-scaled by multiplying with 100. **(A):** $\theta = 58.33$, **(B):** $\theta = 100$, and **(C):** $\theta = 500$.

exploring values $\gamma = 6.67, 10, 16.67$. We observe a positive impact on cancer reduction with a reduced virus decay rate. Although the bifurcation structure remains largely unchanged for different γ values, oscillation frequencies shift from low frequency for $\gamma = 6.67$ to high frequency for $\gamma = 16.67$.

Moving to Figure 3.5, we vary the removal rate of infected cells a from its base value $a = 3.33$, incorporating $a = 6.67, 10, 13.33$. Here, we notice a strong dependency of bifurcations on the value of a. Increased removal rate leads to the loss of oscillations at $\theta = 500$, with convergence towards a coexistence steady state. Intriguingly, elevating the removal rate of infected cells a raises the value of the transcritical bifurcation point $\theta_t = a\gamma$. Such a shift alters treatment outcomes, as depicted in Figure 3.5. This observation aligns with the findings of Bhatt et al. [97], where increasing the death rate of infected cells results in treatment failure. Additionally, Bhatt et al. [97] identified the presence of resistant cancer cells as a contributing factor to treatment failure. In our model, addressing this can be achieved through a reduced infection rate β. A reduction in β lowers θ, effectively moving the system to a lower virus production rate, thereby facilitating easier cancer growth.

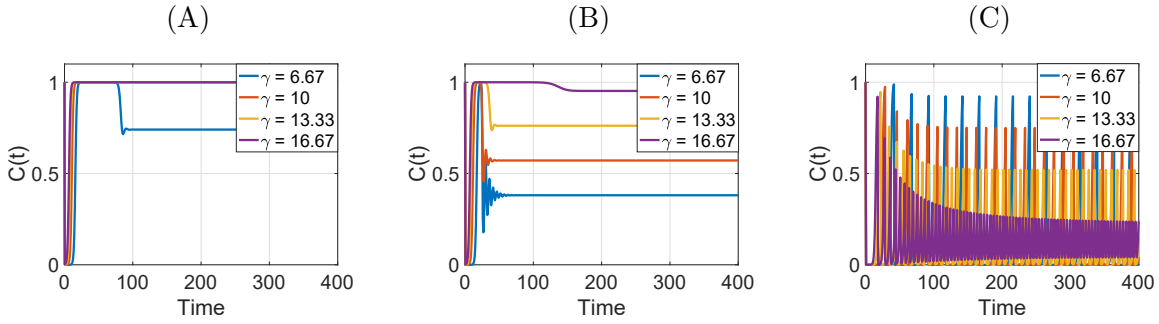

Figure 3.4: The tumor values as function of time with different γ values with $a = 3.33$ when **(A):** $\theta = 30$, **(B):** $\theta = 58.33$, **(C):** $\theta = 500$.

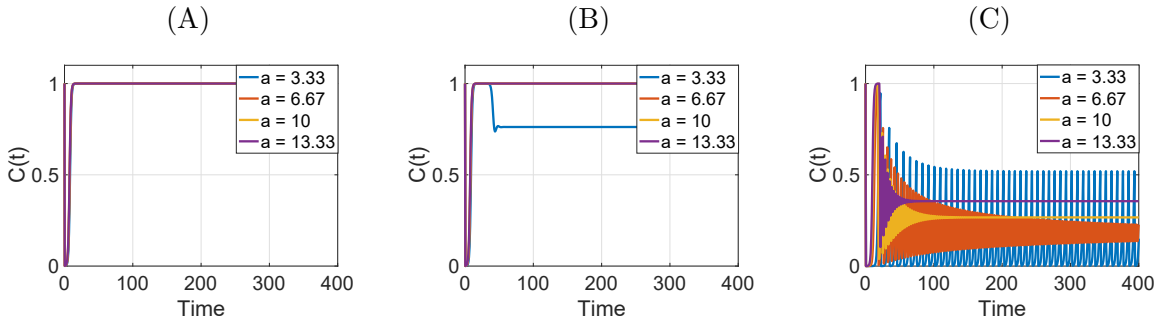

Figure 3.5: The tumor values as function of time with different a values with $\gamma = 13.33$ when **(A):** $\theta = 30$, **(B):** $\theta = 58.33$, **(C):** $\theta = 500$.

3.4.3 Tumor Control Probability

Our primary objective is tumor eradication. Although the extinction steady state $(0, 0, 0)$ is unstable for model (3.3) when $\theta > \theta_t$, complete eradication of cancer cells is unattainable. However, we observe that during the oscillations described previously, the density of tumor cells approaches zero closely. In such instances, we enter a realm where stochastic events become significant, and a deterministic description via an ODE model might prove insufficient. Stochastic models for tumor eradication have been developed, particularly in the context of cancer radiation therapy [16, 144, 175, 176]. The tumor control probability (TCP) serves as a metric for assessing the expected success of a given treatment. Gong et al. [144] compared various formulations for TCP and concluded that the simplest version, the Poissonian TCP, serves as a reasonable first-order approximation. Therefore, in this context, we adopt the Poissonian TCP. Let C_0 denote the initial number of tumor cells, and $C(t)$ those that survive at time t, then

$$S(t) = \frac{C(t)}{C_0} \tag{3.20}$$

denotes the survival fraction and the Poissonian TCP is given as

$$TCP(t) = e^{-C_0\, S(t)}. \tag{3.21}$$

The initial number of tumor cells $C_0 = 10^6$ corresponds to $C_0 = 1$ after non-dimensionalization. We examine three distinct cases of $\theta = 58.33, 350, 500$, and depict the TCP as a function of time in Figure 3.6. In the baseline scenario of $\theta = 58.33$, the TCP initially approaches 1 and subsequently stabilizes at a moderate value around 0.45.

For $\theta = 350$ and 500, lying beyond the Hopf point, we observe plateaus at TCP=1 for prolonged durations immediately following virus infection treatment. This indicates that the TCP reaches 1 after the initial cycle, implying successful treatment.

Subsequent oscillations, though present mathematically, become irrelevant for treatment outcomes. We revisit this aspect when discussing the two-dimensional simulations.

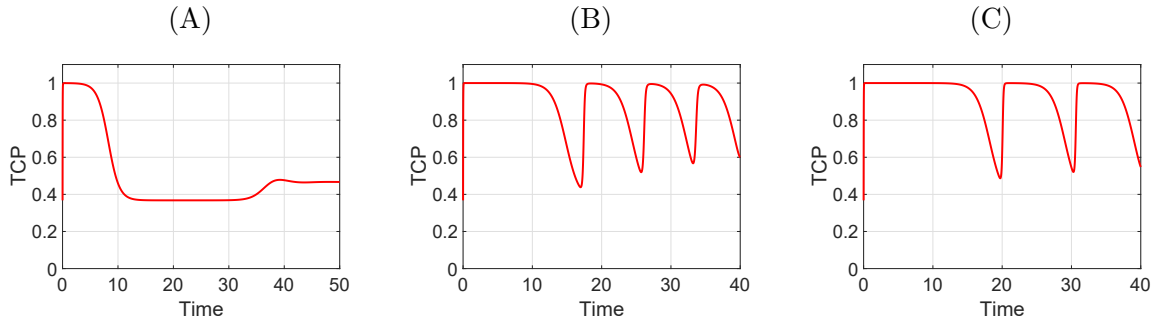

Figure 3.6: TCP values of tumor cells when θ is beyond the Hopf bifurcation value at $a = 3.33$ and $\gamma = 13.33$. **(A):** $\theta = 58.33$, **(B):** $\theta = 350$, and **(C):** $\theta = 500$.

3.4.4 PDE Model 1-D

As we understand the Hopf bifurcation of the ODE model well, it is interesting to see how the oscillations manifest themselves in the spatial context. It is known through the influential Kuramoto model [177] that spatially coupled oscillators can lead to all kind of dynamics such as ring patterns, target patterns, spirals and chaotic patterns [177, 178]. Those models have been applied with success in neurophysiological oscillations [179, 180], for example. We like to explore here if our model is also able to generate interesting patterns and evaluate them in the context of cancer treatment.

Starting in 1-D we consider an interval $[0, 60]$ and run simulations up to time 60. In dimensional parameters this corresponds to an interval of length 54 mm and a time of up to 200 days. Initially the virus particles are injected in the center of the domain. We chose zero-flux boundary conditions. The simulations are seen in Figure 3.7. The cancer cell density $C(x, t)$ in (A) and (D) is shown in colors of brown, where dark color corresponds to maximum tumor cell density. The infected cells $I(x, t)$ in (B) and (E) are shown in shades of blue, with dark blue indicating low density of infected cell. In (C) and (F) we show the virus load in colors from blue (low) to red

(high). In Figure 3.7 (A), (B) and (C), we chose $\theta = 58.33$, i.e. $\theta_t < \theta < \theta_H$.

The initial virus infection grows out from the centre of the domain and forms a travelling wave profile. After the wave has passed (around time 40) the system reaches a homogeneous coexistence steady state. We can use this simulation to estimate the travelling wave speed (slope of the ridges in (A),(B),(C)) as $c_v = 0.9428$, while the theoretical wave speed (3.19) is $c^* = 0.9299$, which is a good match. On the other hand, when $\theta = 500$, we are past the Hopf-point and we see oscillations in Figure 3.7 (D), (E) and (F). The oscillation synchronises spatially until it becomes a fully spatially homogeneous oscillation (long term dynamics not shown).

We perform the same simulations with a different initial condition in Figure 3.8 (A),(B),(C). Here we randomly chose five inoculation points along the interval $[0, 60]$. For $\theta = 58.33$ in (A) we see an initial interaction of the spread waves, which quickly find the coexistence steady state. For $\theta = 350$ in (B) and $\theta = 500$ in (C) we again see synchronized oscillations across the domain.

As in the ODE model the oscillations get very close to zero, indicating very low cancer and virus concentrations. Hence again, we employ the tumor control probability (3.21) to estimate the expected treatment success. In the spatial context we integrate over space to get the total surviving fraction of cancer cells. Then the TCP becomes

$$TCP(t) = e^{-\int_0^l C(x,t)dx}, \tag{3.22}$$

where we use the time point where the cancer concentration C is minimal.

For the cases where we inject the oncolytic virus in the center of the domain we find that the maximal TCP value is 0 for $\theta = 58.33$, 0.2598 for $\theta = 350$, and 0.9753 for $\theta = 500$. The TCP values were generally higher when the tumor was injected at five random locations with TCP of 0 for $\theta = 58.33$, 0.8103 for $\theta = 350$, and 0.9944 at $\theta = 500$. This clearly shows that for the base value of $\theta = 58.33$ treatment failure is expected. Only if θ is increased beyond the Hopf point we can expect good treatment

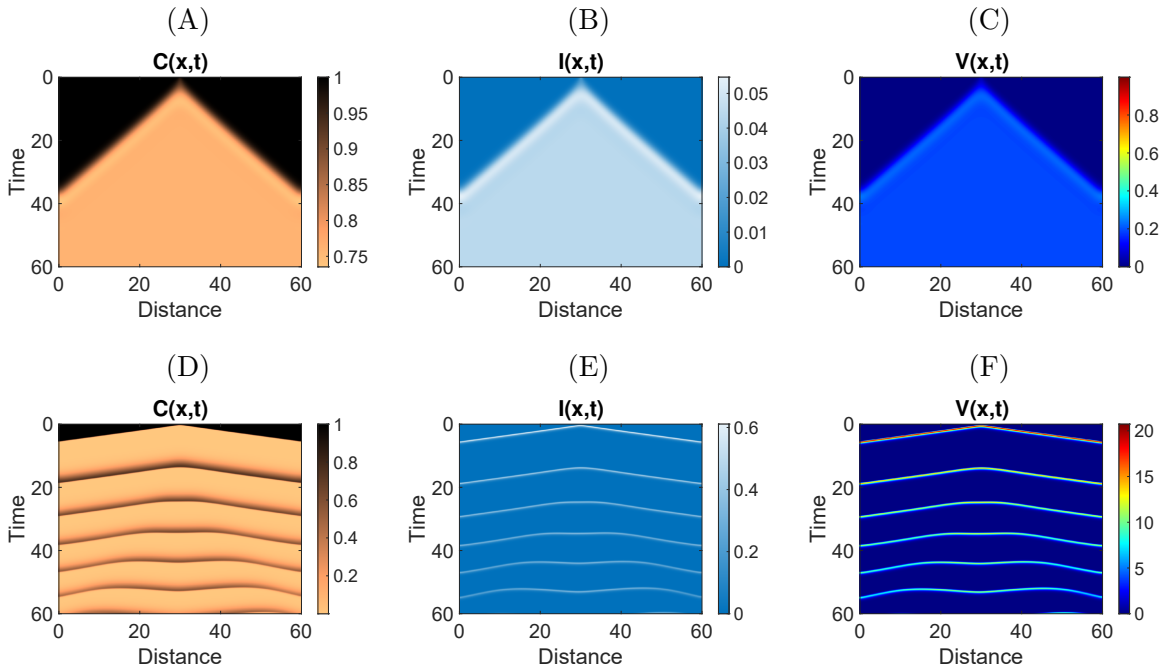

Figure 3.7: 1-D simulations with virus particles injected in the tumor center. The spatial distribution of the susceptible cells, infected cells and the virus with different values of θ with $a = 3.33$ and $\gamma = 13.33$. $\theta = 58.33$ for **(A)**, **(B)** and **(C)** and $\theta = 500$ for **(D)** **(E)** and **(F)**.

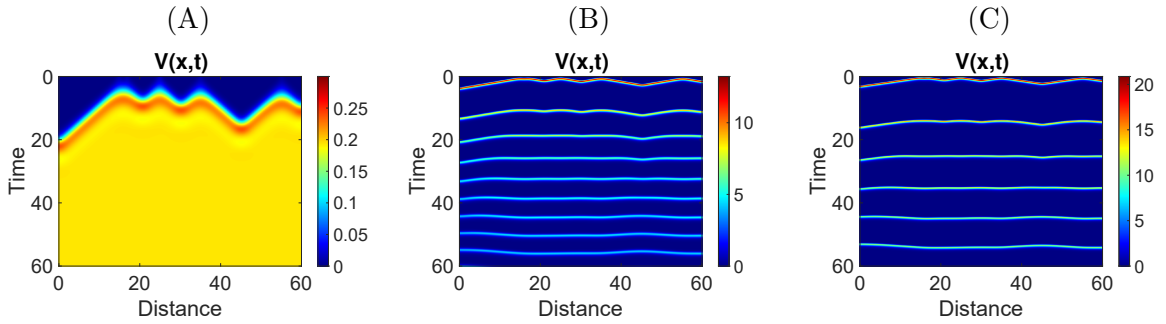

Figure 3.8: 1-D simulations with virus particles injected in different regions of the tumor. **(A):** $\theta = 58.33$, **(B):** $\theta = 350$, and **(C):** $\theta = 500$.

outcomes.

We also plot the TCP as function of time in Figure 3.9. In (A) and (C) the virus is injected into the centre of the domain while in (B) and (D) it is injected in five random locations. In (A) and (B) we chose $\theta = 350$ and in (C) and (D) we have $\theta = 500$. In all cases we see the maximum TCP right after the first cycle. We also note that a distributed injection of virus particles (B) and (D) has a beneficial outcome for the expected tumor control. The plots of the TCP for $\theta = 58.33$ are not shown, as the values do not exceed 2×10^{-20}, which we consider to be 0.

We see a significant difference to the TCP values for the ODE and PDE models. For example for $\theta = 58.33$ the TCP in the ODE model was 0.45 while in the spatial model it is 0. Hence the spatial context of cancer and virus spread is very important.

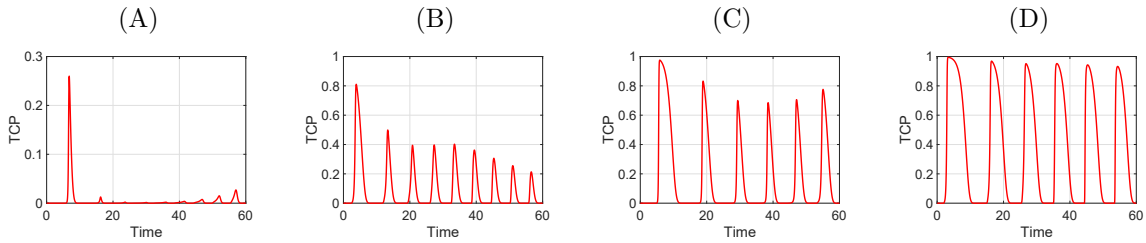

Figure 3.9: The TCP values of injected tumor cells when $\theta > \theta_H$ at $a = 3.33$ and $\gamma = 13.33$. **(A):** $\theta = 350$ where the tumor is injected in the center, **(B):** $\theta = 350$ where the tumor injected in five random locations, **(C):** $\theta = 500$ where the tumor is injected in the center, and **(D):** $\theta = 500$ where the tumor is injected five random locations.

3.4.5 PDE Model 2-D

In this section, we run the simulations of model (3.3) on a 2-D square domain of dimensions 60×60 up to time 37. In dimensional parameters this corresponds to a domain of side length 54 mm and a time of up to 123 days. First, in Figure 3.10 we choose $\theta_t < \theta < \theta_H$ with $\theta = 58.33$. Figures (A) and (D) show the cancer cell density with black for high concentration and brown for low. Figures (B) and (E) show the density of infected tumor cells, where high infection is white. Figures (C) and (F) show the distribution of the virus particles from blue (low) to red (high). Figures

(A),(B),(C) we show $t = 10$, and Figures (D),(E), (F) are at $t = 25$. The pattern is a filled ring pattern that spreads radially and establishes the coexistence steady state in the inside of the ring. In Figure 3.11, we observe the progression of the filled ring pattern within the virus at t=1, 5, 10, 15, 20, and 25, with the highest concentrated region appearing red at the center.

In Figure 3.12 we consider the oscillatory range and choose $\theta = 500 > \theta_H$. We first observe a hollow ring pattern, where tumor is destroyed by the spreading virus wave, leaving a close-to zero state in the inside of the ring. However, as the simulation continues, shown in Figure 3.13, the cancer and the virus come back. They regrow in the centre of the domain and initiate a second outward moving ring of viral infection. This repeats periodically, though, it is not an exact period, since the inoculation spot in the middle of the domain splits up into two spots as seen in Figure 3.13 ($t = 24$) and ($t = 34$). This process of periodic spot splitting is a new effect in reaction-diffusion equations and has, as far as we know, never been analysed before. Also, we get concentric rings resulting of the overlap of several hollow rings which has been remarked in Wodarz et al. [81], Kim et al. [98] and Morselli et al. [91] papers.

Similar behaviour has been induced when we use different injection strategies as we can see in Figure 3.14 and 3.15. The only difference in this case is that the complex interaction of the virus particles and their emergence lead to complex interactions of expanding hollow ring patterns. Again, we observe the periodic peak splitting mentioned above.

Finally, we were interested in the long-time dynamics, since it is known that coupled oscillators can lead to chaotic patterns [182]. The MATLAB code used above prevents a very long time analysis, hence we are using a new tool *VisualPDE* that was recently developed at Durham University [181]. This tool allows us to run very long time simulations and also to extend the domain to a circular shape of radius 250. We observe highly dynamic patterns that include oscillations, spiral waves, target patterns, etc. In Figure 3.16 we show a still image of a typical simulation for

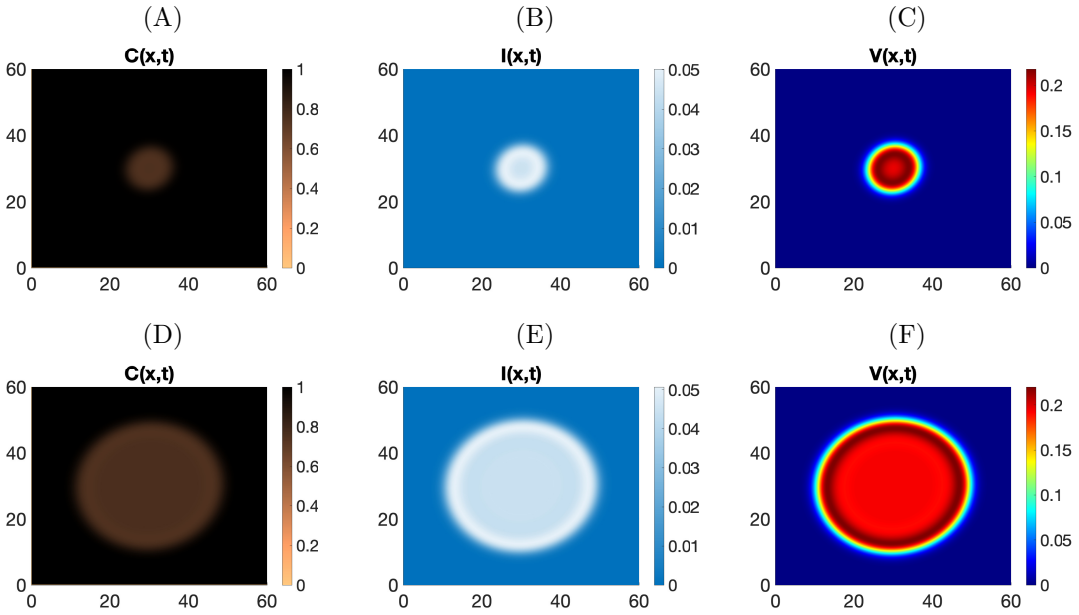

Figure 3.10: 2-D simulations with virus particles injected in the center of the tumor, the spatial distribution of the susceptible cells, infected cells and the virus with $\theta = 58.33$, $a = 3.33$ and $\gamma = 13.33$ at $t = 10$ and $t = 25$, respectively. **(A):** C(x,t), **(B):** I(x,t), and **(C):** V(x,t). **(D):** C(x,t), **(E):** I(x,t), and **(F):** V(x,t).

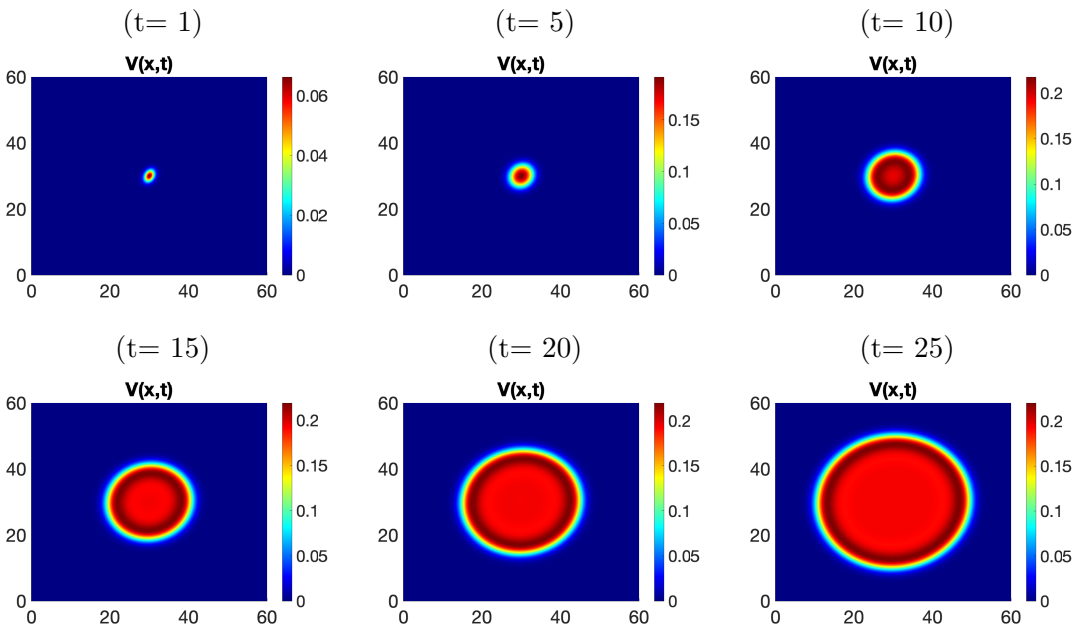

Figure 3.11: 2-D simulations with the virus particles injected in the center of the tumor, the spatial distribution of the virus particles with $\theta = 58.33$, $a = 3.33$ and $\gamma = 13.33$ at different t.

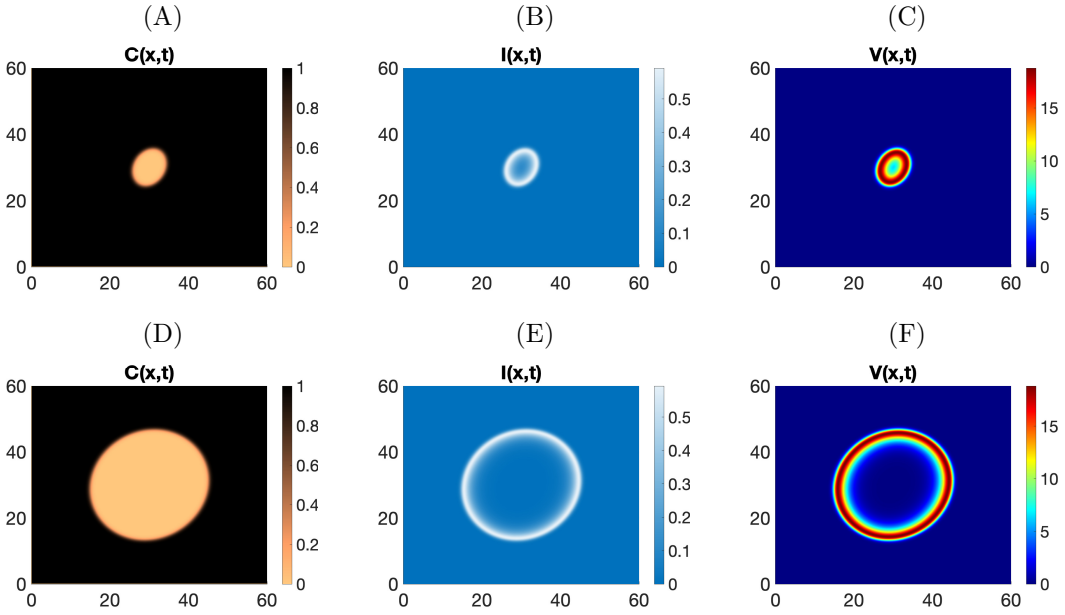

Figure 3.12: 2-D simulations with virus particles injected in the center of the tumor, the spatial distribution of the susceptible cells, infected cells and the virus with $\theta = 500$, $a = 3.33$ and $\gamma = 13.33$ at $t = 1$ and $t = 3$, respectively. **(A):** C(x,t), **(B):** I(x,t), and **(C):** V(x,t). **(D):** C(x,t), **(E):** I(x,t), and **(F):** V(x,t).

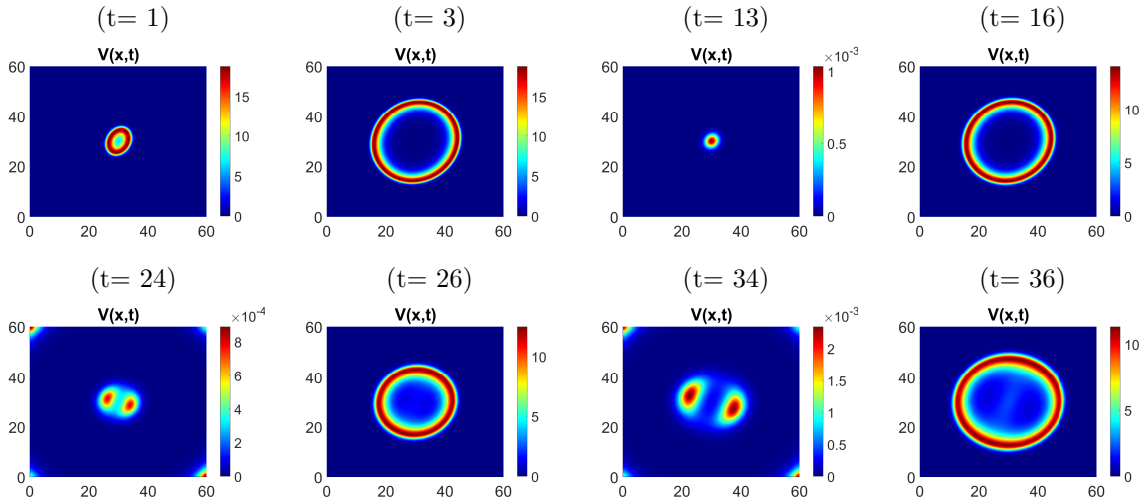

Figure 3.13: Simulation of model (3.3) for initial conditions where the virus particles injected in the center of the tumor with $\theta = 500$, $a = 3.33$ and $\gamma = 13.33$.

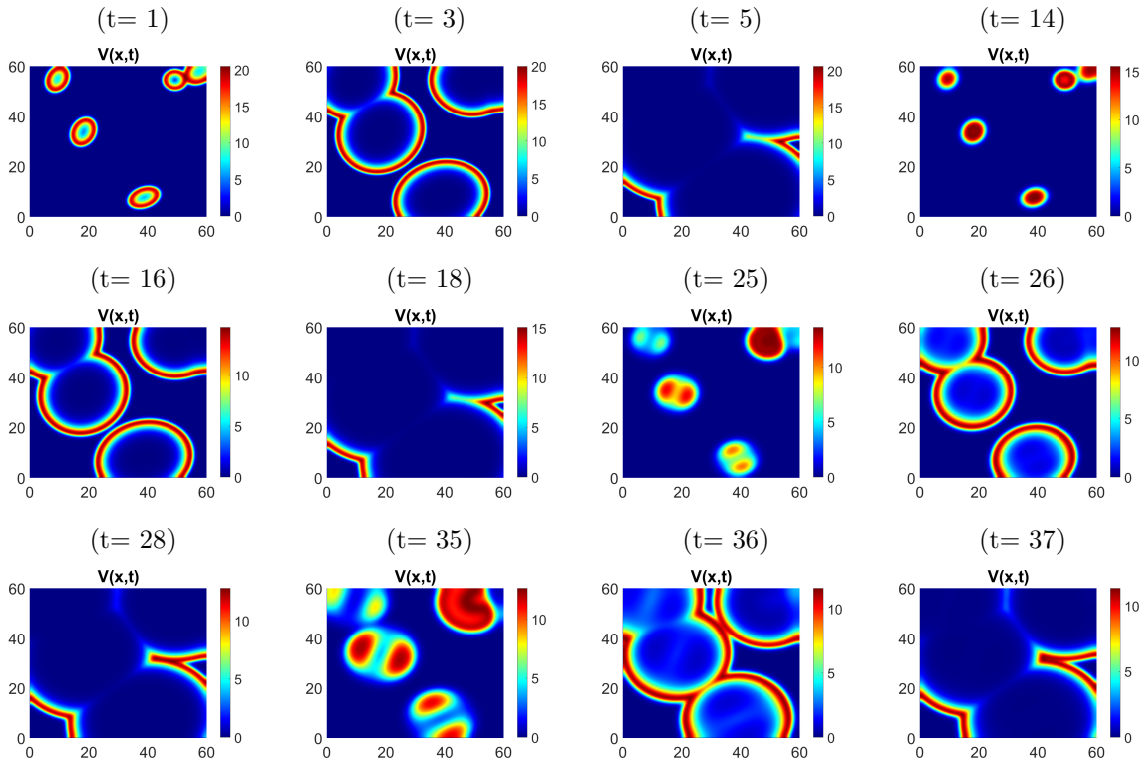

Figure 3.14: Simulation of model (3.3) for initial conditions where the virus particles injected in five locations randomly, with $\theta = 500$, $a = 3.33$ and $\gamma = 13.33$.

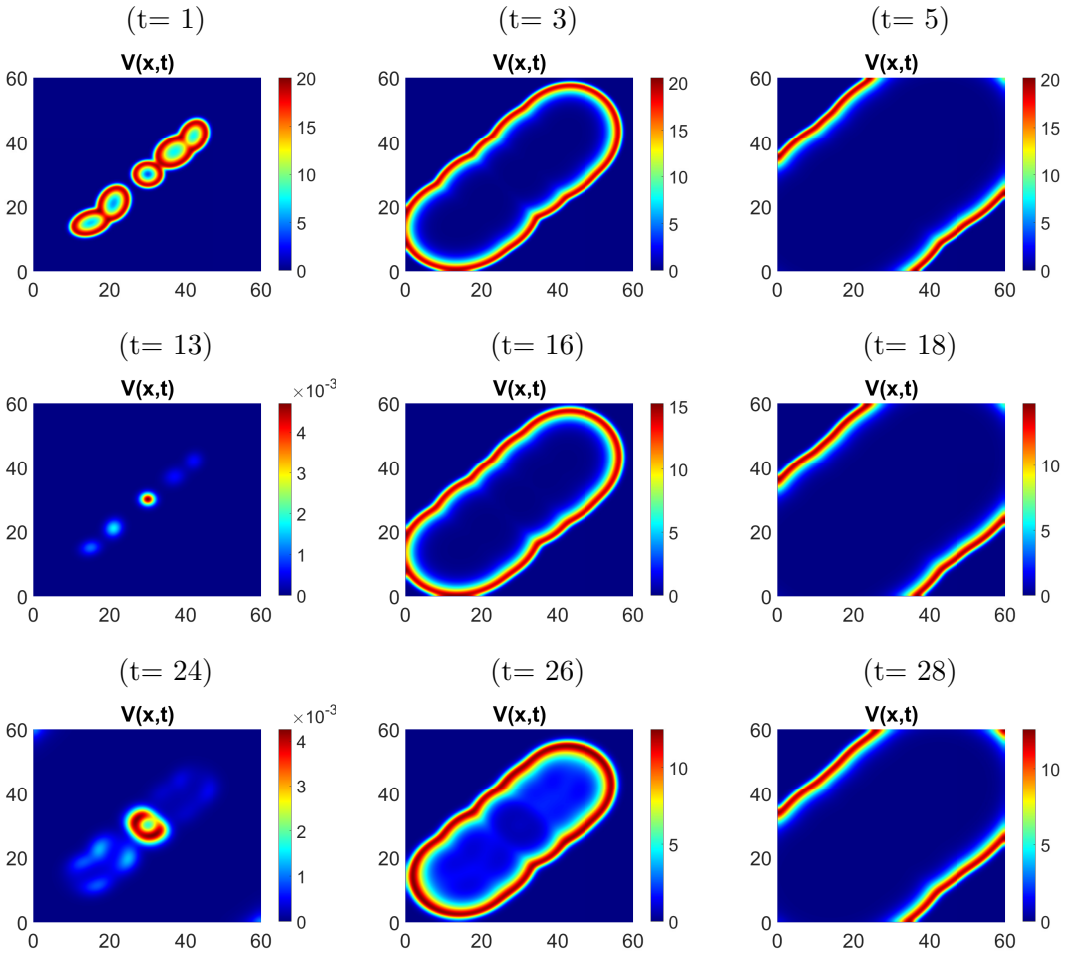

Figure 3.15: Simulation of model (3.3) for initial conditions where the virus particles injected the tumor as diagonal with $\theta = 500$, $a = 3.33$ and $\gamma = 13.33$.

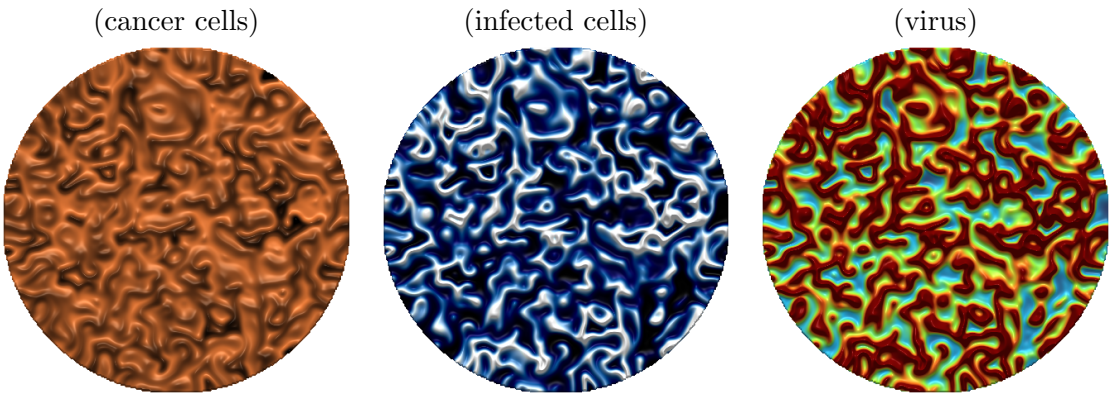

Figure 3.16: Simulations with *VisualPDE* [181] at time $t = 635$ (2116 days) with parameters from Table 3.2 and $\theta = 500$. The cancer cells on the left are shown from 0 (brown) to 0.2 (black). The scale for the infected cells is 0 (blue) to 0.05 (white), and the scale for the virus is 0 (blue) and 1 (red). A video of the dynamics between $t = 600$ and $t = 700$ is available on youtube: https://youtube.com/shorts/V6drXLbs3k0.

the parameter values above with $\theta = 500$. These spatio-temporal patterns persist for as long as we run the simulation. A short video of these dynamics is available on youtube: https://youtube.com/shorts/V6drXLbs3k0.

3.5 Conclusion

The mathematical modelling of oncolytic viruses through a susceptible-infected-virus model is a standard approach (see references in the introduction of this thesis). The occurance of oscillations is well established and it relates to the predator-prey relationship of the cancer cells and the virus. Two aspects, which were less studied in the literature, are considered here: the relevance of these oscillations in clinical practice and the rich patterns that can arise in the spatial context.

From the medical point of view it is clear that the adaptive immune response is activated within a few days [183]. Hence our simulations beyond a few days are unrealistic for patient outcomes. This includes the prolonged oscillations, which typically had a wave length of 10 days or so. Rather, it appears that the tumor burden goes very close to 0 between these oscillatory outbreaks, indicating tumor removal. We

computed the tumor control probability (TCP) to express this fact. We find that with increased viral production rate θ, tumor control can be achieved within a few days. However, for realistic values of $\theta = 58.33$ we found a TCP of 0 in our spatial model, which confirms the observation that oncolytic viral therapy alone is insufficient in many cases [58, 59, 66, 97]. Mechanisms to increase θ seem to be a promising strategy to improve the outcome of oncolytic virotherapy. We recall that

$$\theta = \frac{\alpha\,\beta\,b\,L}{\tau^2} \quad \text{and} \quad a = \frac{\alpha}{\tau},$$

where α denotes the removal rate of infected cells, β denotes the infection rate, b is the burst size of new virions, L denotes the carrying capacity of cancer cells and τ denotes the cancer growth rate.

An immediate option to increase the efficiency of oncolytic virotherapy is to increase the viral infectivity β and the viral burst size b. This confirms previous observations by [66, 68, 97] and it is indeed focus of several virology labs to increase the efficiency of a viral infection [52, 53].

The cancer growth dynamics are represented in θ as the ratio L/τ^2. I.e. if the effective growth rate τ is large, then θ is small and cancer gains an advantage. This opens the door to combine oncolytic virotherapy with growth reduction treatments such as chemotherapy. Chemotherapy can reduce τ, thereby moving θ into the Hopf region to gain tumor control. Combinations of oncolytic virotherapy and chemotherapy were studied in [184–186].

The clearance rate of infected cells α enters our model parameters in two important ways. On the one hand increasing α also increases θ. But in addition, increasing α increases our bifurcation values for the transcritical bifurcation θ_t and for the Hopf bifurcation θ_H. For the value of θ_t this is obvious from (3.6). For the Hopf value θ_H we need to look back at the condition $\kappa(\theta) = 0$ with $\kappa(\theta)$ from (3.9). The coefficient m is increasing in a, hence all positive terms in $\kappa(\theta)$ are increasing in a. The only negative term is $-\theta^3$. This implies that the positive zero θ_H is also increasing in a. As a result,

increasing the infected removal rate shifts the system closer to treatment failure. One way how α or a are increased is the action of the adaptive immune response. If the adaptive immune response activates within a few days, a is increased and the dynamic shifts to reduced viral infection and increased cancer growth. This confirms the common understanding that the oncolytic virus has to be fast to accomplish maximal effect before the immune system responds. We did not explicitly model the immune response here, but the effect is clear. Oncolytic virotherapy with inclusion of immune responses was modelled in [62, 68, 104] and others.

Overall we observe a conundrum. The first idea is to control cancer with a virus that is deadly for cancer alone. However, in many cases the virus is not quick enough to spread through the entire tumor before the adaptive immune system activates. One strategy to overcome this are multiple virus injections at different sites, as we have shown in our simulations. The second idea is to not expect the oncolytic virus to kill, but rather mark cancer cells with an antigen that is recognized by immune cells. However, immune cell kill might be too quick to allow the viral infection to spread to the entire tumor. A Goldilocks regime needs to be found, where viral infection and immune cell kill balance in the right way. This conclusion is further confirmed by models that include immune response. Storey et al. [68] talk about an intermediate immune response for optimal treatment outcome, and Eftimie et al. [62, 103] show the existence of multi-stability and even multi-instability, which is a strong indication of irregular and chaotic behavior.

In the spatial context we computed the speed of invasion of the virus front. This important information tells us if the virus infection is quick enough to reach the entire tumor, before the adaptive immune system kicks in. In Figure 3.7 (A), for example, with a single injection in the centre of the tumor, it took about 38 time units (129 days) before the entire domain was infected. A distributed injection in Figure 3.8 (A) only needed 21 time units (70 days).

In addition, we can do what mathematicians have done ever since modelling existed:

forget the biology for the moment, and consider the model as a mathematical object of its own interest. We find that the model reproduces typical viral load patterns such as a coexistence steady state in Figure 3.10 and a spreading hollow-ring pattern in Figure 3.12. Moreover, we find a new phenomenon of oscillatory peak splitting (see Figures 3.13 and 3.14) which we cannot explain with our current methods. Long time simulations (see Figure 3.16) revealed very complex spatio-temporal oscillations, and the analysis of those is currently out of reach.

While these patterns might not be relevant in the context of oncolytic viruses, they can be relevant for other virus infections. For example many COVID-19 patients suffer from long lasting recurring effects [187, 188], and we can speculate that continued oscillations might have such an effect. The variability of virus infections is enormous [189], and even our abstract mathematical results might develop into useful tools in the future.

Chapter 4

Spatial Oscillations with Michaelis-Menten Kinetics

In this chapter, we further investigate the spatial oscillations within cancer cells, this time incorporating Michaelis-Menten reaction kinetics. We opt for the Michaelis-Menten interaction due to its enhanced realism and its demonstrated capability to align with experimental findings compared to the mass-action case [190]. However, owing to the analytical complexity associated with Michaelis-Menten kinetics, mass-action kinetics remain widely employed.

Given the analogous nature of the analysis involving Michaelis-Menten kinetics to that of mass-action kinetics, we bypass certain basic analyses and proceed directly to presenting the results. Thus, similar to Chapter 3, we begin by analyzing the modified Pooladvand et al.'s [88] adenovirus infection model in glioblastoma where we consider the virus-cancer cell interaction in Michaelis-Menten form. We investigate the propagation of the viral invasion wave and explicitly determine the minimum speed of the viral wave. Additionally, we examine how considering the Michaelis-Menten form impacts the spatio-temporal virus infection patterns.

Similar to the results obtained with mass-action kinetics, our numerical simulations in 2-D reveal various spatial interactions of the virus infection, such as the hollow-ring pattern, filled target pattern, and concentric rings. However, unlike the mass-action results, we observe the loss of the phenomenon of periodic peak splitting.

Furthermore, we compute the tumor control probability (TCP) for the regions where the number of cancer cells approaches zero during the spatial oscillations.

Chapter 4 is structured as follows: In Section 4.1, we introduce the modified Pooladvand's reaction-diffusion model and apply a non-dimensionalization method to simplify parameters. In Section 4.2, we investigate the ODE-version of our model, determine the steady states, their stability, and pinpointing the two relevant bifurcations: a transcritical bifurcation and a Hopf bifurcation. Subsequently, we establish the minimal invasion speed for the one-dimensional PDE version of the model. Section 4.3 is dedicated to the numerical investigation, encompassing both 1D and 2D simulations. Finally, in Section 4.4, we conclude this chapter.

4.1 The Basic Assumptions and the Mathematical Model

Considering reaction diffusion model on a rectangular or smooth domain $\Omega \subset \mathbb{R}^n$:

$$\begin{aligned} \frac{\partial C}{\partial t} &= D_C \Delta C + \tau C \left(1 - \frac{C+I}{L}\right) - \frac{\hat{\beta} C V}{h_c + C}, \\ \frac{\partial I}{\partial t} &= D_I \Delta I + \frac{\hat{\beta} C V}{h_c + C} - \alpha I, \\ \frac{\partial V}{\partial t} &= D_V \Delta V + \alpha b I - \omega V, \end{aligned} \tag{4.1}$$

where the density of susceptible tumor cells, infected tumor cells, and free viruses is denoted by $C(x,t)$, $I(x,t)$, and $V(x,t)$, respectively. The tumor growth rate is τ and L is the carrying capacity of tumor cells. The Michaelis–Menten term $\frac{\hat{\beta} C V}{h_c + C}$ describes the interaction between virus particles and the tumor cells. The infection rate is denoted by $\hat{\beta}$ and h_c is the Michaelis–Menten constant. The death rate of infected cells is denoted by α. The burst size of the virus in infected cells is denoted by b, and ω is viral clearance rate. The diffusion coefficients of susceptible cells, infected cells, and viruses are denoted by D_C, D_I, D_V, respectively. The symbol Δ denotes the Laplacian, i.e. the sum of all second order derivatives.

$$C(x,0) = C_0(x) > 0, \quad I(x,0) = 0, \quad V(x,0) = V_0(x) > 0, \tag{4.2}$$

and homogenous Nuemann boundary conditions on $\partial\Omega$:

$$n \cdot \nabla C(x,t) = n \cdot \nabla I(x,t) = n \cdot \nabla V(x,t) = 0, \qquad \text{for all} \quad x \in \partial\Omega,$$

where n denotes an outward normal at x at $\partial\Omega$. In the case of a rectangular domain some points will have several outer normal vectors. In that case we require the above boundary conditions for all normal vectors.

To simplify our analysis, we apply the non-dimensionalization method by considering

$$\hat{C} = \frac{C}{L}, \quad \hat{I} = \frac{I}{L}, \quad \hat{V} = \frac{\hat{\beta}}{\tau h_c} V, \quad \hat{t} = \tau t, \text{ and } \hat{x} = x\sqrt{\frac{\tau}{D_V}}.$$

After dropping the hat, we get the non-dimensional system:

$$\begin{aligned} \frac{\partial C}{\partial t} &= D_c \frac{\partial^2 C}{\partial x^2} + C\,(1 - C - I) - \frac{jCV}{j + C}, \\ \frac{\partial I}{\partial t} &= D_i \frac{\partial^2 I}{\partial x^2} + \frac{jCV}{j + C} - aI, \\ \frac{\partial V}{\partial t} &= \frac{\partial^2 V}{\partial x^2} + \theta I - \gamma V, \end{aligned} \tag{4.3}$$

where

$$D_c = \frac{D_C}{D_V}, \quad D_i = \frac{D_I}{D_V}, \quad j = \frac{h_c}{L}, \quad a = \frac{\alpha}{\tau}, \quad \theta = \frac{\alpha \hat{\beta} L b}{h_c \tau^2}, \text{ and } \gamma = \frac{\omega}{\tau}. \tag{4.4}$$

4.2 Analysis of the Model

4.2.1 Analysis of the Kinetic Part

The ODE system of (4.3) has three steady states which are the trivial steady state $E_0 = (0,0,0)$, the pure cancer state $E_1 = (1,0,0)$ and a coexistence steady state

$$E_+ = (C^*, I^*, V^*) = \left(\frac{a\gamma j}{j\theta - a\gamma}, \quad \frac{C^*(1 - C^*)}{C^* + a}, \quad \frac{\theta}{\gamma} I^* \right),$$

which exists in the positive quadrant for $0 < C^* < 1$. If θ is increased, the coexistence steady state arises through a transcritical bifurcation at

$$\theta_t = \frac{j+1}{j}\, a\gamma. \tag{4.5}$$

The transcritical bifurcation (4.5) in Michaelis-Menten is just a shift of the transcritical bifurcation $\theta_t = a\gamma$ in the mass-action case by $\frac{j+1}{j}$. Similar to the mass-action model, the effective viral production rate θ will be our bifurcation parameter in the next sections. We compute the basic reproduction number R_0 by next generation matrix with

$$F = \begin{bmatrix} 0 & \frac{j}{j+1} \\ \theta & 0 \end{bmatrix}, V = \begin{bmatrix} a & 0 \\ 0 & \gamma \end{bmatrix}$$

Thus $R_0 = \frac{j\theta}{a\gamma(j+1)}$ is the spectral radius of FV^{-1}. Since, the coexistence steady state E_+ exists in positive quadrant iff $\theta > \frac{a\gamma(j+1)}{j}$, this equivalent to $R_0 > 1$.

The Jacobian matrix of the ODE system (4.3) is

$$J = \begin{bmatrix} 1 - 2C - I - \frac{j^2 V}{(j+C)^2} & -C & -\frac{jC}{j+C} \\ \frac{j^2 V}{(j+C)^2} & -a & \frac{jC}{j+C} \\ 0 & \theta & -\gamma \end{bmatrix} \tag{4.6}$$

1. The Jacobian matrix of $E_0 = (0, 0, 0)$ is

$$J(E_0) = \begin{bmatrix} 1 & 0 & 0 \\ 0 & -a & 0 \\ 0 & \theta & -\gamma \end{bmatrix}$$

   Therefore, the eigenvalues are $\lambda_1 = 1 > 0$, $\lambda_2 = -a < 0$, and $\lambda_3 = -\gamma < 0$. Thus, $E_0 = (0, 0, 0)$ is unstable saddle.

2. The Jacobian matrix of $E_1 = (1, 0, 0)$ is

$$J(E_1) = \begin{bmatrix} -1 & -1 & -\frac{j}{j+1} \\ 0 & -a & \frac{j}{j+1} \\ 0 & \theta & -\gamma \end{bmatrix}$$

If we multiply the second row of the matrix $J(E_1)$ by $\frac{\theta}{a}$ and add it to the third row, we get

$$J(E_1) = \begin{bmatrix} -1 & -1 & -\frac{j}{j+1} \\ 0 & -a & \frac{j}{j+1} \\ 0 & 0 & \frac{j\theta}{a(j+1)} - \gamma \end{bmatrix}$$

Therefore, the eigenvalues are $\lambda_1 = -1 < 0$, $\lambda_2 = -a < 0$, and $\lambda_3 = \frac{j\theta}{a(j+1)} - \gamma = \frac{j\gamma\theta}{a\gamma(j+1)} - \gamma = \gamma(R_0 - 1)$. Thus, $E_1 = (1, 0, 0)$ is stable if $R_0 < 1$, and unstable if $R_0 > 1$.

Proposition 4.2.1 *The stability of steady state $E_1 = (1, 0, 0)$ is determined by R_0.*

(a) If $R_0 < 1$, then E_1 is locally stable.

(b) If $R_0 > 1$, then E_1 is a saddle.

3. The Jacobian matrix of $E_+ = (C^*, I^*, V^*)$ is

$$J(E_+) = \begin{bmatrix} 1 - 2C^* - \frac{C^*(1-C^*)}{C^*+a} - \frac{j^2\theta C^*(1-C^*)}{\gamma(j+C^*)^2(C^*+a)} & -C^* & -\frac{jC^*}{j+C^*} \\ \frac{j^2\theta C^*(1-C^*)}{\gamma(j+C^*)^2(C^*+a)} & -a & \frac{jC^*}{j+C^*} \\ 0 & \theta & -\gamma \end{bmatrix} = \begin{bmatrix} b_{11} & -b_{12} & -b_{13} \\ b_{21} & -a & b_{13} \\ 0 & \theta & -\gamma \end{bmatrix}$$

where

$$\begin{aligned} b_{11} &= 1 - 2C^* - \frac{C^*(1-C^*)}{C^*+a} - \frac{j^2\theta C^*(1-C^*)}{\gamma(j+C^*)^2(C^*+a)}, \\ b_{12} &= C^*, \\ b_{13} &= \frac{jC^*}{j+C^*}, \\ b_{21} &= \frac{j^2\theta C^*(1-C^*)}{\gamma(j+C^*)^2(C^*+a)}. \end{aligned}$$

Thus, the characteristic equation of $E_+ = (C^*, I^*, V^*)$ is given by $\lambda^3 + P_2\lambda^2 + P_1\lambda +$

$P_0 = 0$, where

$$P_2 = a + \gamma - b_{11},$$
$$P_1 = a\gamma + b_{12}b_{21} - (a+\gamma)b_{11} - \theta b_{13},$$
$$P_0 = \theta b_{11}b_{13} + \gamma b_{12}b_{21} + \theta b_{13}b_{21} - a\gamma b_{11}.$$

The Hopf bifurcation function is given by

$$H(\theta) = a\gamma(a+\gamma) - b_{13}\theta(a+\gamma+b_{21}) + ab_{12}b_{21} + b_{11}\left[(a+\gamma)b_{11} - b_{12}b_{21} - (a+\gamma)^2\right].$$

In contrast to the mass-action case, proving the stability of the coexistence steady state $E_+ = (C^*, I^*, V^*)$ and the existence of Hopf bifurcation analytically is challenging due to the system's complexity. Thus, we will demonstrate it numerically in Section 4.3.

4.2.2 Wave Fronts of Glioma and Virus

In Chapter 3, the wave speed of glioma in the absence of viral infection was determined to be $c_c^* = 0.3162$. The wave speed of the virus, denoted as c^*, can be calculated using the leading edge method. While the calculation procedure resembles that of the mass-action case, we omit the details and introduce the characteristic equation:

$$\left(D_c\lambda^2 - c\lambda - 1\right)\left[D_i\lambda^4 - c(D_i+1)\lambda^3 + (c^2 - D_i\gamma - a)\lambda^2 + c(\gamma+a)\lambda + a\gamma - \frac{j\theta}{j+1}\right] = 0. \tag{4.7}$$

Since the first factor of (4.7) corresponds to unsuitable orbits in phase space, our focus lies on the second factor:

$$\Phi(\lambda; c) = D_i\lambda^4 - c(D_i+1)\lambda^3 + (c^2 - D_i\gamma - a)\lambda^2 + c(\gamma+a)\lambda + a\gamma - \frac{j\theta}{j+1}. \tag{4.8}$$

Equation (4.8) closely resembles the characteristic equation (3.17) in the mass-action case, differing only in the constant term $a\gamma - \frac{j\theta}{j+1}$. Thus, by applying implicit differentiation to $\Phi(\lambda; c) = 0$, we derive conditions for $c'(\lambda) = 0$ similar to those in the

mass-action case, given by $\Psi(\lambda; c) = 0$, where

$$\begin{aligned} \Psi(\lambda; c) &= 2\lambda c^2 + \eta_1 c + \eta_0, \\ \eta_1 &= \gamma + a - 3(D_i + 1)\lambda^2, \\ \eta_0 &= 4D_i\lambda^3 - 2(D_i\gamma + a)\lambda. \end{aligned}$$

Consequently, the minimum wave speed c^* occurs at the intersection of the two manifolds:

$$\{\Phi(\lambda; c) = 0\} \quad \text{and} \quad \{\Psi(\lambda; c) = 0\}.$$

For the parameter values from Table 4.1, we depict these curves in a (λ, c)-diagram in Figure 4.1. In this representation, we identify a unique intersection at:

$$\lambda^* \approx 0.8276 \qquad \text{and} \qquad c^* \approx 0.3952, \tag{4.9}$$

as illustrated in Figure 4.1. Notably, in the case of Michaelis-Menten interaction, the viral wave speed is slower than that of mass-action, which were

$$\lambda^*_{\text{mass-action}} \approx 1.5728 \qquad \text{and} \qquad c^*_{\text{mass-action}} \approx 0.9299,$$

see (3.19).

4.3 Numerical Analysis

Numerically solving for the roots of Hopf bifurcation function $H(\theta)$ yields

$$\theta_H = -2134.92, 35.90, 426.52, 438.25, 442.31, \text{and } 548.61.$$

However, $\theta = -2134.92$ is biologically irrelevant since $\theta > 0$. Additionally, $\theta = 35.90, 426.52, 438.25$, and 442.31 are disregarded since within these ranges, the coexistence steady state does not exist, leading to the failure of virotherapy treatment. Considering the values presented in Table 4.1 and Table 4.2, the coexistence steady state is established for $\theta > \theta_t = 488.95$. Consequently, we select values of θ satisfying

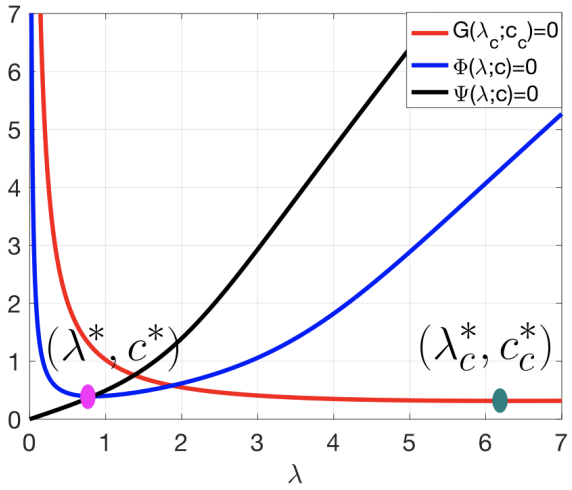

Figure 4.1: The characteristic equation of the tumor and virus as implicit function with respect to λ and c. The green circle is the minimum decay rate and corresponding minimum wave speed of tumor cells. The pink circle is the minimum decay rate and corresponding minimum wave speed of the virus particles. The parameters values are in Table 4.1.

$\theta > 488.95$. Moreover, a numerical investigation reveals a Hopf bifurcation occurring at $\theta_H = 548.61$ with $\frac{dH}{d\theta}\,|_{\theta=548.62} = -1.31 \neq 0$.

This chapter focuses particularly on the Hopf bifurcation region, which corresponds to the hollow ring pattern. Furthermore, as demonstrated in Chapter 3, the optimal TCP resides within the Hopf region.

The only parameters requiring estimation are the infection rate $\hat{\beta}$ and the Michaelis-Menten constant h_c, with all other parameter values remaining consistent with those employed in Chapter 3. For the parameter h_c, we consider the same value as used in previous studies [191, 192], which is $h_c = 10^5$ cells per mm^3.

To estimate the infection rate parameter $\hat{\beta}$, we establish the relationship between the infection rates in the mass-action case, denoted by β, and the Michaelis-Menten case, denoted by $\hat{\beta}$. Applying a Taylor expansion on the infection term $\frac{\hat{\beta}C}{h_c+C}$ about $C = L$, we obtain:

$$\frac{\hat{\beta}C}{h_c + C} = \frac{\hat{\beta}L}{h_c + L} + \frac{\hat{\beta}h_c}{(h_c + L)^2}(C - L) + \mathcal{O}((C - L)^2).$$

We consider only the leading term since the term $\frac{\hat{\beta}h_c}{(h_c+L)^2}(C - L)$ is very small.

Thus, we can approximate the infection rate of the Michaelis-Menten model from the infection rate of the mass-action model as follows:

$$\beta L \approx \frac{\hat{\beta} L}{h_c + L}.$$

Therefore, $\hat{\beta}$ can be calculated using the formula:

$$\hat{\beta} \approx (h_c + L)\beta. \tag{4.10}$$

According to Pooladvand et al. [88], the infection rate β lies within the range $[10^{-9}, 5 \times 10^{-9}]$. Therefore, using (4.10), we can estimate $\hat{\beta}$ to be within the range $[1.1 \times 10^{-3}, 5.5 \times 10^{-3}]$. Additionally, the burst size b is reported to be within the range $[1000, 100000]$. Thus, by fixing the parameters τ, L, h_c, and α, and varying $\hat{\beta}$ and b, we can calculate $\theta = \frac{\alpha \hat{\beta} L b}{h_c \tau^2}$ to be within the range $\theta \in [122.22, 61110.5]$.

After rescaling (4.4), the parameter values for model (4.3) are given in Table 4.2.

Parameter	**Value**	**Units**	**Description**
$C_0(x)$	10^6	cells per mm^3	Initial density of uninfected cells
$V_0(x)$	1.9×10^{10}	viruses per mm^3	Initial density of virus particles
D_C	0.006	mm^2 per day	Diffusion coefficient of susceptible cells
D_I	0.006	mm^2 per day	Diffusion coefficient of infected cells
D_V	0.24	mm^2 per day	Diffusion coefficient of viruses
τ	0.3	per day	Growth rate of tumor cells
L	10^6	cell per mm^3	Carrying capacity of tumor cells
$\hat{\beta}$	variable	cell per (virus $\times$ day)	Infection rate of Michaelis-Menten case
h_c	10^5	cell per mm^3	Michaelis-Menten constant
α	1	per day	Death rate of infected cells
b	variable	virus per cell	Burst size of viruses
ω	4	per day	Clearance rate of viruses

Table 4.1: Summary of CIV model parameters. All the parameters values used from reference [88] except that parameter h_c from reference [191, 192].

Rescaled Parameter	Meaning	Value
D_c	cancer diffusion coefficient	0.025
D_i	infected cells diffusion	0.025
j	$\frac{\text{Michaelis-Menten constant}}{\text{cancer cells carrying capacity}}$	0.1
a	infected death rate	3.33
γ	virus decay rate	13.33
θ	effective virus production rate	[0,900]

Table 4.2: Base parameter values of the rescaled model (4.3) using the rescaling (4.4). These parameters are unitless.

We start by analyzing the ODE system (4.3) with θ serving as a bifurcation parameter, derived from (4.4), where θ represents the effective virus production rate. Figure 4.3 depicts the dynamic behavior of model (4.3) using parameters from Table 4.2, while varying θ. The initial conditions for all four simulations are uniformly set to $(C(0), I(0), V(0)) = (1, 0, 95)$. In Figure 4.2 and Figure 4.3, we illustrate cases for $\theta = 520, 800, 900$ plotted against time. The transcritical bifurcation is evident at $\theta_t = 488.95$, resulting in a coexistence steady state for $\theta > \theta_t$. Subsequently, the Hopf bifurcation occurs at $\theta_H = 548.61$, leading to the emergence of periodic orbits beyond that threshold.

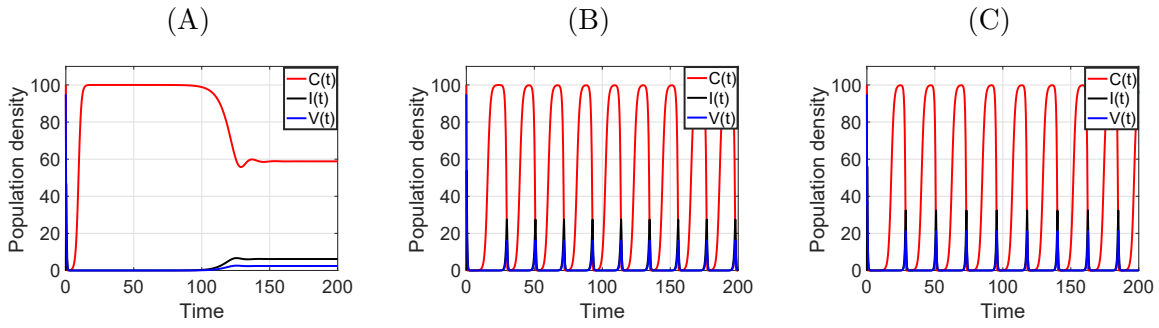

Figure 4.2: Numerical simulation with different θ values with initial conditions (1, 0, 95). Here, the susceptible and infected cells are re-scaled by multiplying with 100. **(A):** $\theta = 520$, **(B):** $\theta = 800$, and **(C):** $\theta = 900$.

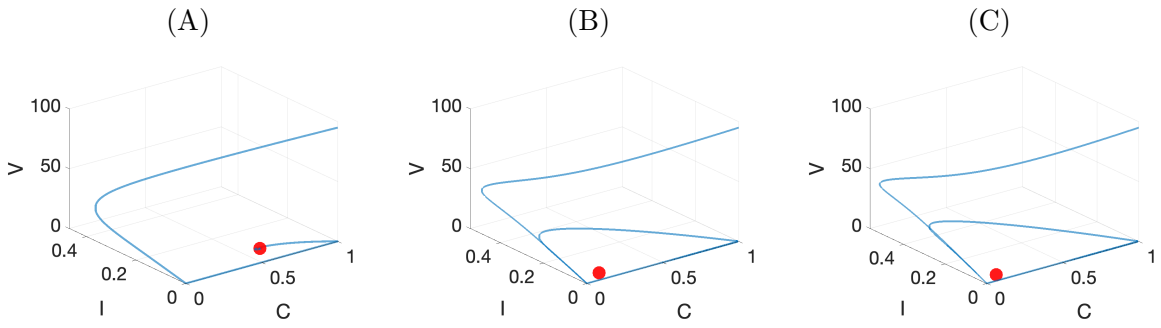

Figure 4.3: Numerical simulation of model (4.3) in 3-D with different θ values with initial conditions C=1, I=0, and V=95. The coexistence steady state is indicated in red. **(A):** $\theta = 520$, **(B):** $\theta = 800$, and **(C):** $\theta = 900$.

4.3.1 PDE Model 1-D

As we investigate the spatial manifestation of oscillations through mass-action interaction, we aim to explore whether incorporating the Michaelis-Menten case yields analogous patterns and enables us to attain a tumor control probability (TCP) nearing 1.

Similar to Chapter 3, we initiate our study in 1-D within the interval $[0, 60]$ and conduct simulations up to time 60. In dimensional parameters, this corresponds to a length interval of 54 mm and a duration of up to 200 days. Initially, virus particles are injected at the center of the domain, with zero-flux boundary conditions selected. The results of the simulations are depicted in Figure 4.4. Cancer cell density $C(x, t)$ is represented in shades of brown in panels (A) and (D), with darker hues indicating higher tumor cell density. Infected cells $I(x, t)$ are displayed in shades of blue in panels (B) and (E), with darker shades representing lower densities of infected cells. The virus load is illustrated in panels (C) and (F), ranging from blue (low) to red (high). In Figure (A), (B), and (C), we set $\theta = 520$ and $\theta = 900$ for Figure (D), (E), and (F).

We conduct identical simulations with a distinct initial condition showcased in Figure 4.5 (A), (B), (C). In this scenario, we randomly select five inoculation points within the interval $[0, 60]$. For $\theta = 520$ in (A), we observe an initial interaction

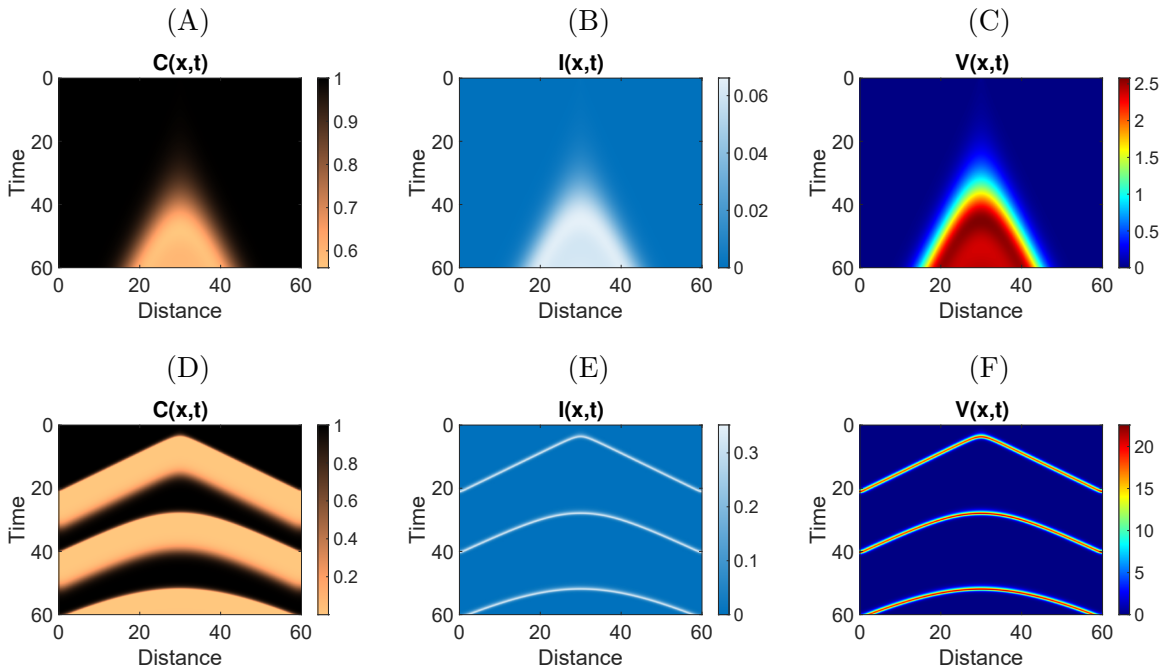

Figure 4.4: 1-D simulations with virus particles injected in the tumor center. The spatial distribution of the susceptible cells, infected cells and the virus with different values of θ with $a = 3.33$ and $\gamma = 13.33$. $\theta = 520$ for **(A)**, **(B)** and **(C)** and $\theta = 900$ for **(D)** **(E)** and **(F)**.

of spreading waves, swiftly converging to the coexistence steady state. In (B), with $\theta = 800$, and in (C), with $\theta = 900$, synchronized oscillations persist across the domain.

Since, the oscillations get close to zero, indicating low cancer and virus concentrations. Hence again, we employ the tumor control probability (3.22) to estimate the expected treatment success in the spatial context.

For the cases where we inject the oncolytic virus in the center of the domain we find that the maximal TCP value is 0 for $\theta = 520$, 0 for $\theta = 800$, and 0.0611 for $\theta = 900$. The TCP values were generally higher when the tumor was injected at five random locations with TCP of 0 for $\theta = 520$, 0.7149 for $\theta = 800$, and 0.6305 at $\theta = 900$. This clearly shows that for $\theta = 520$ treatment failure is expected.

We also plot the TCP as function of time in Figure 4.6. In (A) and (C) the virus is injected into the centre of the domain while in (B) and (D) it is injected in five random locations. In (A) and (B) we chose $\theta = 800$ and in (C) and (D) we have $\theta = 900$. In

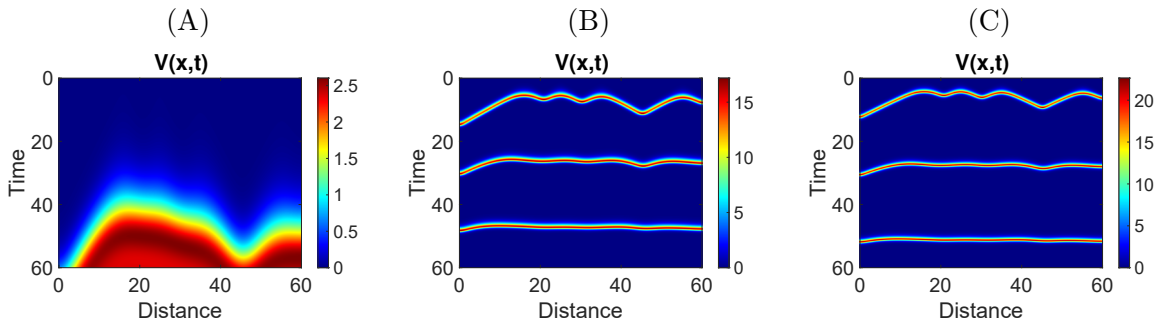

Figure 4.5: 1-D simulations with virus particles injected in different regions of the tumor. **(A):** $\theta = 520$, **(B):** $\theta = 800$, and **(C):** $\theta = 900$.

all cases we see the maximum TCP right after the first cycle. We also note that a distributed injection of virus particles (B) and (D) has a beneficial outcome for the expected tumor control. We refrain from displaying the TCP plots for $\theta = 520$, as the values do not surpass 7×10^{-17}, which we consider to be effectively zero.

Additionally, the TCP values for multiple injections were lower than those of the mass-action case, with the highest TCP in the Michaelis-Menten case reaching 0.7149 for $\theta = 800$, compared to 0.9944 for $\theta = 500$ in the mass-action formulation. Furthermore, contrary to the mass-action case, the TCP of the second cycle exceeds that of the first cycle. Consequently, extending the simulation duration up to $t = 150$, we observe that as the oscillations synchronize over time, the TCP value improves to over 0.97 (not shown). However, it's worth noting that these results are irrelevant from a medical standpoint, as this timeframe is too late, given that the immune response has already occurred.

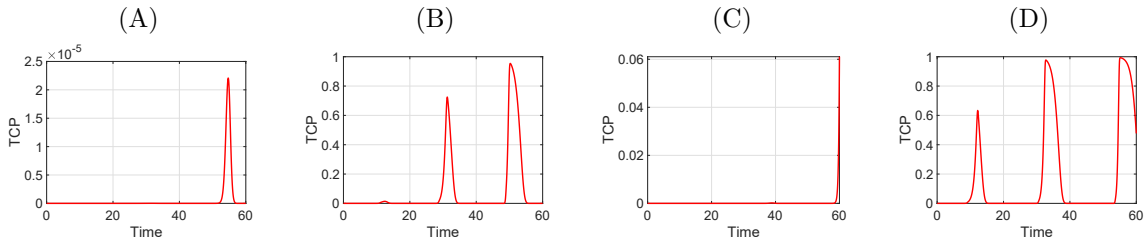

Figure 4.6: The TCP values of injected tumor cells when $\theta > \theta_H$ at $a = 3.33$ and $\gamma = 13.33$. **(A):** $\theta = 800$ where the tumor is injected in the center, **(B):** $\theta = 800$ where the tumor injected in five random locations, **(C):** $\theta = 900$ where the tumor is injected in the center, and **(D):** $\theta = 900$ where the tumor is injected five random locations.

4.3.2 PDE Model 2-D

In this section, we conduct simulations using model (4.3) on a 2-D square domain measuring 60×60 units, extended up to time 55. In terms of dimensional parameters, this equates to a domain with a side length of 54 mm and a time span of up to 183 days. Initially, in Figure 4.7, we set $\theta_t < \theta < \theta_H$ with $\theta = 520$. Panels (A) and (D) depict the density of cancer cells, represented by black for high concentration and brown for low. Panels (B) and (E) illustrate the density of infected tumor cells, where white indicates high infection. Panels (C) and (F) display the distribution of virus particles, ranging from blue (low concentration) to red (high concentration). In Panels (A), (B), and (C), we present the results at $t = 45$, while Panels (D), (E), and (F) showcase the outcomes at $t = 55$. The observed pattern resembles a filled ring that expands radially, establishing a coexistence steady state within the ring's interior. In Figure 4.8, we observe the progression of this filled ring pattern within the virus at time instances $t = 1$, 5, 10, 15, 20, and 25, with the highest concentration region appearing red at the center.

In Figure 4.9, we explore the oscillatory regime with $\theta = 900 > \theta_H$. Similar to the scenario in mass-action dynamics, we observe a distinctive hollow ring pattern, wherein the tumor succumbs to the advancing virus wave, resulting in a near-zero state within the ring's interior. However, as the simulation progresses, as depicted

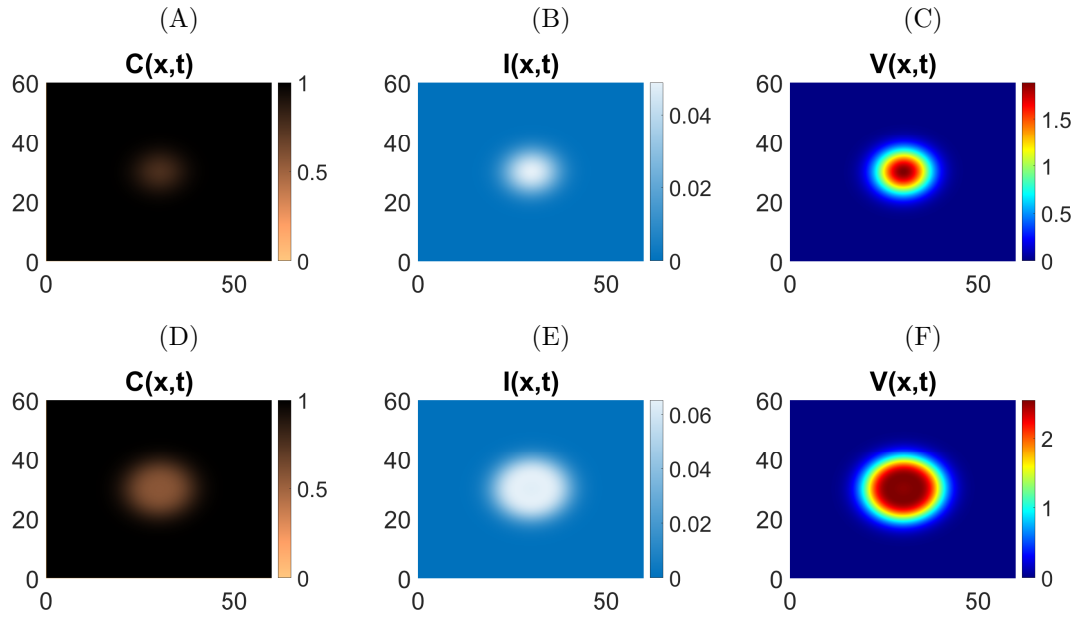

Figure 4.7: 2-D simulations with virus particles injected in the center of the tumor, the spatial distribution of the susceptible cells, infected cells and the virus with $\theta = 520$, $a = 3.33$ and $\gamma = 13.33$ at $t = 45$ and $t = 55$, respectively. **(A):** C(x,t), **(B):** I(x,t), and **(C):** V(x,t). **(D):** C(x,t), **(E):** I(x,t), and **(F):** V(x,t).

in Figure 4.10, both the cancerous cells and the virus stage a resurgence. They regenerate at the center of the domain, initiating a secondary outward wave of viral infection. This cycle repeats periodically, although we no longer observe the periodic spot splitting seen in the mass-action scenario. Additionally, concentric rings form due to the overlapping of multiple hollow rings.

We observe similar behavior when employing various injection strategies, as depicted in Figure 4.11 and 4.12. The notable distinction in this scenario is that the intricate interplay among virus particles and their emergence results in complex interactions, ultimately giving rise to expanding hollow ring patterns.

Finally, to explore the long-term dynamics, we utilize *VisualPDE* [181], enabling us to conduct simulations over extended periods and expand the domain to a circular shape with a radius of 250. We observe highly dynamic patterns, encompassing oscillations, spiral waves, target patterns, and more. In Figure 4.13, we present a static image from a typical simulation using the specified parameter values with

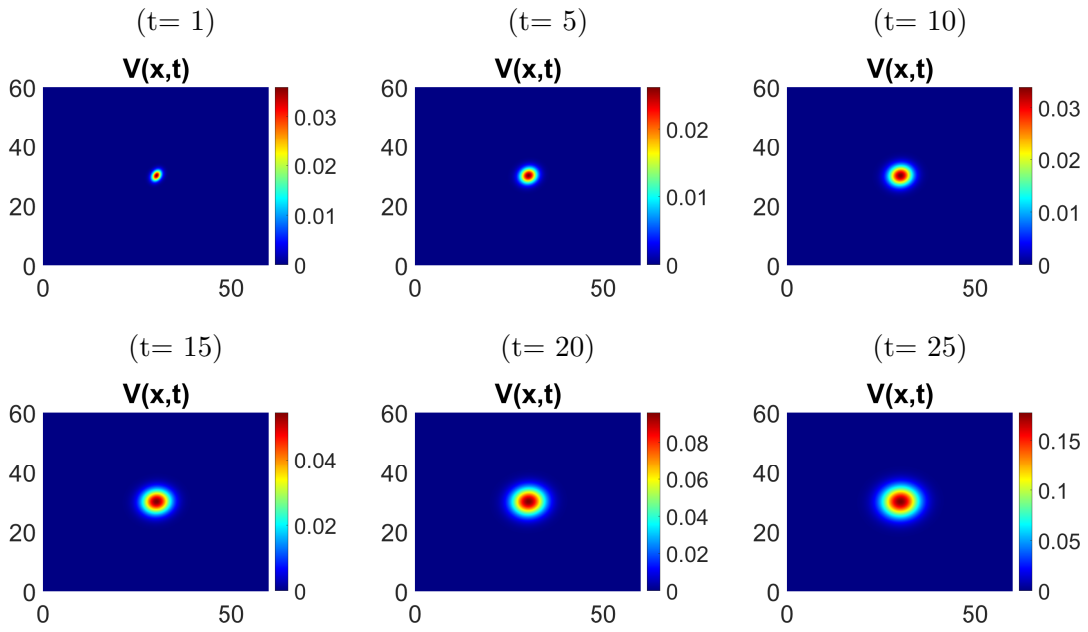

Figure 4.8: 2-D simulations with the virus particles injected in the center of the tumor with $\theta = 520$, $a = 3.33$ and $\gamma = 13.33$ at different t.

$\theta = 900$. These spatio-temporal patterns persist throughout the duration of the simulation.

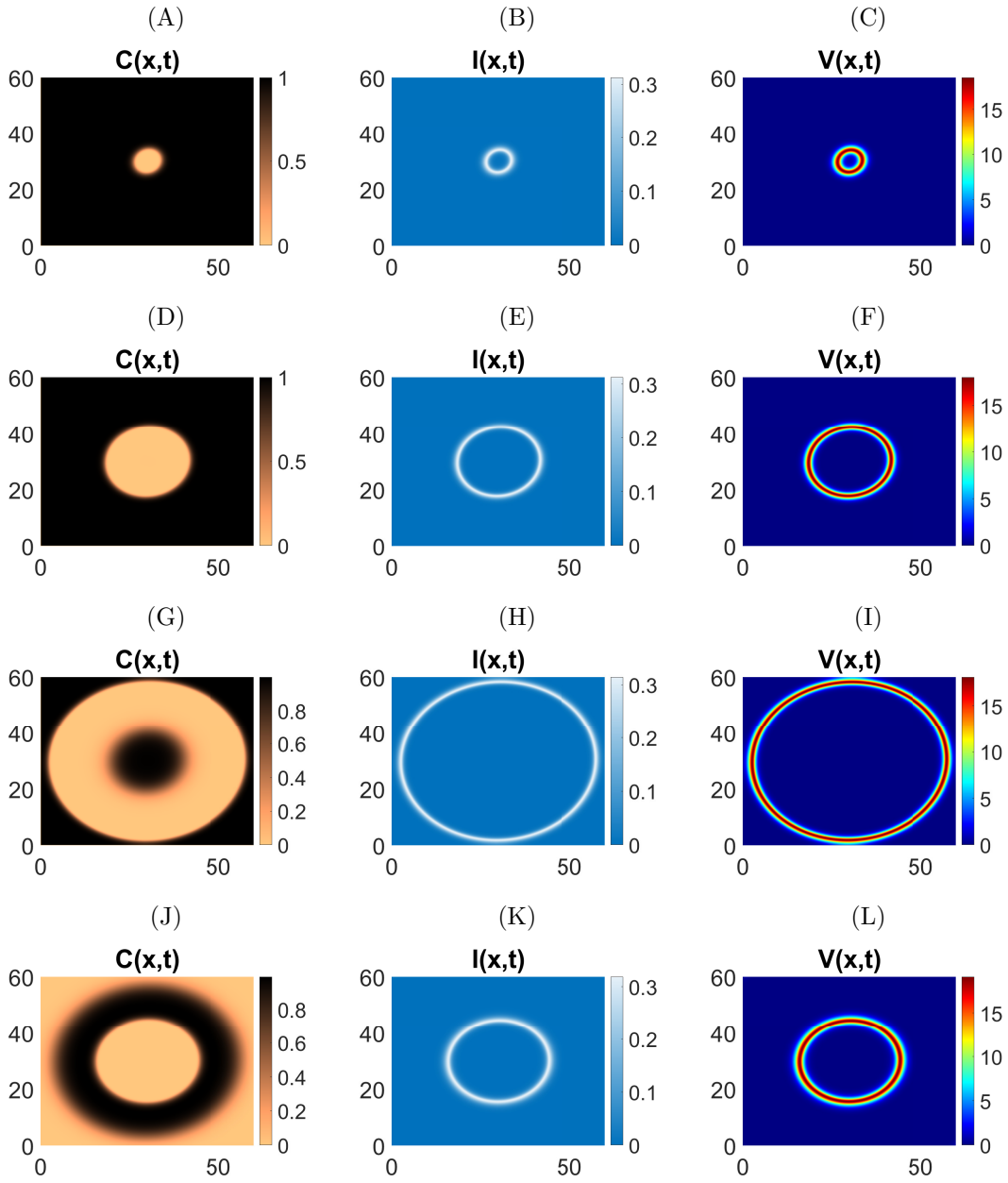

Figure 4.9: 2-D simulations with virus particles injected in the center of the tumor with $\theta = 900$, $a = 3.33$ and $\gamma = 13.33$ at $t = 5$, $t = 10$, $t = 20$, and $t = 30$, respectively. **(A):** C(x,t), **(B):** I(x,t), and **(C):** V(x,t). **(D):** C(x,t), **(E):** I(x,t), and **(F):** V(x,t). **(G):** C(x,t), **(H):** I(x,t), and **(I):** V(x,t). **(J):** C(x,t), **(K):** I(x,t), and **(L):** V(x,t).

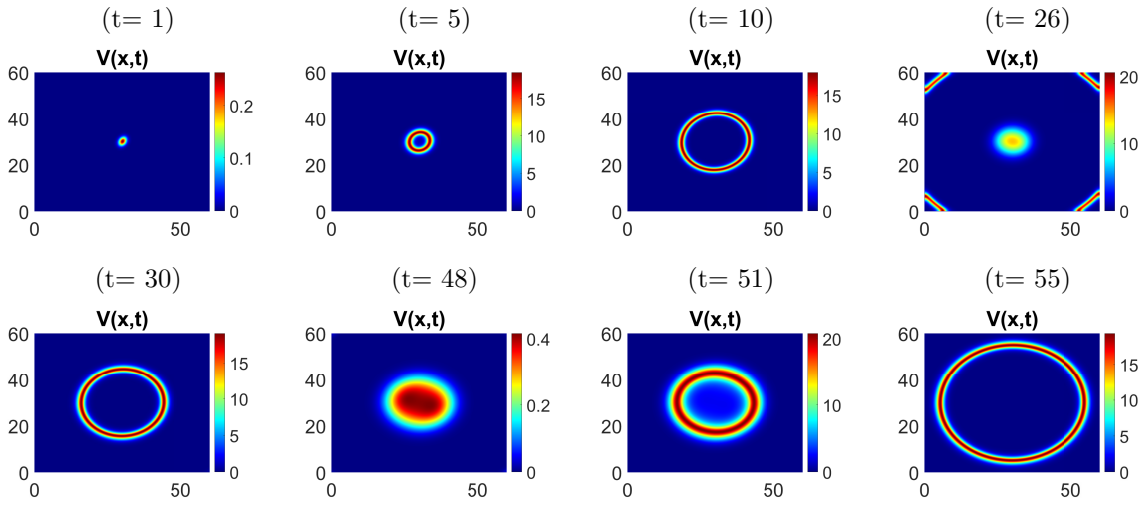

Figure 4.10: 2-D simulations of virus particles injected in the center of the tumor with $\theta = 900$, $a = 3.33$ and $\gamma = 13.33$.

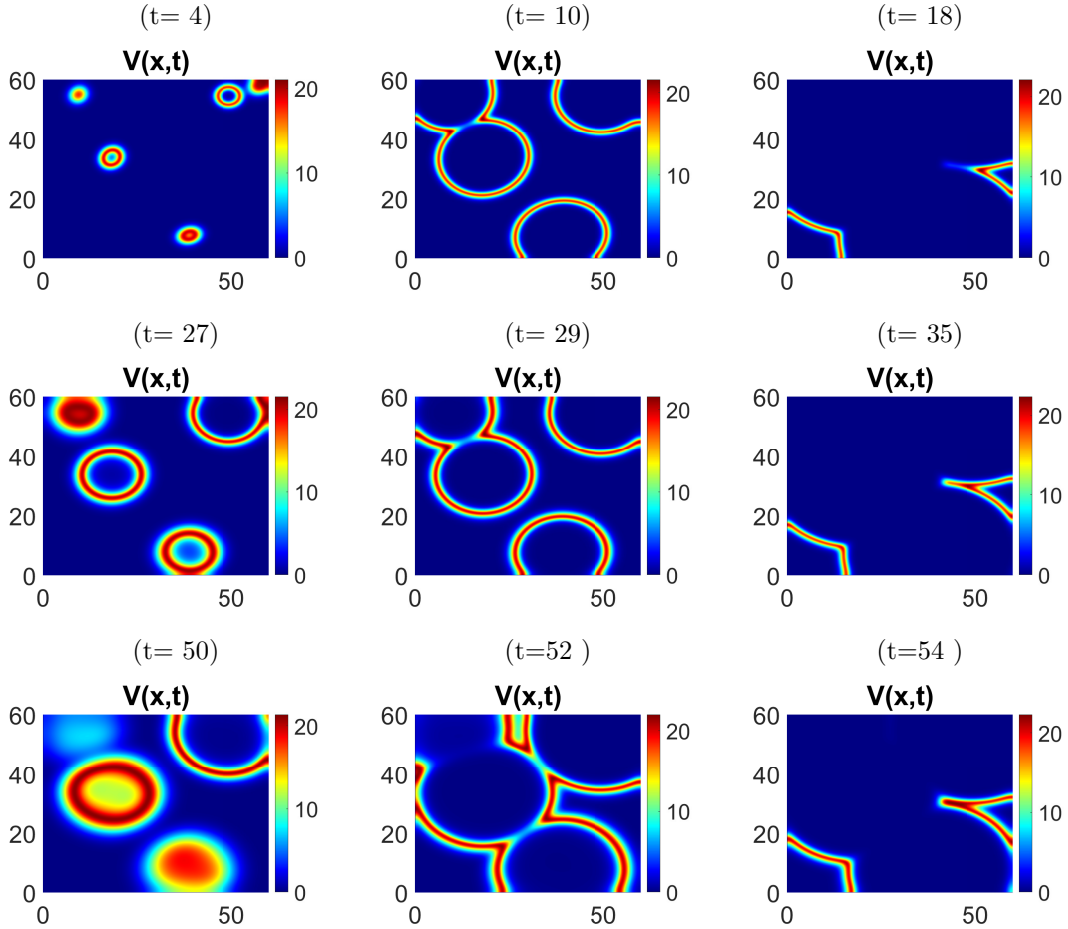

Figure 4.11: 2-D simulations of virus particles injected in the tumor randomly with $\theta = 900$, $a = 3.33$ and $\gamma = 13.33$.

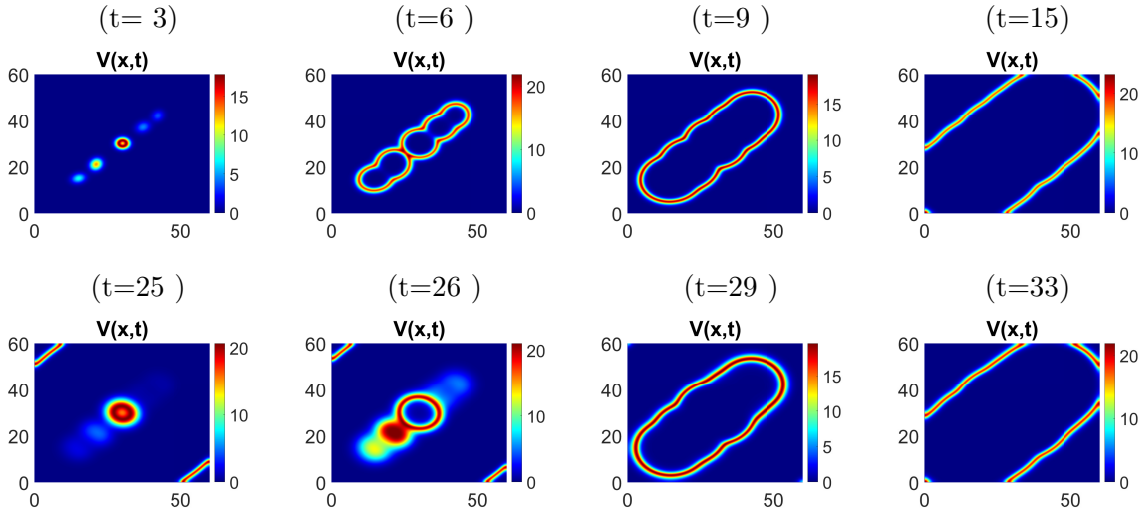

Figure 4.12: 2-D simulations of virus particles injected the tumor as diagonal with $\theta = 900$, $a = 3.33$ and $\gamma = 13.33$.

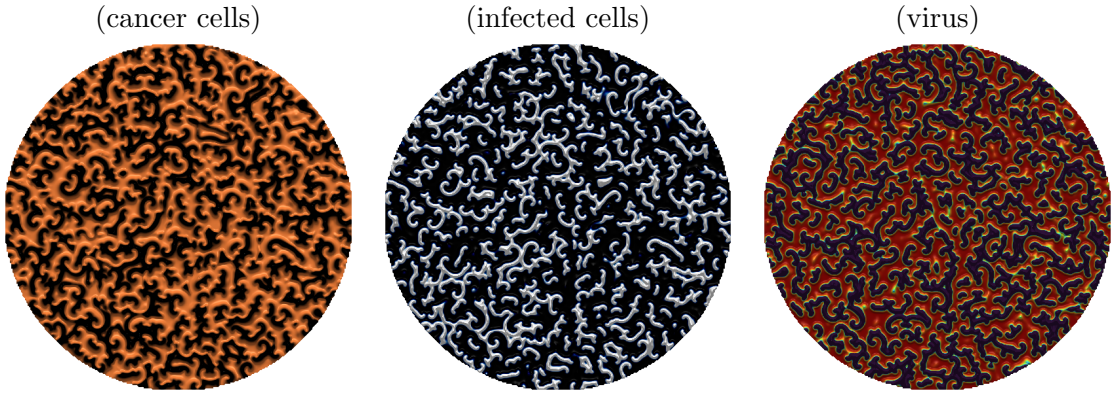

Figure 4.13: Simulations with *VisualPDE* [181] at time $t = 635$ (2116 days) with parameters from Table 3.2 and $\theta = 900$. The cancer cells on the left are shown from 0 (brown) to 0.2 (black). The scale for the infected cells is 0 (blue) to 0.05 (white), and the scale for the virus is 0 (blue) and 1 (red).

4.4 Conclusion

Continuing from Chapter 3, we delve into the examination of viral spatial patterns, this time considering the Michaelis-Menten kinetics. Our focus lies on investigating the results of oscillations stemming from the Hopf bifurcation and their implications in clinical practice.

Our simulations extending beyond a few days become unrealistic for predicting patient outcomes, as the adaptive immune response is typically activated within this timeframe [183]. However, we observe prolonged oscillations with a wavelength of more than 10 days, during which the tumor burden decreases close to zero. It is within these oscillatory outbreaks that we compute the tumor control probability (TCP).

In contrast to the TCP results obtained with the mass-action case, the TCP results with the Michaelis-Menten case were lower. Even with an increase in the viral production rate θ and employing multiple viral injection strategies, the maximum tumor control probability remains around 0.7149. Once again, these findings confirm the observation that oncolytic viral therapy alone is often insufficient in many cases [58, 59, 66, 97].

When comparing the viral wave speeds of the Michaelis-Menten and mass-action models, we observe that the viral wave speed of the Michaelis-Menten model is approximately one-third slower compared to that of the mass-action model. This discrepancy in wave speeds can contribute to the lower TCP values observed in the Michaelis-Menten model.

Additionally, considering the model with Michaelis-Menten kinetics, we still encounter a transcritical bifurcation θ_t and a Hopf bifurcation θ_H. However, in this case, the parameter θ_t for the transcritical bifurcation is shifted by a factor of $\frac{j+1}{j}$, where j represents the ratio of the Michaelis-Menten constant to the cancer cells carrying capacity.

Due to the absence of direct information for estimating the infection rate $\hat{\beta}$ for adenovirus using the Michaelis-Menten model, we resort to employing a Taylor expansion to establish a relationship between the infection rates of the mass-action β and Michaelis-Menten models, with $\hat{\beta}$ being larger than β.

Furthermore, conducting simulations in 2-D leads to the absence of the splitting peaks phenomenon observed in mass-action interactions. However, we still observe similar viral patterns as in the mass-action case, including filled rings, hollow rings, and concentric rings. Long-time simulations in Figure 4.13 reveal very complex spatio-temporal oscillations. Again, we believe these patterns can be relevant for other virus infections such as COVID-19 [187, 188], where patients suffering from long-lasting recurring effects result from continued oscillations.

Chapter 5

Analysis of Reovirus Binding and Plaque Size

5.1 Introduction

In this chapter, we investigate the oncolytic potential of reovirus, a nonpathogenic virus native to the enteric tract of mammals. As a double-stranded RNA virus, reovirus has demonstrated natural capabilities for infecting and lysing tumors under both in vitro and in vivo conditions [49, 52, 53, 193, 194]. The unmodified form of reovirus, referred to as T3wt, is currently undergoing evaluation in over 30 clinical trials targeting various cancer types, including metastatic breast cancer [194, 195], prostate cancer [196, 197], and colorectal cancer [49, 198]. Additionally, it has progressed to phase III clinical trials as a potential therapeutic intervention for breast cancer [195, 199].

Drs. Maya Shmulevitz and Francisca Cristi, researchers affiliated with the University of Alberta, have dedicated their laboratory efforts to the augmentation of reovirus for oncological therapeutic applications. Comprehensive experimental investigations were conducted on both the wild-type (T3wt) and the oncolytic mutated type (SV5) of reovirus. These investigations focused primarily on key parameters, including binding percentage, virus spread, and infectivity [52, 53]. The outcomes of these assessments underscore the importance of enhancing virus spread as a critical mechanism for optimizing therapeutic interventions in the context of oncolytic

virotherapy. The experimental results reveal a connection between the binding rate and viral spread, suggesting that a reduction in the binding rate leads to a more extensive viral spread, characterized by larger plaque sizes. In this context, plaque size refers to the area resulting from cells that have been infected. This observation highlights a distinct advantage that the mutated SV5 virus possesses over the wild-type T3wt, despite similarities in viral production and cell death. Concurrently, previous studies have delved into the dynamics of viral infection spread within cell culture contexts [200–202].

The phenomenon of viruses exhibiting reduced binding to host cells has been extensively documented in the scientific literature. Notably, reovirus variants with diminished affinity for sialic acid have been identified in both murine and human species. Furthermore, investigations into the infection dynamics of a sialic-acid-binding-deficient reovirus variant have revealed heightened infectivity when compared to the wild-type reovirus, particularly when infecting polarized epithelial cells from apical or basolateral orientations [203]. This suggests a potential selective advantage for viruses with reduced binding during the course of natural infections.

Similar observations have been made in the context of rotavirus mutants incapable of binding to sialic acid. Although these mutants displayed slower replication and lower titers in mouse cancer cell lines MA104, they paradoxically exhibited increased pathogenicity in mice [204]. This underscores the nuanced relationship between viral binding capabilities and infection outcomes under specific conditions.

Expanding beyond reoviruses and rotaviruses, other viruses have demonstrated the capacity to spread more extensively in monolayer cell cultures without a concomitant increase in replication. For instance, vaccinia virus-infected cells repel superinfecting virions, resulting in enhanced viral spread [205]. This phenomenon has also been observed with SV5. Additionally, reduced adsorption rates to host bacteria have been linked to increased plaque size in phages [206]. Moreover, various virus variants of polyomavirus, parvovirus, and Sindbis virus, characterized by deficiencies in binding,

have been shown to generate larger plaques in vitro [207–210]. Importantly, these variants exhibited higher pathogenicity and increased spread in vivo.

Building on Dr. Shmulevitz's experimental data [53], this chapter aims to address key questions through mathematical modeling: How does the virus spread correlate with the binding rate? What is the dependence of the invasion speed on the binding rate? How does the reduction in binding rate impact plaque sizes in vitro experiments? Is there an optimal binding rate, which maximizes viral spread?

To answer these questions, we develop two mathematical models that capture different aspects of viral dynamics. Model 1 focuses on a small time scale (less than 16 hours), enabling observation of viral spread without considering cell death and viral replication. Model 2 extends the analysis to a longer time scale (about 5 days), incorporating viral spread, cell death, and viral replication. Model 3 then includes the cancer cells explicitly, which allows us to compare plaque sizes of different experiments. The results of our models exhibit excellent concordance with the observed experimental phenomena, providing valuable insights into the dynamics of reovirus-mediated oncolytic therapy. We also compute the optimal binding rate that leads to the largest plaque size.

The outline of this chapter encompasses the following: we introduce a multi-scale mathematical modeling approach to investigate the dynamics of viral spread in cell culture experiments. The study begins with a short time scale model in Section 5.2, utilizing data from [53] to estimate the binding rate γ_b and viral diffusion coefficient D_{v}. Section 5.3 extends the model to longer time scales, incorporating events such as cell death and viral production. The viral spread speed is computed via travelling wave analysis, revealing the relationship between the binding rate γ_b and the viral spread speed c^* in Section 5.4. Model validation is presented in Section 5.5, where additional experimental data is considered. In Section 5.6 and Section 5.7 we present the main result on the optimal choice of the binding rate γ_b. The paper concludes in Section 5.8, contextualizing the results within the broader scope of mathematical

modeling and cancer and viral infection research.

5.1.1 Reovirus Experiments

Our mathematical models will be fitted and validated from the data of [53]. In [53] characteristics of T3wt and SV5 are empirically determined on monolayers of TUBO cells (spontaneously derived HER2+ murine breast cancer cells) and L929 cells (tumorigenic mouse fibroblasts). TUBO and L929 cells are exposed to T3wt or SV5 to measure cell attachment, virus replication, cell killing, and the size of plaques produced over several rounds of infection and re-infection. Reoviruses typically bind cells within an hour, enter in 3-4 hours, replicate exponentially until 15-18 hours, and newly-made viruses become released from cells at 18-20 hours post-infection (hpi). Accordingly, short-term infections of 1 hour are used to monitor binding. Long-term infections of up to 5 days are used to monitor plaque size. They find that among a variety of reovirus mutations, the variant SV5 (supervirus 5), which has five mutations in the virus genome, leads to the largest plaque sizes. Relative to T3wt, SV5 displays similar kinetics of replication in an infected cell, cell death of the infected cell, burst size (the titer of virus released from infected cell), and diffusion. However, SV5 binds less efficiently to cells, and also produces significantly larger plaques over several rounds of infection. While our mathematical modelling will use the empirical data derived on cancer cell cultures, it might be of interest to the reader that SV5 also significantly improves tumor regression and mouse survival in the more-complex mouse models of TUBO-derived tumors.

5.2 Model 1: Short Time Scale

First, we start by answering the following question: How far does the virus spread depending on the binding rate during a time scale that is short enough such that cell death and viral replication has not yet taken place? To answer this question, we use two sets of data from [53]. In short-time experiments the percentage of virus binding

after 1 hour to L929 cells was measured. These data will be used to estimate the binding rate γ_b. Second, to estimate viral diffusion in the extracellular medium, the viral load was measured after inoculation in a cell free medium.

On the short time scale of 1-16 hours, we consider only two processes, which is binding of the virus to the cells and diffusion of virions in the cell medium. Hence our model has the simple form

$$\frac{\partial V}{\partial t} = D_{\mathrm{v}} \Delta V - \gamma_b V \tag{5.1}$$

with the initial condition

$$V(x, y, 0) = V_0 \delta_0(x, y). \tag{5.2}$$

Here $V(x, t)$ denotes the titre of virus particles, D_{v} is the constant diffusion coefficient, γ_b is the constant binding rate and V_0 is the amount of virus particles at the start of the experiment $t = 0$. Equations (5.1)-(5.2), explain the virus spread in 2-D depending on the diffusion coefficient D_{v} and the binding rate γ_b. Here the virus is initiated at time 0 as a Dirac delta distribution at the centre of our domain. We use model (5.1) to estimate the binding rate γ_b and the diffusion coefficient D_{v}.

5.2.1 Binding Rate Estimation

To measure the binding rate γ_b, we use the data in [53], where three experiments for each reovirus type were completed to estimate the efficacy of reovirus attachments to tumor cells. Thus, a transformed murine tumorigenic L929 cells were exposed to equivalent virus particle doses and incubated at 4^oC for 1 hour to enable the virus attachment without entry into the cells (i.e. entry requires temperatures above 19^oC). The unbound virus particles were removed by washing the cells extensively before harvesting the post-binding lysates. Finally, Western blot analysis was used to calculate the percentage of cell-bound virus particles based on virus protein levels in the lysates versus the input. The results show that on average, 62% of T3wt virus

were bound to L929 cells, compared to on overage 24% of SV5 virus particles bound to cells (see Table 5.1.)

Virus Type	**% of Binding**	**mean ± error**	**half-life time** $t_{1/2}$
T3wt	80.64	61.63 ±10.14	0.722 h
T3wt	58.25		
T3wt	45.99		
SV5	24.25	24.18 ± 5.75	2.476 h
SV5	34.10		
SV5	14.19		

Table 5.1: The percentage of binding for each virus type at 1 hour for three data sets each. The estimated data range is computed.

The binding process can be easily described by a simple binding law

$$\frac{d}{dt}V(t) = -\gamma_b V(t), \qquad V(0) = V_0.$$

To estimate the binding rate γ_b, we assume the data in Table 5.1 is normally distributed and apply the likelihood method with the least square error (LSE) [108]. We denote the measured %-values of viruses binding as y_i, for i=1,2,3, as there are three independent data points for each virus. Using an exponential model, we can compute the number of unbound virus particles at time t as

$$V(t) = V_0 e^{-\gamma_b t}. \tag{5.3}$$

Then, the percentage of bound virus particles after $t = 1$ hour is

$$y_i = 1 - e^{-\gamma_b}.$$

Therefore, $\gamma_b = -\ln(1 - y_i)$. As there are several measurements for y_i, an average is necessary, which is generated using the maximum likelihood estimator and the corresponding confidence interval is then computed (see [108]).

Lemma 5.2.1 *The maximum likelihood estimator is*

$$\tilde{\gamma_b} = ln\left(\frac{1}{k}\sum_{i=1}^{k}(1 - y_i)\right). \tag{5.4}$$

Proof. Fixing t=1, let $x_i = 1 - y_i$, then the likelihood function of normal distribution is

$$\begin{aligned}\mathcal{L}(p) &= P(x_i = X_i,\ i = 1, ..., k | p = (\gamma_b, \sigma^2)) \\ &= \prod_{i=1}^{k} \frac{1}{\sqrt{2\pi}\sigma} e^{\frac{-(x_i - e^{-\gamma_b})^2}{2\sigma^2}}\end{aligned}$$

and the log-likelihood becomes

$$\mathcal{LL}(p) = -\sum_{i=1}^{k} ln(\sqrt{2\pi}\sigma) - \frac{1}{2\sigma^2} \sum_{i=1}^{n} \left(x_i - e^{-\gamma_b}\right)^2.$$

Now, we need to estimate the binding rate γ_b and the corresponding variance σ^2. To estimate γ_b, we compute the least square error and its γ_b-derivative as

$$\begin{aligned}LSE &= \sum_{i=1}^{k} (x_i - e^{-\gamma_b})^2 \\ \frac{d\,LSE}{d\gamma_b} &= 2e^{-\gamma_b} \left(\sum_{i=1}^{k} x_i - k e^{-\gamma_b} \right).\end{aligned}$$

To find maxima or minima in γ_b, we set the above derivative equal to zero and solve

$$\sum_{i=1}^{k} x_i - k e^{-\gamma_b} = 0$$

Therefore,

$$\gamma_b = -ln \left(\frac{1}{k} \sum_{i=1}^{k} x_i \right) = \tilde{\gamma_b}.$$

Thus, the maximum likelihood estimator is $\tilde{\gamma_b}$. To estimate the variance, we compute σ derivative as the following

$$\begin{aligned}\frac{d\,LL(p)}{d\sigma} &= -\frac{k}{\sigma} + \frac{1}{\sigma^3} \sum_{i=1}^{k} (x_i - e^{-\gamma_b})^2 \\ 0 &= \frac{1}{\sigma} \left[\frac{1}{\sigma^2} \sum_{i=1}^{k} (x_i - e^{-\gamma_b})^2 - k \right].\end{aligned}$$

Since $\sigma \neq 0$, we have

$$\begin{aligned}0 &= \frac{1}{\sigma^2} \sum_{i=1}^{k} (x_i - e^{-\gamma_b})^2 - k \\ k &= \frac{1}{\sigma^2} \sum_{i=1}^{k} (x_i - e^{-\gamma_b})^2\end{aligned}$$

Thus, we get

$$\sigma^2 = \frac{\sum_{i=1}^{k}(x_i - e^{-\gamma_b})^2}{k}. \quad \square \tag{5.5}$$

Applying the formula (5.4) and (5.5) to the data in Table 5.1, we find the binding rate for the wild type (T3wt) is $\gamma_{b\mathrm{T3wt}} = 0.96 \pm 0.16$ per hour, while for the mutated type (SV5) is $\gamma_{b\mathrm{SV5}} = 0.28 \pm 0.09$ per hour. These values can be related to the half-life of the virus population by

$$t_{1/2} = \frac{\ln 2}{\gamma_b}.$$

The T3wt virus population has a shorter time for binding with $t_{1/2} = 0.722$ hour compared to the SV5 virus population with $t_{1/2} = 2.476$ hours.

5.2.2 Diffusion Coefficient Estimation

The spatial diffusion of virus inside the culture medium without host cells was measured using the barrel of 1 mL syringes filled with semi-solid 0.5 % agar medium see Figure 5.1 (A). The virus was introduced at the top of the medium and allowed to diffuse over time. The medium was then removed from syringes and divided spatially into equal fractions (see Figure 5.1 (A)). Each fraction corresponds to 100 μL. The percentage of viral load that diffused into each fraction was measured at time $t = 120$ hours. The spatial extent of each fraction is approximately 0.55 cm as we can see in Figure 5.1 (A). To estimate the diffusion coefficient D_{v} at t=120 hour, we fit the data in Matlab by applying the Gaussian distribution formula for a diffusion process

$$V(x) = \frac{V_0}{\sqrt{4\pi D_{\mathrm{v}} t}} e^{\frac{-x^2}{4D_{\mathrm{v}} t}} \tag{5.6}$$

The parameters V_0 and D_{v} are then estimated, where V_0 is the number of viruses particles at t=0, which was not measured in the experiments.

From the data in [53], we have the percentage of the virus in each fraction. We consider each fraction as sub-interval with length 0.55 cm with the summation of

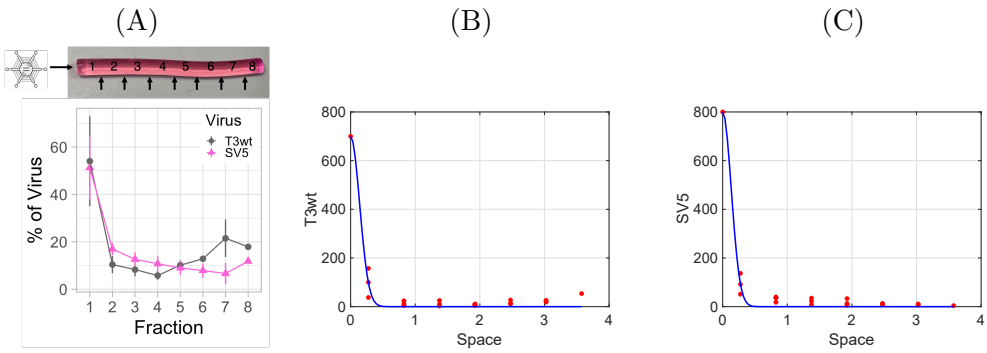

Figure 5.1: The diffusion coefficient estimation for T3wt and SV5 particles from the experiment in Cristi et al. [53]. **(A):** The diffusion of T3wt and SV5 from the experiment by measuring the percentage of the virus in each fraction at 120 hour, **(B):** The T3wt particles when $D_{\mathrm{v}} = 0.01$ mm^{2}per hour with $V_0 = 243$, and **(C):** The SV5 particles when $D_{\mathrm{v}} = 0.01$ mm^{2}per hour with $V_0 = 265$.

these sub-intervals correspond to the total viral contents. Since the virus percentage is measured for each medium fraction, we can use the area under the curve to estimate the diffusion coefficient.

There were no significant differences in the diffusion coefficients between T3wt and SV5 viruses. The estimated diffusion coefficient is $D_{\mathrm{v}} = 0.01 \pm 0.0015$ mm^2 per hour (equivalent $D_{\mathrm{v}} = 0.0001 \pm 0.000015\,\mathrm{cm}^2$ per hour) which is the best fit for our data as we can see in Figure 5.1 (B) and (C).

Another way to evaluate the diffusion coefficient D_{v} of small particles in a medium is by applying the Stokes-Einstein equation for the diffusion coefficient D_{v} of a spherical particle of radius r in a fluid of dynamic viscosity η at absolute temperature T [161]. We do not have any direct information from the data to estimate the value of the viscosity of the 0.5 % agar in Minimum Essential Media (MEM). Therefore, we use the viscosity of water which is also similar to the viscosity of Dulbecco's Modified Eagle Medium (DMEM) (10 % FBS where FBS refers to a Fetal Bovine Serum) [162]. Thus, in our case the Stokes-Einstein relation gives

$$D_{\mathrm{v}} = \frac{k_B T}{6\pi\eta r} = 0.02\,\mathrm{mm}^2 \text{ per hour},$$

where k_B is Boltzmann's constant, $r = 35$nm [211] is a typical virus radius, and

	D_{V} **(mm^2 per hour)**
Our model fit estimation	0.01 ± 0.0015
Stokes-Einstein estimation [161]	0.02
Rioja et al. [70] estimation	0.014
Poolandvand et al. [88] estimation	0.01

Table 5.2: Comparison between the value of the viral diffusion coefficient that have been estimated in our model, by Stokes-Einstein relation, by Rioja et.al model [70] and by Poolandvand et al. model [88].

$\eta = 0.001$ pa.s is the viscosity of water at $T = 21^oC$. The values of diffusion coefficient in our estimation and Stokes-Einstein are very close. Furthermore, [70] and [88] use a similar diffusion coefficient of $D_{\mathrm{Rioja}} = 0.014$ mm^2 per hour and $D_{\mathrm{P}} = 0.01$ mm^2 per hour for cancer viral therapy, which are similar to our value $D_{\mathrm{V}} = 0.01$ mm^2 per hour as we can see in Table 5.2.

5.2.3 Result: Prediction of the Spread Radius for Short Times

Now, as we estimated the diffusion coefficient D_{V} and the binding rates γ_b, we come back to model (5.1) to evaluate the spread radius r as a function of the binding rate γ_b.

We solve equations (5.1)-(5.2) with a little trick by setting $\phi = Ve^{\gamma_b t}$. Then

$$\phi_t = V_t e^{\gamma_b t} + \gamma_b V e^{\gamma_b t} = e^{\gamma_b t}\left(V_t + \gamma_b V\right) = D_{\mathrm{V}} e^{\gamma_b t}\Delta V = D_{\mathrm{V}}\Delta\phi.$$

Hence ϕ satisfies a linear heat equation, which we can solve explicitly using the fundamental solution in 2-D [108].

$$\phi(x, y, t) = \frac{V_0}{4\pi D_{\mathrm{V}} t} e^{\frac{-x^2-y^2}{4D_{\mathrm{V}}t}}.$$

Using $\phi = Ve^{\gamma_b t}$, we obtain

$$V(x, y, t) = e^{-\gamma_b t}\frac{V_0}{4\pi D_{\mathrm{V}} t} e^{\frac{-x^2-y^2}{4D_{\mathrm{V}}t}}. \tag{5.7}$$

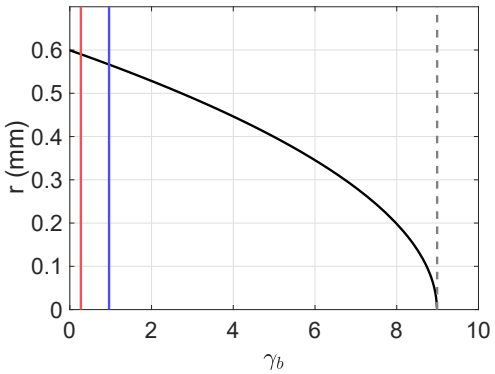

Figure 5.2: The spread radius values as function of the binding rate γ_b (per hour) with $D_V = 0.01$ mm^2 per hour, and $\frac{V_0}{V_{\min}} = 1000$ virus at t=1 hour. The blue line represents the value of $\gamma_{b\mathrm{T3wt}} = 0.96$, while the red line represents the value of $\gamma_{b\mathrm{SV5}} = 0.28$.

To compute the spread radius $r = \sqrt{x^2 + y^2}$, we assume that below a level of $V_{\min}$ no virus can be measured. Hence at the spread radius r we have

$$V_{\min} = e^{-\gamma_b t} \frac{V_0}{4\pi D_{\mathrm{V}} t} e^{\frac{-r^2}{4D_{\mathrm{V}} t}}.$$

We solve this equation for r and obtain

$$r = \sqrt{4D_{\mathrm{V}} t \left(ln \left[\frac{V_0}{4\pi D_{\mathrm{V}} V_{\min} t} \right] - \gamma_b t \right)}. \tag{5.8}$$

Fixing the time t, the diffusion coefficient D_{V}, the number of virus particles at t=0 i.e V_0, and the threshold $V_{\min}$, we have the spread radius r as a function of the binding rate γ_b. We show this dependence in Figure 5.2. In Figure 5.2 we also show the estimated binding rate for the wild type virus in blue ($\gamma_{b\mathrm{T3wt}} = 0.96$ per hour) and for SV5 in red ($\gamma_{b\mathrm{SV5}} = 0.28$ per hour). Furthermore, we see that the spread radius declines as the binding rate increases, until after a maximum binding rate of $\gamma_b > \gamma_b^* = 9.0$, no more spread is possible.

5.3 Model 2: Long Time Scale

5.3.1 Basic Assumptions and the Mathematical Model

In this section, we study the viral spread for time scales that include viral replication inside the cells, virion release and cell death, (i.e. more than 16 hours). Thus, we

explain the plaque size results on L929 cell monolayers in [53]. Plaque size refers to the area of dead cells that result from the viral infection. The larger the plaque size, the farther the virus has spread. In [53], a monolayer of L929 cells was subjected to infection by reovirus particles. Following a one-hour incubation at 37^oC, a 0.5% agar overlay was introduced onto the cells. Once the agar solidified, the cells were placed back into the 37^oC incubator for a period of 5 days. Afterward, the cells were treated with 4% paraformaldehyde (PFA) for fixation and the cellular monolayer was stained using a 1% (wt/vol) crystal violet solution. Subsequently, plaque size analysis was performed using the Fiji software with the particle analysis plugin and the results expressed as a relative plaque size to T3wt after normalization T3wt plaque size to 1.

To analyze the results of plaque size in [53], we assume that the number of cells that can be infected during the experiment is about constant. This is a strong assumption, but we feel that it is justified, since the model shows good results. We include a class of infected cells $I(x,t)$ and extend our previous model (5.1) as

$$\begin{aligned} \frac{\partial I}{\partial t} &= \gamma_b \nu V - \alpha I \\ \frac{\partial V}{\partial t} &= D_{\mathrm{v}} \frac{\partial^2 V}{\partial x^2} + \alpha \tilde{b} I - \gamma_b V, \end{aligned} \tag{5.9}$$

where the virus diffusion coefficient D_V and the binding rate γ_b are the same as before in model (5.1)-(5.2). The percentage of binding viruses that lead to infection is denoted by ν. The infected cells die at rate α, and the burst size of the infectious viruses is denoted by $\tilde{b}$. Here, we would like to indicate that the rate of virus replication in infected cells are expressed in some papers by parameter b, where b represents the infected cells death rate $\times$ the virus burst size [69, 201, 212]. This is equivalent in our model to $b = \alpha\tilde{b}$.

In addition to γ_b and D_{v}, we have three more parameters to estimate: the death rate of infected cells α, the percentage of binding virus that lead to an infection ν, and the burst size $\tilde{b}$. We estimate these values in the next subsections and summarize

the values in Table 5.4.

In [53] the percentage of cell death at time points 15, 18, 24, 30 and 36 hour after inoculation had been measured for each virus type T3wt and SV5. We show these data in Table 5.3 and illustrate them in Figure 5.3 (A). While for 15 and 18 hours, only one data point had been measured compared to three data points at time 24 hour and two data points at time 30 and 36 hours each. From the data, we can see that the cells are surviving between 15-24 hours with no significant differences based on the virus type. The death rate of infected cells α at different time points can be estimated by data fitting of the exponential function $I(t) = 1 - e^{-\alpha t}$ using MATLAB, as shown in Figure 5.3 (B) and (C). We find no significant difference between the death rate of the T3wt virus and SV5 virus, which is consistent with the data observation. Therefore, we estimate the death rate of infected cells as $\alpha = 0.057 \pm 0.030$ per hour.

Virus Type	**Time**	**% of Cell Death**	**Estimated Data**
T3wt	15	1.470	
T3wt	18	40.15	
T3wt	24	34.38	36.72 ± 5.27
T3wt	24	46.79	
T3wt	24	28.99	
T3wt	30	58.64	68.36 ± 9.72
T3wt	30	78.08	
T3wt	36	62.35	71.49 ± 9.14
T3wt	36	80.63	
SV5	15	1.34	
SV5	18	39.05	
SV5	24	25.68	31.25 ± 6.751
SV5	24	44.69	
SV5	24	23.39	
SV5	30	45.34	60.81 ± 15.47
SV5	30	76.28	
SV5	36	52.15	64.99 ± 12.84
SV5	36	77.83	

Table 5.3: The percentage of cell death at different time points for T3wt and SV5 particles from the experiment in Cristi et al. [53]. The estimated data range is computed.

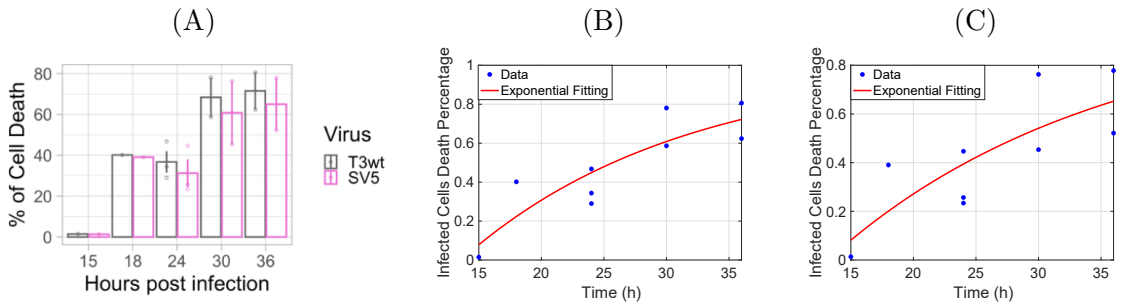

Figure 5.3: The death rate of infected cells estimation for T3wt and SV5 particles from experiment in Cristi et al. [53]. **(A)**: The percentage of cell death at different time points. **(B)**: T3wt virus and **(C)**: SV5 virus. Infected cell counts (blue dots) and the theoretical curve $I(t) = 1 - e^{-\alpha t}$ (in red).

5.3.2 Viral Burst Size Estimation

The burst size of the virus is the number of released new virions from one infected cell. Experimentally in [53], the released number of virions had been measured with two data sets with multiplicity of infection (MOI) 21 for T3wt and 27 for SV5, respectively, at different time points: 0, 3, 6, 9, 12, 15, 18, 24, 30, and 36 hour. The Multiplicity of Infection (MOI) refers to the number of virions that are added per cell during infection. The data are shown in Figure 5.4 (A). In Figures 5.4 (B), and (C) we use a logistic fit for these data and estimate the burst size as the carrying capacity value for this logistic fit. We find $\tilde{b}_{\text{T3wt}} = 514 \pm 114$ viable virions per cell and $\tilde{b}_{\text{SV5}} = 732 \pm 146$ viable virions per cell, respectively. Note that the confidence intervals for these two values overlap. Hence, as reported already in [53], there is no statistically significant difference in those values. This is an important observation, and we come back to this issue later.

5.3.3 Percentage of Infectious Viral Particles

The results in [213], show that the percentage of bound reovirus that lead to an infection is in the range of $\nu \in [\frac{1}{1000}, \frac{1}{100}]$ cells per virus. We choose $\nu = 0.01$ cell per virus [1]. This means out of 100 binding viruses on average one virus leads to a

[1] After personal communication with Dr. Shmulevitz and Dr. Cristi.

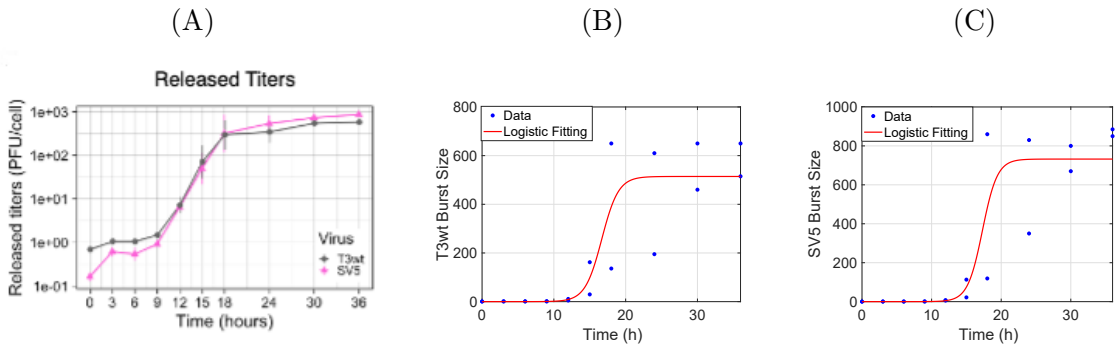

Figure 5.4: The burst size virus estimation for T3wt and SV5 particles from experiment in Criesti et al. [53]. **(A)**: The percentage of viral burst size at different time points.**(B)**: $\tilde{b}_{\mathrm{T3wt}} = 514$ infectious virus per cell **(C)**: $\tilde{b}_{\mathrm{SV5}} = 732$ infectious virus per cell. The blue dots show the measured released viral particles per cell, while the red curve shows our logistic fit

successful infection.

The parameters values are summarized in Table 5.4.

Parameter	**Description**	**Value**	**Unit**
D_{V}	Diffusion coefficient of reovirus	0.01 ± 0.0015	mm^2 per hour
$\gamma_{b\mathrm{T3wt}}$	Binding rate of wild type	0.96 ± 0.16	per hour
$\gamma_{b\mathrm{SV5}}$	Binding rate of SV5	0.28 ± 0.09	per hour
α	Death rate of infected cells	0.057 ± 0.030	per hour
ν	Percentage of binding reovirus leads to infection	0.01	cell per virus
$\tilde{b}$	Infectious burst size of reovirus	500-1000	virus per cell
$\tilde{b}_{\mathrm{T3wt}}$	Infectious burst size of T3wt	514 ± 114	viable virions per cell
$\tilde{b}_{\mathrm{SV5}}$	Infectious burst size of SV5	732 ± 146	viable virions per cell

Table 5.4: Estimated parameter values of system (5.9).

5.4 Model Analysis

Now, as all model parameters are identified, we can begin its analysis.

5.4.1 Viral Replication Number

A useful quantity for the analysis of our model is the virus replication number (VRN) i.e R_{v} of the ODE system (5.9) as defined in [201]. Since the system (5.9) is linear and the only steady state is $(I, V) = (0, 0)$, then the corresponding eigenvalue problem is

$$A \begin{bmatrix} I \\ V \end{bmatrix} = \lambda \begin{bmatrix} I \\ V \end{bmatrix} \quad \text{where} \quad A = \begin{bmatrix} -\alpha & \gamma_b \nu \\ \alpha \tilde{b} & -\gamma_b \end{bmatrix} \tag{5.10}$$

Condition $\det A = 0$ can be written as $R_{\mathrm{v}} = 1$, where

$$R_{\mathrm{v}} = \tilde{b}\nu. \tag{5.11}$$

The stability of the steady state $(I, V) = (0, 0)$ is determined by R_{v}. Mathematically, if $R_{\mathrm{v}} < 1$, then both eigenvalues of the matrix A are negative and hence the steady state (0,0) is stable. Biologically, this means that the virus dies out. On the other hand, if $R_{\mathrm{v}} > 1$, then we have one positive eigenvalue and the second eigenvalue is negative. Therefore, the steady state is unstable and hence the virus can spread to infect the neighbouring cells and as a result the virus population grows. From the experimental data, we find that $R_{\mathrm{v}} = \tilde{b}\nu > 1$, where $R_{\mathrm{VT3wt}} = 5.14 \pm 1.14$ and $R_{\mathrm{VSV5}} = 7.32 \pm 1.46$, respectively.

5.4.2 Travelling Invasion Wave

One way to understand the effect of the binding rate γ_b on the viral invasion in the L929 cell culture is the invasion wave analysis. Here we assume that $R_{\mathrm{v}} > 1$, such that the virus can grow. The speed c of the virus invasion is then called the wave speed and there is an established theory to estimate it [107]. Since our model (5.9) is linear we use the leading edge method, where we focus on the behaviour of the front profile of the invasion, near the steady state $(I, V) = (0, 0)$. We use c to denote the invasion wave speed and λ to denote its exponential decay rate. Hence we look for solutions of the form $(I(x,t), V(x,t)) = (\varepsilon_i e^{-\lambda z}, \varepsilon_v e^{-\lambda z})$ with $z = x - ct$ and small

constants $\varepsilon_i, \varepsilon_v$. Substituting the Ansatz for $(I(x,t), V(x,t))$ into system (5.9), we get

$$\begin{aligned} \gamma_b \nu \varepsilon_v - c\lambda\varepsilon_i - \alpha\varepsilon_i &= 0 \\ D_{\mathrm{v}}\lambda^2\varepsilon_v - c\lambda\varepsilon_v + \alpha\tilde{b}\varepsilon_i - \gamma_b\varepsilon_v &= 0 \end{aligned} \tag{5.12}$$

We write system (5.12) in a matrix form $A\varepsilon = 0$,

$$\begin{bmatrix} -(c\lambda+\alpha) & \gamma_b\nu \\ \alpha\tilde{b} & D_{\mathrm{v}}\lambda^2 - c\lambda - \gamma_b \end{bmatrix} \begin{bmatrix} \varepsilon_i \\ \varepsilon_v \end{bmatrix} = \begin{bmatrix} 0 \\ 0 \end{bmatrix}. \tag{5.13}$$

Thus, to obtain a non-trivial solution, we assume that the determinant of the matrix A is zero. The characteristic equation of (5.13) is

$$-(c\lambda+\alpha)\left(D_{\mathrm{v}}\lambda^2 - c\lambda - \gamma_b\right) - \alpha\gamma_b\tilde{b}\nu = 0. \tag{5.14}$$

Following a method of Volpert [201], we introduce $\varrho = c\lambda > 0$, substitute it into (5.14) and solve it for c^2 to obtain

$$c^2 = \chi(\varrho) := \frac{D_{\mathrm{v}}\varrho^2(\alpha+\varrho)}{\varrho^2 + (\alpha+\gamma_b)\varrho - \alpha\gamma_b(\tilde{b}\nu - 1)}. \tag{5.15}$$

Next we show that $\chi(\varrho)$ has a unique positive minimum at ϱ^* such that the minimal wave speed c^* is given by

$$c^* = \sqrt{\chi(\varrho^*)}.$$

Consequently, we find the decay rate of the invasion with minimal speed as

$$\lambda^* = \frac{\varrho^*}{c^*}. \tag{5.16}$$

For the parameter values that we estimated for the two virus types T3wt and SV5, as reported in Table 5.4, we plot the curves $\chi(\varrho)$ in Figure 5.5 (A). The function $\chi(\varrho)$ has zeros at $\varrho = 0$, and $\varrho = -\alpha$, which are not relevant since we require $\varrho > 0$. Also, $\chi(\varrho)$ has a vertical asymptote at

$$\varrho_v = \frac{-(\alpha+\gamma_b) + \sqrt{(\alpha+\gamma_b)^2 + 4\alpha\gamma_b(\tilde{b}\nu - 1)}}{2} > 0. \tag{5.17}$$

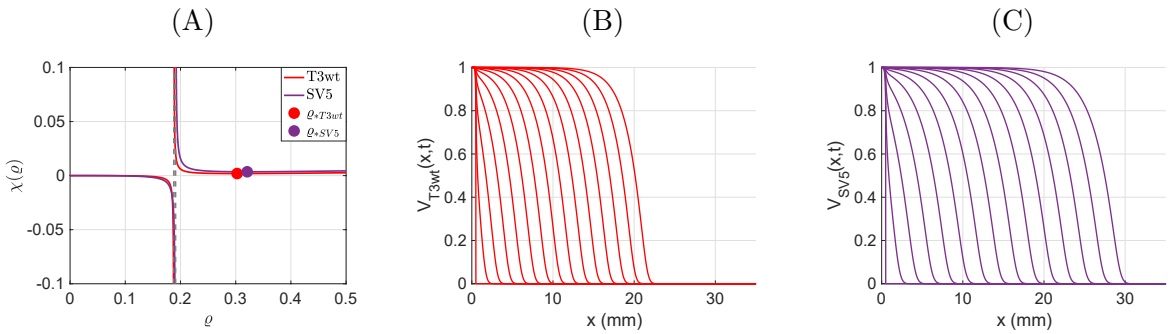

Figure 5.5: The travelling wave when we vary the binding rate γ_b for the T3wt and the SV5 with $D_{\mathrm{V}} = 0.01$, $\alpha = 0.057$, and $\nu = 0.01$. **(A)**: $\gamma_{b\mathrm{T3wt}} = 0.96$, with $\tilde{b} = 514$, **(B)**: $\gamma_{b\mathrm{SV5}} = 0.28$, with $\tilde{b} = 732$.

The positive minima, indicated as dots in Figure 5.5 (A), are right of the asymptote, hence we define

$$c^* = \sqrt{\min_{\varrho > \varrho_v} \chi(\varrho)}. \tag{5.18}$$

For the parameter values from Table 5.4 we get

$$c^*_{\mathrm{T3wt}} = 0.04366 \text{ mm per hour} \quad \text{and} \quad c^*_{\mathrm{SV5}} = 0.05941 \text{ mm per hour}. \tag{5.19}$$

In Figure 5.5 (B) and (C) we show numerical simulations of the invasion waves for these parameters. We see that the invasion wave of T3wt (B) is slower than the invasion of the SV5 virus (C). If we compute the invasion speeds numerically, we find

$$c_{\mathrm{T3wt}} = 0.04373 \text{ mm per hour} \quad \text{and} \quad c_{\mathrm{SV5}} = 0.05990 \text{ mm per hour},$$

which is very close to the theoretical values above (5.19).

We also determine the corresponding invasion front decay rate (λ^*) by formula (5.16) and find

$$\lambda^*_{\mathrm{T3wt}} = 6.9 \,\text{per mm}, \quad \text{and} \quad \lambda^*_{\mathrm{SV5}} = 5.4 \,\text{per mm}. \tag{5.20}$$

5.5 Validation of Model 2 on Invasion Front Data

In the previous sections we estimated all the model parameters as summarized in Table 5.4, plus the invasion speeds c^* and the decay rates λ^* at the edge of the

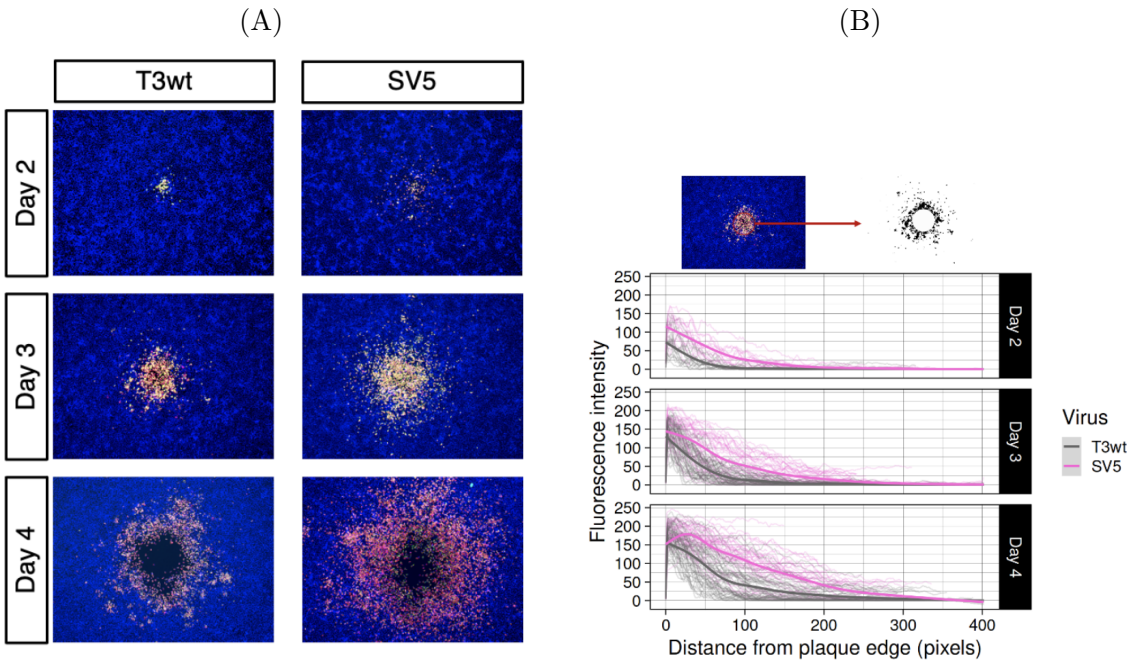

Figure 5.6: SV5 spread farther than T3wt. **(A)**: Immunofluorescence pictures of T3wt and SV5 plaques formation at days 2, 3 and 4 post infection, **(B)**: Quantification of the fluorescence from the edge of the plaque to represent the spread of the virus. (or Figure 6 (H) and (I) in [53].)

invasion front. To validate our model (5.9) we compare it now to data that have not been used to parameterize the model. The set of data is an experiment in [53] where we use fluorescence measurements of viral load at the edge of the plaques.

When plaques are evaluated by crystal violet staining, as in the above experiments, then plaque size reflects the size of the clearance produced by killing cells in the center. Crystal violet staining does not, however, reveal the extent of cells that are infected by virus but are still alive. Therefore, immunofluorescence was used to directly visualize reovirus-infected cells in the plaques over days 2, 3 and 4 post infection [53]. The immunofluorescence allowed visualization of individual infected cells at the rim of the plaque Figure 5.6. In these experiments, SV5 infected cells at a further distance from the origin of infection (i.e. center of the plaque) relative to T3wt. Mathematically, this can be represented by estimating the decay rate λ of the invasion front of T3wt and SV5 viruses from the plaque edge.

To estimate the decay rates of the T3wt invasion front λ_{T3wt} and the SV5 invasion front λ_{SV5} from the data, we apply MATLAB to fit the data in Figure 5.6 with an exponential decay function for the flourescence value $Fl(x,t) = e^{-\lambda(x-s)}$, where λ is the invasion front decay rate and s is a shift of the exponential decay function to place it at the best location for the fit. In Figures 5.7 and 5.8 we show this fit in red with the corresponding data in blue.

In Figure 5.7 we find the best fit decay rates on days 2,3,4 to be $\lambda = 0.029 \pm 0.001, 0.022 \pm 0.0004, 0.014 \pm 0.0003$ per pixel, which has a mean value of $\lambda = 0.022$ per pixel. There are 445 pixel per mm, hence we find $\lambda_{\text{T3wt}} = 9.8$ per mm. This corresponds well with the previous estimate in (5.20) of $\lambda^*_{\text{T3wt}} = 6.9$ per mm. For the supervirus SV5 we find the decay rates $\lambda = 0.015 \pm 0.0005, 0.011 \pm 0.0002, 0.007 \pm 0.0002$ per pixel, with an average of 0.011. This corresponds to $\lambda_{\text{SV5}} = 4.95$ per mm. Again, this is very close to the theoretical value of $\lambda^*_{\text{SV5}} = 5.4$ per mm from (5.20).

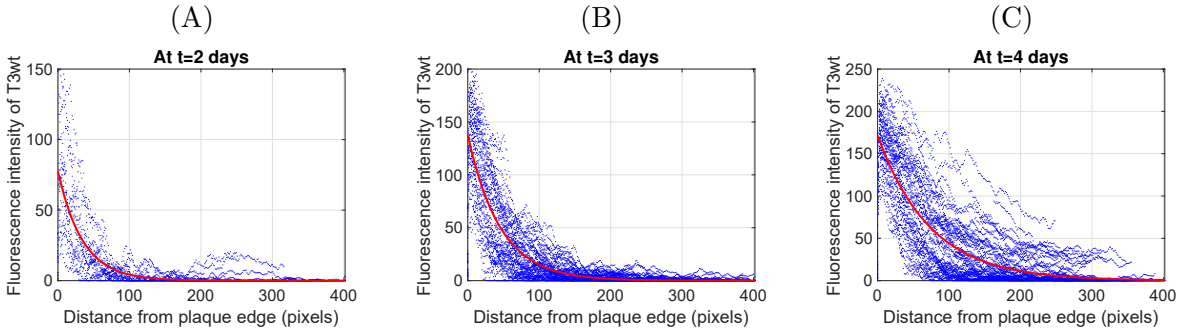

Figure 5.7: The T3wt invasion front's decay rate is illustrated by the blue dots, depicting the data of the viral spread from the plaque's edge. The red curve represents the best fit decay rates. **(A)**: $\lambda = 0.029$ at t= 2 days **(B)**:$\lambda = 0.022$ at t=3 days and **(C)**:$\lambda = 0.014$ at t=4 days.

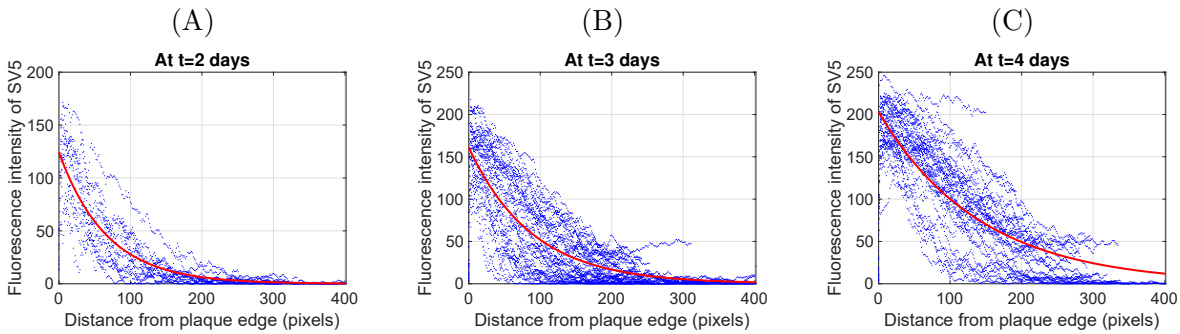

Figure 5.8: The SV5 invasion front's decay rate is illustrated by the blue dots, depicting the data of the viral spread from the plaque's edge. The red curve represents the best fit decay rates. **(A)**: $\lambda = 0.015$ at t= 2 days **(B)**: $\lambda = 0.011$ at t=3 days and **(C)**: $\lambda = 0.007$ at t=4 days.

5.6 The Relationship Between Binding Rate and Wave Speed

The relationship between the binding rate γ_b and the invasion wave speed is very important. To optimize the efficacy of reovirus treatment, we like to find the binding rate $\gamma_{b\max}$ that maximizes the viral invasion speed c^*. The minimal invasion speed is given by formula (5.18), where the function $\chi(\varrho)$ and the value of the asymptote ϱ_v both depend on the binding rate γ_b. We first look at the extreme cases $\gamma_b = 0$ and $\gamma_b \to \infty$.

In the case of no virus binding ($\gamma_b = 0$), there will be no invasion, since the virus cannot replicate. In this case we expect $c^* = 0$. Indeed, in case of $\gamma_b = 0$, direct calculation in (5.15) and (5.17) shows that

$$\varrho_v = 0 \quad \text{and} \quad \chi(\varrho) = D_{\mathrm{V}}\varrho,$$

and

$$c^* = \sqrt{\min_{\varrho \geq 0} \chi(\varrho)} = 0.$$

This means when the binding rate $\gamma_b = 0$, the wave speed for T3wt and SV5 viruses is zero.

In the other extreme of very strong binding $\gamma_b \to \infty$, the virus will bind immediately to cells and will no longer be able to invade any further. So we also expect $c^* = 0$. In this case we have the singularity of $\chi(\varrho)$ at $\varrho_v = \alpha(\tilde{b}\nu - 1)$. For $\varrho > \varrho_v$ we can apply L'Hopital's rule to $\chi(\varrho)$ given in (5.15) to consider the limit as $\gamma_b \to \infty$. We find

$$\lim_{\gamma_b \to \infty} \chi(\varrho) = 0,$$

which implies $c^* = 0$.

Since in the two extreme cases of γ_b the invasion speed is zero, and since χ and ϱ_v depend continuously on γ_b for $\varrho > \varrho_v$, we conclude that there is at least one maximum of c^* for some intermediate value $\gamma_b \in (0, \infty)$.

To find this value we consider the critical points of $\chi(\varrho)$:

$$\begin{aligned}
0 =& \chi'(\varrho) \\
=& \frac{D_{\mathrm{v}}\varrho\left(\varrho^3 + 2(\alpha+\gamma_b)\varrho^2 + (\alpha^2 + 4\alpha\gamma_b - 3\alpha\gamma_b\tilde{b}\nu)\varrho - 2\alpha^2\gamma_b(\tilde{b}\nu - 1)\right)}{\left[\varrho^2 + (\alpha+\gamma_b)\varrho - \alpha\gamma_b(\tilde{b}\nu - 1)\right]^2} \\
=& \frac{D_{\mathrm{v}}\varrho P_3(\varrho)}{P_2^2(\varrho)},
\end{aligned}$$

where

$$P_3(\varrho) = \varrho^3 + 2(\alpha+\gamma_b)\varrho^2 + (\alpha^2 + 4\alpha\gamma_b - 3\alpha\gamma_b\tilde{b}\nu)\varrho - 2\alpha^2\gamma_b(\tilde{b}\nu - 1).$$

and

$$P_2(\varrho) = \varrho^2 + (\alpha+\gamma_b)\varrho - \alpha\gamma_b(\tilde{b}\nu - 1).$$

Thus, $\chi'(\varrho) = 0$ when $\varrho = 0$ or $P_3(\varrho) = 0$. Clearly, the coefficient of ϱ^3 and ϱ^2 are positive while the sign of the coefficient of ϱ^0 is negative. The sign of the coefficient of ϱ depends on the value of γ_b after fixing the parameter values of α, $\tilde{b}$, and ν.

Based on Descartes' rule of signs [214] even if the sign of the coefficient ϱ is positive or negative, we have only one positive real root and 2 or zero negative real roots of P_3. Therefore, there exist a unique $\varrho^* > 0$, such that $\chi'(\varrho^*) = 0$. Furthermore, at $\varrho = 0$, we have $P_3(0) = -2\alpha^2\gamma_b(\tilde{b}\nu - 1) < 0$, with the continuity of $P_3(\varrho)$ and being concave

up since $P_3''(\varrho) = 6\varrho + 4(\alpha + \gamma_b) > 0$ for each $\varrho \geq 0$. Therefore, by the Intermediate Value Theorem and the Mean Value Theorem, there is only one positive real root i.e $\varrho^* > 0$ such that $P_3(\varrho^*) = 0$. Thus for each $\gamma_b > 0$, $\chi(\varrho^*)$ is a unique minimum with $P_3(\varrho^*) = 0$ for $\varrho^* > \rho_v$. The maximum possible invasion speed is then

$$c^*_{\max} = \max_{\gamma_b \in (0,\infty)} c^*(\gamma_b).$$

For the parameter values from Table 5.4 for T3wt and SV5 we plot the function $c^*(\gamma_b)$ as red line for T3wt and in purple for SV5 in Figure 5.9 (A). As red and purple points we indicate the estimated binding rates for the corresponding cases, and in black we indicate the maximum of these curves.

- For T3wt (red curve) we observe that the invasion speed could be increased by reducing the binding rate γ_b from 0.96 per hour to 0.29 per hour. In that case the speed would change from 0.044 mm per hour to 0.048 mm per hour. Expressed in percentage of binding after one hour, we aim to decrease the percentage of binding of T3wt virus from 61.7 % to 25.9 %.

- In the case of SV5 (purple curve) we see that an increase in binding rate from 0.28 to 0.42 would have a small accelerating effect from $c^* = 0.059$ to 0.060. In other words, we like to increase the percentage of binding of SV5 virus after one hour from 24.4 % to 34.3 %.

- We also notice that this result depends on the burst size of the corresponding virus. As indicated earlier, and also in [53], the difference in the burst sizes is not statistically significant. Hence we add, in blue, the corresponding curve for the mean burst size of $\tilde{b} = 623$. The curve is very similar to the red and purple curves and the maximum invasion speed of $c^* = 0.054$ is found for a binding rate near 0.36.

- We also considered some extreme cases for the burst size of $\tilde{b} = 500$ and $\tilde{b} = 1000$. For $\tilde{b} = 500$ we find $\gamma_{b\max} = 0.28$ per hour with corresponding wave

speed $c^*_{\max} = 0.04775$ mm per hour, while for the upper bound of burst size $\tilde{b} = 1000$ virus per cell we find $\gamma_{b\max} = 0.5$ per hour with corresponding wave speed $c^*_{\max} = 0.07154$ mm per hour.

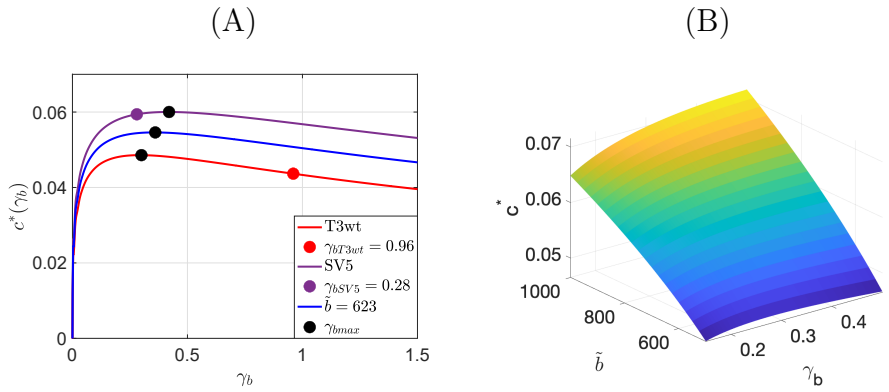

Figure 5.9: (A) The relationship between the binding rate γ_b and the invasion speed c^* for T3wt, SV5, and when $\tilde{b} = 623$. We plot the function (5.15) for different values of γ_b to find the maximum $\gamma_{b\max}$ that leads to maximum wave speed i.e $c^*_{\max}$. The numerical results indicate that for T3wt virus, the $c^*_{\max} = 0.04858$ at $\gamma_{b\max} = 0.29$, while the $c^*_{\max} = 0.06002$ at $\gamma_{b\max} = 0.42$ for SV5 virus. Finally, when we choose intermediate value of infectious burst size $\tilde{b}$, we find the $c^*_{\max} = 0.05460$ at $\gamma_{b\max} = 0.36$. (B) The values of the minimum wave speed c^* when we vary the binding rate γ_b and the burst size $\tilde{b}$. The maximum wave speed c^* is 0.07154 when $\gamma_b = 0.5$ and $\tilde{b} = 1000$. The values of the binding rate in (B) have the range $\gamma_b \in [0.15, 0.5]$.

The previous results emphasize the importance of the burst size parameter $\tilde{b}$ in determining the viral spread c^* and, as a result, the plaque size. In Figure 5.9 (B), we determine the minimum wave speed values, denoted as c^*, by varying the binding rate γ_b and the burst size $\tilde{b}$. It is observed that for our range of possible burst sizes $\tilde{b} \in [500, 1000]$, the maximum wave speed c^* reaches 0.07154 when $\gamma_b = 0.5$ and $\tilde{b} = 1000$.

	γ_b	% **of Binding**	c^*	$\tilde{b}$	$\frac{\gamma_{\max}}{\tilde{b}}$
T3wt Data	0.96	61.7	0.04366	514	
Max T3wt	0.29	25.2	0.04858	514	0.00056
Intermediate Max	0.36	30.2	0.05460	623	0.00058
SV5 Data	0.28	24.4	0.05941	732	
Max SV5	0.42	34.3	0.06002	732	0.00057

Table 5.5: The infectious burst size, the binding rate, % of binding viruses and the corresponding wave speed for the wild type T3wt, intermediate infectious burst size, and SV5 virus.

$\tilde{b}$	$\gamma_{\max}$	$\frac{\gamma_{\max}}{\tilde{b}}$	$c^*_{\max}$	**Plaque Size**
virus per cell	per hour	cell per (virus × hour)	mm per hour	mm^2
500	0.28	0.00056	0.04775	5
550	0.32	0.00058	0.05065	20
600	0.36	0.00060	0.05338	32
650	0.36	0.00055	0.05600	43
700	0.39	0.00056	0.05848	55
750	0.43	0.00057	0.06090	69
800	0.47	0.00059	0.06316	82
850	0.47	0.00055	0.06538	95
900	0.51	0.00057	0.06753	106
950	0.51	0.00054	0.06959	121
1000	0.50	0.00050	0.07154	129

Table 5.6: The ratio of infectious burst size, the corresponding maximum binding rate, the maximum wave speed and the corresponding plaque size. The plaque size is computed with Model 3 as described in Section 5.7.

We observe that the ratio $\frac{\gamma_{\max}}{\tilde{b}}$ in Table 5.5 and Table 5.6 remains nearly constant for each maximum binding rate $\gamma_{\max}$ corresponding to the burst size $\tilde{b}$. Hence, we might use the ratio $\frac{\gamma_{\max}}{\tilde{b}}$ as a benchmark to assess how closely the experimental results approach the maximum required viral spread speed. The average number of ratio $\frac{\gamma_{\max}}{\tilde{b}}$ is 0.00056. Therefore, the optimal binding rate and burst size have a ratio of about

0.00056.

5.7 Model 3: Plaque Size

Results in Section 5.6 emphasize the importance of the burst size parameter $\tilde{b}$ in determining the viral spread c^* and, as a result, the plaque size. Motivated by these findings, this section embarks on an investigation into how variations in both the burst size $\tilde{b}$ and the binding rate γ_b parameters influence plaque size.

5.7.1 Plaque Size Experiments

In [53] an experiment is designed to measure the plaque size of the T3wt and SV5 viruses. They reported the relative areas $A_{\text{SV5}}/A_{\text{T3wt}}$ and found that the relative value of plaque size between SV5 and T3wt after 5 days varies between 3.4530 to 5.1248. This means that after 5 days, the plaque size of SV5 virus is about 4 times larger than the plaque size of the T3wt virus. We would like to point out the reason to measure the relative value of plaque size. It was observed that repeat experiments lead to different plaque sizes, due to variables that are out of control of the experimentalist such as cell viability, humidity, person performing the experiments, etc.. However, the relative plaque size difference of a factor of 4 were similar in all experiments. The reported values for $A_{\text{SV5}}/A_{\text{T3wt}}$ are

$$7.5575, 4.3643, 3.5976, 3.3551, 4.2194, 4.0628, 4.2596, 3.7092, 3.4748.$$

with mean and standard error

$$\frac{A_{\text{SV5}}}{A_{\text{T3wt}}} = 4.2889 \pm 0.8359,$$

which we like to confirm with our model.

To properly keep track of the plaque sizes, we now include the cancer cell compartment $C(x,t)$ explicitly. The plaques correspond to regions of dead cancer cells, and in our modelling we identify those as regions where $C(x,t)$ is below a small threshold.

Our previous model (5.9) is now extended to **Model 3:**

$$\begin{aligned}\frac{\partial C}{\partial t} &= -\gamma_b \nu C V,\\ \frac{\partial I}{\partial t} &= \gamma_b \nu C V - \alpha I,\\ \frac{\partial V}{\partial t} &= D_{\mathrm{v}} \frac{\partial^2 V}{\partial x^2} + \alpha \tilde{b} I - \gamma_b V,\end{aligned} \tag{5.21}$$

where all parameters have already been identified in Table 5.4.

We numerically solve our model (5.21) with virus inoculated in the center of a two-dimensional domain (see Figure 5.10). We estimate the plaque sizes after 5 days with threshold for cancer cells of 1%, indicated as a red line in the figures. We find a ratio $\frac{A_{\mathrm{SV5}}}{A_{\mathrm{T3wt}}} = \frac{55.4177}{15.2053} \approx 3.6$, which is very close to the experimental ratio mentioned above. We note that the T3wt and SV5 invasion forms a hollow ring spread pattern (see Figure 5.10). Such invasion patterns are typical for virus infections of tissues, and were also previously found in [81, 215].

Furthermore, we perform simulations of this model for a few chosen parameter values to see the dependence on γ_b and $\tilde{b}$. In Figure 5.11 and 5.12, we fix all parameters as in Table 5.4, while the burst size $\tilde{b}$ is varied as follows: 514 (T3wt), 623 (average), 732 (SV5), and 1000 (max). A notable increase in plaque size is observed for increased burst size.

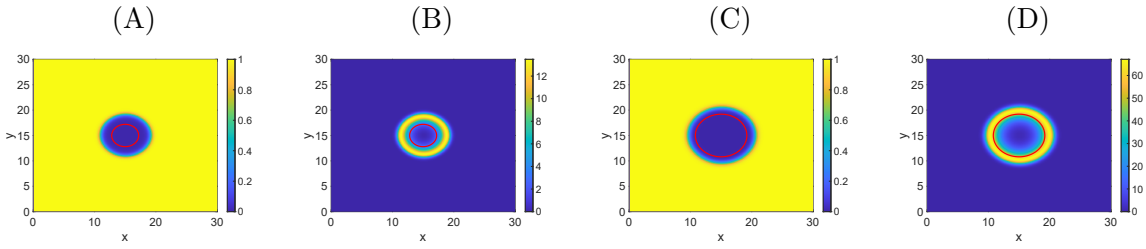

Figure 5.10: The plaque sizes at 5 days. **(A)+(B)**: T3wt spread with cancer cell density in (A) and viral concentration in (B). The C-level of 1% is indicated as a red line. **(C)+(D)**: SV5 infection with cancer cells in (C) and SV5 in (D). The computed plaque sizes are indicated in the red circle in (A) which is 15.2053 for T3wt virus and 55.4177 for SV5 virus in (C). Therefore, the relative plaque size of SV5 related to T3wt is 3.6446.

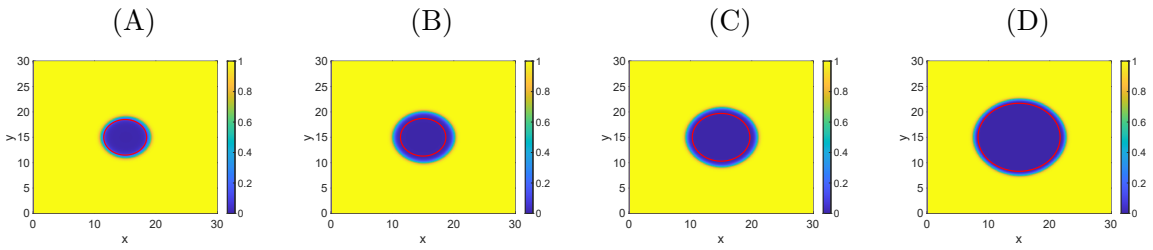

Figure 5.11: The plaque size of T3wt at t=5 days when $\gamma_b = 0.96$ with different burst size $\tilde{b}$. **(A)**: $\tilde{b} = 514$ **(B)**: $\tilde{b} = 623$ **(C)**: $\tilde{b} = 732$ and **(D)**: $\tilde{b} = 1000$. The threshold= 1 %.

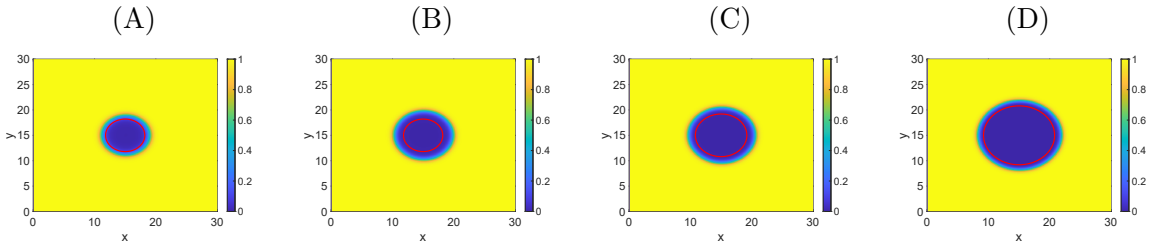

Figure 5.12: The plaque size of SV5 at t=5 days when $\gamma_b = 0.28$ with different burst size $\tilde{b}$. **(A)**: $\tilde{b} = 514$ **(B)**: $\tilde{b} = 623$ **(C)**: $\tilde{b} = 732$ and **(D)**: $\tilde{b} = 1000$. The threshold=1 %.

The paper [53] presents an additional dataset that we have not included here. These data pertain to plaque experiments conducted under the administration of the drug neuraminidase. Neuraminidase, known as a cancer chemotherapy agent, reduces the binding affinity of the virus. Our extended model (5.21) appears to offer the appropriate level of detail to simulate these experiments, and I am currently engaged in discussions with the Shmulevitz lab regarding the specifics of this modeling.

5.8 Conclusion

In this study, we employ a reaction-diffusion model to investigate key aspects of viral dynamics. Specifically, we explore the impact of the binding rate on virus spread, the correlation between viral invasion speed and binding rate, and the repercussions of reducing binding rate on plaque size. Two distinct time scales are considered: a short duration (less than 16 hours) focusing on viral spread preceding cell death and

replication events, and a longer time scale addressing viral infection between cells. All the parameters in our models are estimated using data from [53].

Our model establishes a connection between viral spread speed and binding rate, revealing the maximum viral spread aligns with a fine balance of viral binding. The binding has to be fast enough to allow for efficient cell infection, but it also has to be weak enough to allow the virus to spread throughout the medium. This result contradicts some common belief that increased binding rate leads to increased viral invasion. For the specific case of reovirus, our findings indicate that 25.9% binding after one hour is necessary for T3wt virus to achieve the maximum viral spread rate, whereas the SV5 virus requires approximately 34.3% binding after one hour.

Despite experimental results in [53] indicating no significant difference in burst size between T3wt and SV5 viruses, our numerical results present a contrasting perspective. The burst size parameter emerges as a critical determinant influencing viral spread, as an increase in burst size corresponds to heightened viral spread speed and, consequently, larger plaque sizes. This underscores the significance of the burst size parameter, as supported by various virotherapy references [88, 191]. Therefore, augmenting the burst size in conjunction with the optimal binding rate has the potential to yield substantial improvements in virotherapy outcomes. Additionally, our extended model results align with experimental data on relative plaque size and viral spread from the edge, reinforcing the robustness of our findings.

To sum up, the results of this study hold significant implications for advancing the development of anti-cancer viruses. The insights gained from this research are anticipated to play a pivotal role in shaping forthcoming strategies aimed at augmenting the therapeutic efficacy in the context of not only virotherapy but also viral infections in general.

Chapter 6

Conclusion and Future Work

The kingdom of viruses is expansive and diverse, encompassing a multitude of forms and structures, ranging from minuscule viruses to colossal mega-viruses. These entities play integral roles in the ecosystem, influencing the existence of every species on the planet. While capable of spreading contagion, viruses also possess the capacity to confer benefits essential to life itself [10, 55].

Oncolytic virotherapy represents a strategic endeavor to harness viral infections for our advantage. The concept involves infecting cancer cells with viruses, aiming either to directly eliminate them or to flag them for targeted immune responses. However, the path to developing effective oncolytic viruses is complex and convoluted. Numerous laboratories worldwide are immersed in fundamental research endeavors aimed at gaining a deeper understanding of the viral life cycle, encompassing processes such as binding, replication, cell lysis, and subsequent spread. It is within this realm of foundational research that I contribute, employing mathematical modeling techniques to shed light on crucial aspects of viral behavior and interaction with host cells.

In Chapter 2, a simple reaction-diffusion model is employed alongside homogenization techniques to assess whether the spatial distribution of host cells influences the effectiveness of viral infection. Through this approach, we not only validate the experimentally observed phenomenon but also establish a means to quantify the results using either arithmetic or geometric means.

Chapter 3 and 4 lead us to a detailed analysis of a prominent model within oncolytic virotherapy, extensively documented in numerous papers. Central to this model are oscillations induced by a Hopf bifurcation, which hold significant importance. Our exploration extends to understanding the spatial coupling of these oscillations, identifying precise conditions conducive to the formation of a hollow ring pattern—a pivotal configuration for effective tumor eradication. Furthermore, we establish the minimum wave speed required for the propagation of invading waves, considering both cancer cells and oncolytic viruses. Through 2-D numerical simulations, we uncover intricate spatial dynamics in virus infection, unveiling a novel phenomenon characterized by the periodic splitting of peaks in a mass-action scenario. Furthermore, the long time simulations uncovered highly complex spatio-temporal oscillations with potential relevance to a broad spectrum of virus infections, including COVID-19. Given that many COVID-19 patients experience long-lasting recurring effects [187, 188], it's plausible to speculate that sustained oscillations could contribute to such outcomes.

In Chapter 5, our focus centers on the examination of specific viruses, specifically the reovirus T3wt and SV5. We delve into understanding the influence of the binding rate on virus spread, the relationship between viral invasion speed and binding rate, and the consequences of reducing the binding rate on plaque size. We establish a direct link between the speed of viral spread and the binding rate, elucidating that the optimal viral spread occurs when there is a delicate equilibrium in viral binding. Our investigation into the reovirus reveals that for the T3wt virus, achieving a binding rate of 25.9% after one hour is imperative for attaining the maximum rate of viral spread, while the SV5 virus necessitates approximately 34.3% binding after the same duration. Moreover, despite the findings of the experiments in [53] indicating no substantial variance in burst size between T3wt and SV5 viruses, our numerical analysis presents a contrasting viewpoint. The burst size parameter emerges as a pivotal factor influencing viral spread, as an augmentation in burst size correlates with heightened viral spread speed and consequently, larger plaque sizes. This underscores

the significance of the burst size parameter, a notion reinforced by several references in virotherapy literature [88, 191]. Thus, enhancing the burst size alongside achieving the optimal binding rate holds promise for significantly enhancing virotherapy outcomes. Furthermore, our extended model's findings are consistent with experimental data on relative plaque size and viral spread from the edge, reinforcing the reliability and robustness of our conclusions.

It is very satisfying to witness how simple mathematical models can significantly enhance our comprehension of oncolytic virotherapy. Through our modeling efforts, we have pinpointed optimal binding conditions that enable reovirus to achieve maximum spatial spread. Moreover, we have demonstrated that the collective behavior of cells in a homogeneous mixture may not simply be the sum of their individual contributions, particularly when considering virus-host oscillations, which can be advantageous to patients, particularly in scenarios involving hollow-ring dynamics.

Of course, these models can be expanded to incorporate additional factors, with the foremost being the immune response. Now that we have characterized all parameters governing viral dynamics, the logical progression is to integrate immune responses. I aspire to further this research in my future endeavors in cancer research.

Bibliography

[1] H. Sung, J. Ferlay, R. L. Siegel, M. Laversanne, I. Soerjomataram, A. Jemal, and F. Bray. Global cancer statistics 2020: globocan estimates of incidence and mortality worldwide for 36 cancers in 185 countries. *CA: A Cancer Journal for Clinicians*, 71(3):209–249, 2021.

[2] G. Cooper and K. Adams. *The cell: a molecular approach*. Oxford University Press, 2022.

[3] C. A. Perez, S. Vijayakumar, S Levitt, and J. A. Purdy. *Technical Basis of Radiation Therapy Practical Clinical Applications*. Springer, 2012.

[4] N. André, M. Carré, and E. Pasquier. Metronomics: towards personalized chemotherapy? *Nature Reviews Clinical Oncology*, 11(7):413–431, 2014.

[5] W. J. Curran, C. B. Scott, J. Horton, J. S. Nelson, A. S. Weinstein, D. F. Nelson, A. J. Fischbach, C. H. Chang, M. Rotman, S. O. Asbell, et al. Does extent of surgery influence outcome for astrocytoma with atypical or anaplastic foci (aaf)? a report from three radiation therapy oncology group (rtog) trials. *Journal of Neuro-Oncology*, 12(3):219–227, 1992.

[6] A. Grzelak, I. Polakova, J. Smahelova, J. Vackova, L. Pekarcikova, R. Tachezy, and M. Smahel. Experimental combined immunotherapy of tumours with major histocompatibility complex class I downregulation. *International Journal of Molecular Sciences*, 19(11):3693, 2018.

[7] S. J. Russell, K.-W. Peng, and J. C. Bell. Oncolytic virotherapy. *Nature Biotechnology*, 30(7):658–670, 2012.

[8] C. Fountzilas, S. Patel, and D. Mahalingam. Oncolytic virotherapy, updates and future directions. *Oncotarget*, 8(60):102617, 2017.

[9] K. Harrington, D. J. Freeman, B. Kelly, J. Harper, and J.-C. Soria. Optimizing oncolytic virotherapy in cancer treatment. *Nature Reviews Drug Discovery*, 18(9):689–706, 2019.

[10] L. Li, S. Liu, D. Han, B. Tang, and J. Ma. Delivery and Biosafety of Oncolytic Virotherapy. *Frontiers in Oncology*, 10:475, 2020.

[11] A Tsun, X. Miao, C. Wang, and D. Yu. Oncolytic immunotherapy for treatment of cancer. *Progress in Cancer Immunotherapy*:241–283, 2016.

[12] G. R. Simpson, K. Relph, K. Harrington, A. Melcher, and H. Pandha. Cancer immunotherapy via combining oncolytic virotherapy with chemotherapy: recent advances. *Oncolytic Virotherapy*, 5:1, 2016.

[13] Y. Touchefeu, G. Vassaux, and K. J. Harrington. Oncolytic viruses in radiation oncology. *Radiotherapy and Oncology*, 99(3):262–270, 2011.

[14] K. J. Harrington, E. M. Karapanagiotou, V. Roulstone, K. R. Twigger, C. L. White, L. Vidal, D. Beirne, R. Prestwich, K. Newbold, M. Ahmed, et al. Two-stage phase I dose-escalation study of intratumoral reovirus type 3 dearing and palliative radiotherapy in patients with advanced cancers. *Clinical Cancer Research*, 16(11):3067–3077, 2010.

[15] G. Belostotski. *A control theory model for cancer treatment by radiotherapy*, University of Alberta, 2005.

[16] S. O'Rourke, H. McAneney, and T. Hillen. Linear quadratic and tumour control probability modelling in external beam radiotherapy. *Journal of Mathematical Biology*, 58(4):799–817, 2009.

[17] Z. Liu and C. Yang. A mathematical model of cancer treatment by radiotherapy. *Computational and Mathematical Methods in Medicine*, 2014, 2014.

[18] L. Bodgi, A. Canet, L. Pujo-Menjouet, A. Lesne, J.-M. Victor, and N. Foray. Mathematical models of radiation action on living cells: from the target theory to the modern approaches. a historical and critical review. *Journal of Theoretical Biology*, 394:93–101, 2016.

[19] J. Usher. Some mathematical models for cancer chemotherapy. *Computers & Mathematics with Applications*, 28(9):73–80, 1994.

[20] U. Ledzewicz, B. Amini, and H. Schättler. Dynamics and control of a mathematical model for metronomic chemotherapy. *Mathematical Biosciences and Engineering*, 12(6):1257–1275, 2015.

[21] G Powathil, M Kohandel, S Sivaloganathan, A Oza, and M Milosevic. Mathematical modeling of brain tumors: effects of radiotherapy and chemotherapy. *Physics in Medicine & Biology*, 52(11):3291, 2007.

[22] M Kohandel, S Sivaloganathan, and A Oza. Mathematical modeling of ovarian cancer treatments: sequencing of surgery and chemotherapy. *Journal of Theoretical Biology*, 242(1):62–68, 2006.

[23] L. Pang, L. Shen, and Z. Zhao. Mathematical modelling and analysis of the tumor treatment regimens with pulsed immunotherapy and chemotherapy. *Computational and Mathematical Methods in Medicine*, 2016, 2016.

[24] R. Serre, S. Benzekry, L. Padovani, C. Meille, N. André, J. Ciccolini, F. Barlesi, X. Muracciole, and D. Barbolosi. Mathematical modeling of cancer immunotherapy and its synergy with radiotherapy. *Cancer Research*, 76(17):4931–4940, 2016.

[25] H.-C. Wei and J.-T. Lin. Periodically pulsed immunotherapy in a mathematical model of tumor-immune interaction. *International Journal of Bifurcation and Chaos*, 23(04):1350068, 2013.

[26] A. Konstorum, A. T. Vella, A. J. Adler, and R. C. Laubenbacher. Addressing current challenges in cancer immunotherapy with mathematical and computational modelling. *Journal of The Royal Society Interface*, 14(131):20170150, 2017.

[27] D. Dingli, M. D. Cascino, K. Josić, S. J. Russell, and Ž. Bajzer. Mathematical modeling of cancer radiovirotherapy. *Mathematical Biosciences*, 199(1):55–78, 2006.

[28] E. Domingo, C. R. Parrish, and J. J. Holland. *Origin and evolution of viruses*. Elsevier, 2008.

[29] M. G. Mateu. Structure and physics of viruses. *Thematic Issue of Subcell*:12, 2013.

[30] M. J. Roossinck. *Viruses: A Natural History*, volume 5. Princeton University Press, 2023.

[31] A. Cann. Replication of viruses. *Encyclopedia of Virology*:406, 2008.

[32] J. Louten. *Essential Human Virology*. Elsevier, 2017.

[33] W.-S. Ryu. *Molecular Virology of Human Pathogenic Viruses*. Elsevier, 2017.

[34] Y. Miyah, M. Benjelloun, S. Lairini, A. Lahrichi, et al. Covid-19 impact on public health, environment, human psychology, global socioeconomy, and education. *The Scientific World Journal*, 2022, 2022.

[35] E. Kelly and S. J. Russell. History of oncolytic viruses: genesis to genetic engineering. *Molecular Therapy*, 15(4):651–659, 2007.

[36] C. E. Engeland and J. C. Bell. *Introduction to Oncolytic Virotherapy*. Springer New York, 2020.

[37] D. N. Santiago, J. P. Heidbuechel, W. M. Kandell, R. Walker, J. Djeu, C. E. Engeland, D. Abate-Daga, and H. Enderling. Fighting cancer with mathematics and viruses. *Viruses*, 9(9):239, 2017.

[38] S. Chaurasiya, Y. Fong, and S. G. Warner. Oncolytic virotherapy for cancer: clinical experience. *Biomedicines*, 9(4):419, 2021.

[39] G. Motalleb. Virotherapy in cancer. *Iranian Journal of Cancer Prevention*, 6(2):101, 2013.

[40] I. Ganly, D. Kirn, S. Eckhardt, G. Rodriguez, D. Soutar, R. Otto, A. Robertson, O. Park, M. Gulley, C. Heise, et al. A phase I study of onyx-015, an e1b attenuated adenovirus, administered intratumorally to patients with recurrent head and neck cancer. *Clinical Cancer Research*, 6(3):798–806, 2000.

[41] J.-H. Kim, Y.-S. Lee, H. Kim, J.-H. Huang, A.-R. Yoon, and C.-O. Yun. Relaxin expression from tumor-targeting adenoviruses and its intratumoral spread, apoptosis induction, and efficacy. *Journal of the National Cancer Institute*, 98(20):1482–1493, 2006.

[42] M. Garcia, R. Moreno, M. Gil-Martin, M. Cascallo, M. de Olza, C. Cuadra, J. Piulats, V. Navarro, M. Domenech, R. Alemany, et al. A phase 1 trial of oncolytic adenovirus icovir-5 administered intravenously to cutaneous and uveal melanoma patients. *Human Gene Therapy*, 30(3):352–364, 2019.

[43] D. Makower, A. Rozenblit, H. Kaufman, M. Edelman, M. Lane, J. Zwiebel, H. Haynes, and S. Wadler. Phase II clinical trial of intralesional administration of the oncolytic adenovirus onyx-015 in patients with hepatobiliary tumors with correlative p53 studies. *Clinical Cancer Research*, 9(2):693–702, 2003.

[44] D. Sanchala, L. Bhatt, and K. Prabhavalkar. Oncolytic herpes simplex viral therapy: a stride toward selective targeting of cancer cells. *Frontiers in Pharmacology*, 8:270, 2017.

[45] N. Sokolowski, H. Rizos, and R. Diefenbach. Oncolytic virotherapy using herpes simplex virus: how far have we come? *Oncolytic Virotherapy*, 4:207, 2015.

[46] S. H. Thorne. Next-generation oncolytic vaccinia vectors. In *Oncolytic Viruses*, pages 205–215. Springer, 2012.

[47] S. Bhattacharjee and P. Yadava. Measles virus: background and oncolytic virotherapy. *Biochemistry and Biophysics Reports*, 13:58–62, 2018.

[48] L. Vidal, H. S. Pandha, T. A. Yap, C. L. White, K. Twigger, R. G. Vile, A. Melcher, M. Coffey, K. J. Harrington, and J. S. DeBono. A phase I study of intravenous oncolytic reovirus type 3 dearing in patients with advanced cancer. *Clinical Cancer Research*, 14(21):7127–7137, 2008.

[49] L. Müller, R. Berkeley, T. Barr, E. Ilett, and F. Errington-Mais. Past, present and future of oncolytic reovirus. *Cancers*, 12(11):3219, 2020.

[50] J. Gong, E. Sachdev, A. C. Mita, and M. M. Mita. Clinical development of reovirus for cancer therapy: an oncolytic virus with immune-mediated antitumor activity. *World Journal of Methodology*, 6(1):25, 2016.

[51] A. Mohamed, R. N. Johnston, and M. Shmulevitz. Potential for improving potency and specificity of reovirus oncolysis with next-generation reovirus variants. *Viruses*, 7(12):6251–6278, 2015.

[52] F. Cristi, T. Gutiérrez, M. M. Hitt, and M. Shmulevitz. Genetic modifications that expand oncolytic virus potency. *Frontiers in Molecular Biosciences*, 9:831091, 2022.

[53] F. Cristi, M. Walters, N. Narayan, K. Agopsowicz, M. M. Hitt, and M. Shmulevitz. Improved oncolytic activity of a reovirus mutant that displays enhanced virus spread due to reduced cell attachment. *Molecular Therapy Oncolytics*, 31, 2023.

[54] E. Hastie and V. Z. Grdzelishvili. Vesicular stomatitis virus as a flexible platform for oncolytic virotherapy against cancer. *The Journal of General Virology*, 93(Pt 12):2529, 2012.

[55] P. Gao, G. Ding, and L. Wang. The efficacy and safety of oncolytic viruses in the treatment of intermediate to advanced solid tumors: a systematic review and meta-analysis. *Translational Cancer Research*, 10(10):4290, 2021.

[56] K. Garber. China approves world's first oncolytic virus therapy for cancer treatment. *Journal of the National Cancer Institute*, 98(5):298–300, 2006.

[57] S. L. Greig. Talimogene laherparepvec: first global approval. *Drugs*, 76(1):147–154, 2016.

[58] K.-T. Jin, W.-L. Du, Y.-Y. Liu, H.-R. Lan, J.-X. Si, and X.-Z. Mou. Oncolytic virotherapy in solid tumors: the challenges and achievements. *Cancers*, 13(4):588, 2021.

[59] J. Wojton and B. Kaur. Impact of tumor microenvironment on oncolytic viral therapy. *Cytokine & Growth Factor Reviews*, 21(2-3):127–134, 2010.

[60] A. L. Jenner, C.-O. Yun, P. S. Kim, and A. C. Coster. Mathematical modelling of the interaction between cancer cells and an oncolytic virus: insights into the effects of treatment protocols. *Bulletin of Mathematical Biology*, 80(6):1615–1629, 2018.

[61] Ž. Bajzer, T. Carr, K. Josić, S. J. Russell, and D. Dingli. Modeling of cancer virotherapy with recombinant measles viruses. *Journal of Theoretical Biology*, 252(1):109–122, 2008.

[62] R. Eftimie, C. K. Macnamara, J. Dushoff, J. L. Bramson, and D. J. Earn. Bifurcations and chaotic dynamics in a tumour-immune-virus system. *Mathematical Modelling of Natural Phenomena*, 11(5):65–85, 2016.

[63] I. A. Rodriguez-Brenes, A. Hofacre, H. Fan, and D. Wodarz. Complex dynamics of virus spread from low infection multiplicities: implications for the spread of oncolytic viruses. *PLoS Computational Biology*, 13(1):e1005241, 2017.

[64] R. Eftimie and G. Eftimie. Investigating macrophages plasticity following tumour–immune interactions during oncolytic therapies. *Acta Biotheoretica*, 67(4):321–359, 2019.

[65] K. W. Okamoto, P. Amarasekare, and I. T. Petty. Modeling oncolytic virotherapy: is complete tumor-tropism too much of a good thing? *Journal of Theoretical Biology*, 358:166–178, 2014.

[66] J. P. Tian. The replicability of oncolytic virus: defining conditions in tumor virotherapy. *Mathematical Biosciences & Engineering*, 8(3):841, 2011.

[67] A. L. Jenner, P. S. Kim, and F. Frascoli. Oncolytic virotherapy for tumours following a gompertz growth law. *Journal of Theoretical Biology*, 480:129–140, 2019.

[68] K. M. Storey, S. E. Lawler, and T. L. Jackson. Modeling oncolytic viral therapy, immune checkpoint inhibition, and the complex dynamics of innate and adaptive immunity in glioblastoma treatment. *Frontiers in Physiology*, 11:151, 2020.

[69] J. J. Crivelli, J. Földes, P. S. Kim, and J. R. Wares. A mathematical model for cell cycle-specific cancer virotherapy. *Journal of Biological Dynamics*, 6(sup1):104–120, 2012.

[70] V. de Rioja, N. Isern, and J. Fort. A mathematical approach to virus therapy of glioblastomas. *Biology Direct*, 11(1):1–12, 2016.

[71] Y. Wang, J. P. Tian, and J. Wei. Lytic cycle: a defining process in oncolytic virotherapy. *Applied Mathematical Modelling*, 37(8):5962–5978, 2013.

[72] K. J. Mahasa, A. Eladdadi, L. De Pillis, and R. Ouifki. Oncolytic potency and reduced virus tumor-specificity in oncolytic virotherapy. a mathematical modelling approach. *Plos One*, 12(9):e0184347, 2017.

[73] Z. Wang, Z. Guo, and H. Smith. A mathematical model of oncolytic virotherapy with time delay. *Mathematical Biosciences and Engineering*, 16(4):1836–1860, 2019.

[74] L. R. Paiva, C. Binny, S. C. Ferreira Jr, and M. L. Martins. A multiscale mathematical model for oncolytic virotherapy. *Cancer Research*, 69(3):1205–1211, 2009.

[75] T. Alzahrani, R. Eftimie, and D. Trucu. Multiscale modelling of cancer response to oncolytic viral therapy. *Mathematical Biosciences*, 310:76–95, 2019.

[76] C. L. Reis, J. M. Pacheco, M. K. Ennis, and D. Dingli. In silico evolutionary dynamics of tumour virotherapy. *Integrative Biology*, 2(1):41–45, 2010.

[77] T. A. Phan and J. P. Tian. Basic stochastic model for tumor virotherapy. *Mathematical Biosciences and Engineering: MBE*, 17(4):4271, 2020.

[78] A. Raza, J. Awrejcewicz, M. Rafiq, N. Ahmed, and M. Mohsin. Stochastic analysis of nonlinear cancer disease model through virotherapy and computational methods. *Mathematics*, 10(3):368, 2022.

[79] I. Kemler, M. K. Ennis, C. M. Neuhauser, and D. Dingli. In vivo imaging of oncolytic measles virus propagation with single-cell resolution. *Molecular Therapy-Oncolytics*, 12:68–78, 2019.

[80] A. Swick, A. Baltes, and J. Yin. Visualizing infection spread: dual-color fluorescent reporting of virus–host interactions. *Biotechnology and Bioengineering*, 111(6):1200–1209, 2014.

[81] D. Wodarz, A. Hofacre, J. Lau, Z. Sun, H. Fan, and N. Komarova. Complex spatial dynamics of oncolytic viruses in vitro: mathematical and experimental approaches. *PLoS Computational Biology*, 8(6):e1002547, 2012.

[82] A. Friedman, J. P. Tian, G. Fulci, E. A. Chiocca, and J. Wang. Glioma virotherapy: effects of innate immune suppression and increased viral replication capacity. *Cancer Research*, 66(4):2314–2319, 2006.

[83] J. T. Wu, H. M. Byrne, D. H. Kirn, and L. M. Wein. Modeling and analysis of a virus that replicates selectively in tumor cells. *Bulletin of Mathematical Biology*, 63:731–768, 2001.

[84] J. T. Wu, D. H. Kirn, and L. M. Wein. Analysis of a three-way race between tumor growth, a replication-competent virus and an immune response. *Bulletin of Mathematical Biology*, 66:605–625, 2004.

[85] B. I. Camara, H. Mokrani, and E. K. Afenya. Mathematical modeling of glioma therapy using oncolytic viruses. *Mathematical Biosciences & Engineering*, 10(3):565, 2013.

[86] A. M. Elaiw, A. Hobiny, and A. Al Agha. Global dynamics of reaction-diffusion oncolytic m1 virotherapy with immune response. *Applied Mathematics and Computation*, 367:124758, 2020.

[87] N. Al-Johani, E. Simbawa, and S. Al-Tuwairqi. Modeling the spatiotemporal dynamics of virotherapy and immune response as a treatment for cancer. *Communications in Mathematical Biology and Neuroscience*, 2019:Article–ID, 2019.

[88] P. Pooladvand, C. Yun, A. Yoon, P. Kim, and F. Frascoli. The role of viral infectivity in oncolytic virotherapy outcomes: a mathematical study. *Mathematical Biosciences*, 334:108520, 2021.

[89] J. Malinzi, P. Sibanda, and H. Mambili-Mamboundou. Analysis of virotherapy in solid tumor invasion. *Mathematical Biosciences*, 263:102–110, 2015.

[90] J. Malinzi. A mathematical model for oncolytic virus spread using the telegraph equation. *Communications in Nonlinear Science and Numerical Simulation*, 102:105944, 2021.

[91] D. Morselli, M. E. Delitala, and F. Frascoli. Agent-based and continuum models for spatial dynamics of infection by oncolytic viruses. *Bulletin of Mathematical Biology*, 85(10):92, 2023.

[92] K. M. Storey and T. L. Jackson. An agent-based model of combination oncolytic viral therapy and anti-pd-1 immunotherapy reveals the importance of spatial location when treating glioblastoma. *Cancers*, 13(21):5314, 2021.

[93] D. Wodarz. Viruses as antitumor weapons: defining conditions for tumor remission. *Cancer Research*, 61:3501–3507, 2001.

[94] J. Wang and J. Tian. Numerical study for a model of tumor virotherapy. *Applied Mathematics and Computation*, 196(1):448–457, 2008.

[95] D. Wodarz and N. Komarova. Towards predictive computational models of oncolytic virus therapy: basis for experimental validation and model selection. *PLOS ONE*, 4(1):e4271, 2009.

[96] J. Zhao and J. P. Tian. Spatial model for oncolytic virotherapy with lytic cycle delay. *Bulletin of Mathematical Biology*, 81(7):2396–2427, 2019.

[97] D. K. Bhatt, T. Janzen, T. Daemen, and F. J. Weissing. Modelling the spatial dynamics of oncolytic virotherapy in the presence of virus-resistant tumour cells. *PLOS Computational Biology*, 18(12):e1010076, 2022.

[98] Y. Kim, H. G. Lee, N. Dmitrieva, J. Kim, B. Kaur, and A. Friedman. Choindroitinase abc i-mediated enhancement of oncolytic virus spread and anti tumor efficacy: a mathematical model. *PLOS ONE*, 9(7):e102499, 2014.

[99] D. Wodarz. Gene therapy for killing p53-negative cancer cells: use of replicating versus nonreplicating agents. *Human Gene Therapy*, 14(2):153–159, 2003.

[100] B. W. Bridle, K. B. Stephenson, J. E. Boudreau, S. Koshy, N. Kazdhan, E. Pullenayegum, J. Brunellière, J. L. Bramson, B. D. Lichty, and Y. Wan. Potentiating cancer immunotherapy using an oncolytic virus. *Molecular Therapy*, 18(8):1430–1439, 2010.

[101] C. J. Breitbach, J. M. Paterson, C. G. Lemay, T. J. Falls, A. McGuire, K. A. Parato, D. F. Stojdl, M. Daneshmand, K. Speth, D. Kirn, et al. Targeted inflammation during oncolytic virus therapy severely compromises tumor blood flow. *Molecular Therapy*, 15(9):1686–1693, 2007.

[102] R. Alemany, K. Suzuki, and D. T. Curiel. Blood clearance rates of adenovirus type 5 in mice. *Journal of General Virology*, 81(11):2605–2609, 2000.

[103] R. Eftimie, J. Dushoff, B. W. Bridle, J. L. Bramson, and D. J. Earn. Multistability and multi-instability phenomena in a mathematical model of tumor-immune-virus interactions. *Bulletin of Mathematical Biology*, 73:2932–2961, 2011.

[104] J. W. A. Timalsina JP. Tian. Mathematical and computational modelling for tumor virotherapy with mediated immunity. *Bulletin of Mathematical Biology*, 79:1736–1758, 2017.

[105] Y. Yuan. Spatial heterogeneity in the tumor microenvironment. *Cold Spring Harbor Perspectives in Medicine*, 6(8), 2016.

[106] J. D. Murray. *Mathematical biology: II: spatial models and biomedical applications*, volume 18. Springer, 2003.

[107] N. F. Britton. *Reaction-diffusion equations and their applications to biology*. Academic Press, 1986.

[108] G. De Vries, T. Hillen, M. Lewis, J. Müller, and B. Schönfisch. *A course in mathematical biology: quantitative modeling with mathematical and computational methods*. SIAM, 2006.

[109] G. Pavliotis and A. Stuart. *Multiscale methods: averaging and homogenization*. Springer Science & Business Media, 2008.

[110] L. Perko. *Differential equations and dynamical systems*, volume 7. Springer Science & Business Media, 2013.

[111] R. A. Fisher. The wave of advance of advantageous genes. *Annals of Eugenics*, 7(4):355–369, 1937.

[112] A. N. Kolmogorov, I. G. Petrovskii, and N. S. Piskunov. A study of the diffusion equation with increase in the amount of substance, and its application to a biological problem. *Bull. Moscow Univ., Math. Mech.*, 1:6:1–26, 1937.

[113] J. G. Skellam. Random dispersal in theoretical populations. *Biometrika*, 38(1/2):196–218, 1951.

[114] A. M. Turing. The chemical basis of morphogenesis. *Bulletin of Mathematical Biology*, 52:153–197, 1990.

[115] N. V. Swindale. A model for the formation of ocular dominance stripes. *Proceedings of the Royal Society of London. Series B. Biological Sciences*, 208(1171):243–264, 1980.

[116] J. D. Murray. On pattern formation mechanisms for lepidopteran wing patterns and mammalian coat markings. *Philosophical Transactions of the Royal Society of London. B, Biological Sciences*, 295(1078):473–496, 1981.

[117] D. G. Kendall. Mathematical models of the spread of infection. *Mathematics and Computer Science in Biology and Medicine*:213–225, 1965.

[118] D Ludwig, D. Aronson, and H. Weinberger. Spatial patterning of the spruce budworm. *Journal of Mathematical Biology*, 8(3):217–258, 1979.

[119] H. Kierstead and L Slobodkin. The size of water masses containing plankton blooms. *Journal of Marine Research*, 12:141–147, 1953.

[120] D. Alonso, F. Bartumeus, and J. Catalan. Mutual interference between predators can give rise to turing spatial patterns. *Ecology*, 83(1):28–34, 2002.

[121] S. Aly, I. Kim, and D. Sheen. Turing instability for a ratio-dependent predator–prey model with diffusion. *Applied Mathematics and Computation*, 217(17):7265–7281, 2011.

[122] L. Li and Z. Jin. Pattern dynamics of a spatial predator–prey model with noise. *Nonlinear Dynamics*, 67:1737–1744, 2012.

[123] R. S. Cantrell and C. Cosner. *Spatial ecology via reaction-diffusion equations*. John Wiley & Sons, 2004.

[124] P. K. Maini and H. G. Othmer. *Mathematical models for biological pattern formation*. Springer, 2001.

[125] J. Keener and J. Sneyd. *Mathematical physiology*. Springer, 1998.

[126] A. Panfilov and P. Hogeweg. Spiral breakup in a modified fitzhugh-nagumo model. *Physics Letters A*, 176(5):295–299, 1993.

[127] Q. Zheng and J. Shen. Pattern formation in the fitzhugh–nagumo model. *Computers & Mathematics with Applications*, 70(5):1082–1097, 2015.

[128] A. Turner. *A simple model of the Belousov-Zhabotinsky reaction from first principles*, Bartlett School of Graduate Studies, UCL, 2009.

[129] J. E. Pearson. Complex patterns in a simple system. *Science*, 261(5118):189–192, 1993.

[130] E. Körös. *Oscillations, waves, and spirals in chemical systems*. World Scientific, Singapore, 1992.

[131] J. Rinzel and J. B. Keller. Traveling wave solutions of a nerve conduction equation. *Biophysical Journal*, 13(12):1313–1337, 1973.

[132] S. Hastings. On the existence of homoclinic and periodic orbits for the fitzhugh-nagumo equations. *The Quarterly Journal of Mathematics*, 27(1):123–134, 1976.

[133] M. A. Lewis and P Kareiva. Allee dynamics and the spread of invading organisms. *Theoretical Population Biology*, 43(2):141–158, 1993.

[134] M. A. Lewis, B. Li, and H. F. Weinberger. Spreading speed and linear determinacy for two-species competition models. *Journal of Mathematical Biology*, 45:219–233, 2002.

[135] M. Kamiński. Homogenization of transient heat transfer problems for some composite materials. *International Journal of Engineering Science*, 41(1):1–29, 2003.

[136] J. A. Powell and N. E. Zimmermann. Multiscale analysis of active seed dispersal contributes to resolving reid's paradox. *Ecology*, 85(2):490–506, 2004.

[137] W. E. Fitzgibbon, M. Langlais, and J. J. Morgan. A mathematical model of the spread of feline leukemia virus (felv) through a highly heterogeneous spatial domain. *SIAM Journal on Mathematical Analysis*, 33(3):570–588, 2001.

[138] S. Dewhirst and F. Lutscher. Dispersal in heterogeneous habitats: thresholds, spatial scales, and approximate rates of spread. *Ecology*, 90(5):1338–1345, 2009.

[139] M. J. Garlick, J. A. Powell, M. B. Hooten, and L. R. MacFarlane. Homogenization, sex, and differential motility predict spread of chronic wasting disease in mule deer in southern utah. *Journal of Mathematical Biology*, 69:369–399, 2014.

[140] M. H. Holmes. *Introduction to perturbation methods*, volume 20. Springer Science & Business Media, 2012.

[141] Y. M. Shabana and N. Noda. Numerical evaluation of the thermomechanical effective properties of a functionally graded material using the homogenization method. *International Journal of Solids and Structures*, 45(11-12):3494–3506, 2008.

[142] W. Liu. Criterion of Hopf bifurcations without using eigenvalues. *Journal of Mathematical Analysis and Applications*, 182(1):250–256, 1994.

[143] S. Jahedi, L. Wang, and J. Watmough. Fighting cancer with oncolytic viral therapy: identifying threshold parameters for success. *bioRxiv*, 2021.

[144] J. Gong, M. M. Dos Santos, C. Finlay, and T. Hillen. Are more complicated tumour control probability models better? *Mathematical Medicine and Biology: a Journal of the IMA*, 30(1):1–19, 2013.

[145] J. Medhi. *Stochastic processes*. New Age International, 1994.

[146] A. Smith and A. Perelson. Influenza A virus infection kinetics: quantitative data and models. *WIREs Syst. Biol. Med.*, 3:429–445, 2011.

[147] C. Beauchemin and A. Handel. A review of mathematical models of influenza A infections within a host or cell culture: lessons learned and challenges ahead. *BMC Public Health*, 11:S7, 2011.

[148] M. Gallagher, C. Brooke, R. Ke, and K. Koelle. Causes and consequences of spatial within-host viral spread. *Viruses*, 10:627–650, 2018.

[149] A. Smith. Host-pathogen kinetics during influenza infection and coinfection: insights from predictive modeling. *Immunological Reviews*, 285:97–112, 2018.

[150] B. Snijder, R. Sacher, P. Rämö, E.-M. Damm, P. Liberali, and L. Pelkmans. Population context determines cell-to-cell variability in endocytosis and virus infection. *Nature*, 461(7263):520–523, 2009.

[151] J. A. Park, S. Yoon, J. Kwon, Y. K. Kim, W. J. Kim, J. Y. Yoo, and S. Jung. Freeform micropatterning of living cells into cell culture medium using direct inkjet printing. *Scientific Reports*, 7(1):1–11, 2017.

[152] I. Li, K. Chan, K. To, S. Wong, P. Ho, S. Lau, P. Woo, H. Tsoi, J. Chan, V. Cheng, et al. Differential susceptibility of different cell lines to swine-origin influenza A H1N1, seasonal human influenza A H1N1, and avian influenza A H5N1 viruses. *Journal of Clinical Virology*, 46(4):325–330, 2009.

[153] E. De Vries, D. M. Tscherne, M. J. Wienholts, V. Cobos-Jimenez, F. Scholte, A. Garcia-Sastre, P. J. Rottier, and C. A. De Haan. Dissection of the influenza A virus endocytic routes reveals macropinocytosis as an alternative entry pathway. *PLoS Pathogens*, 7(3):e1001329, 2011.

[154] H. Now and J.-Y. Yoo. Ag490 and pf431396 sensitive tyrosine kinase control the population heterogeneity of basal stat1 activity in ube1l deficient cells. *PloS One*, 11(7):e0159453, 2016.

[155] N. Shigesada, K. Kawasaki, and E. Teramoto. Traveling periodic waves in heterogeneous environments. *Theoretical Population Biology*, 30(1):143–160, 1986.

[156] N. Shigesada, K. Kawasaki, and H. F. Weinberger. Spreading speeds of invasive species in a periodic patchy environment: effects of dispersal based on local information and gradient-based taxis. *Japan Journal of Industrial and Applied Mathematics*, 32(3):675–705, 2015.

[157] G. A. Maciel and F. Lutscher. How individual movement response to habitat edges affects population persistence and spatial spread. *The American Naturalist*, 182(1):42–52, 2013.

[158] G. A. Maciel and F. Lutscher. Allee effects and population spread in patchy landscapes. *Journal of Biological Dynamics*, 9(1):109–123, 2015.

[159] B. P. Yurk. Homogenization analysis of invasion dynamics in heterogeneous landscapes with differential bias and motility. *Journal of Mathematical Biology*, 77(1):27–54, 2018.

[160] B. P. Yurk and C. A. Cobbold. Homogenization techniques for population dynamics in strongly heterogeneous landscapes. *Journal of Biological Dynamics*, 12(1):171–193, 2018.

[161] A. G. Murray and G. A. Jackson. Viral dynamics: a model of the effects of size, shape, motion and abundance of single-celled planktonic organisms and other particles, 1992.

[162] E. Fröhlich, G. Bonstingl, A. Höfler, C. Meindl, G. Leitinger, T. R. Pieber, and E. Roblegg. Comparison of two in vitro systems to assess cellular effects of nanoparticles-containing aerosols. *Toxicology in Vitro*, 27(1):409–417, 2013.

[163] W.-P. Breugem. The effective viscosity of a channel-type porous medium. *Physics of Fluids*, 19(10):103104, 2007.

[164] A. Boianelli, V. K. Nguyen, T. Ebensen, K. Schulze, E. Wilk, N. Sharma, S. Stegemann-Koniszewski, D. Bruder, F. R. Toapanta, C. A. Guzmán, et al. Modeling influenza virus infection: a roadmap for influenza research. *Viruses*, 7(10):5274–5304, 2015.

[165] G. D Smith. *Numerical Solution Of Partial Differential Equations: Finite Difference Methods*. Oxford University Press, 3rd edition, 1985.

[166] N. Néant, G. Lingas, Q. Le Hingrat, J. Ghosn, I. Engelmann, Q. Lepiller, A. Gaymard, V. Ferré, C. Hartard, J.-C. Plantier, et al. Modeling sars-cov-2 viral kinetics and association with mortality in hospitalized patients from the french covid cohort. *Proceedings of the National Academy of Sciences*, 118(8):e2017962118, 2021.

[167] M. Getz, Y. Wang, G. An, A. Becker, C. Cockrell, N. Collier, M. Craig, C. Davis, J. Faeder, A. Versypt, J. Gianlupi, J. Glazier, S. Hamis, R. Heiland, T. Hillen, D. Hou, M. A. Islam, A. Jenner, F. Kurtoglu, B. Liu, F. Macfarlane, P. Maygrundter, P. Morel, A. Narayanan, J. Ozik, E. Pienaar, P. Rangamani, J. E. Shoemaker, A. Smith, and P. Macklin. Rapid community-driven development of a sars-cov-2 tissue simulator. 2020.

[168] K. L. Roberts, B. Manicassamy, and R. A. Lamb. Influenza A virus uses intercellular connections to spread to neighboring cells. *Journal of Virology*, 89(3):1537–1549, 2015.

[169] O. Diekmann, J. Heesterbeek, and M. G. Roberts. The construction of next-generation matrices for compartmental epidemic models. *Journal of the Royal Society Interface*, 7(47):873–885, 2010.

[170] H. F. Lodish. *Molecular cell biology*. Macmillan, 2008.

[171] I. Ganly, V. Mautner, and A. Balmain. Productive replication of human adenoviruses in mouse epidermal cells. *Journal of Virology*, 74(6):2895–2899, 2000.

[172] W. Mok, T. Stylianopoulos, Y. Boucher, and R. K. Jain. Mathematical modeling of herpes simplex virus distribution in solid tumors: implications for cancer gene therapy. *Clinical Cancer Research*, 15(7):2352–2360, 2009.

[173] E. V. Shashkova, S. M. May, and M. A. Barry. Characterization of human adenovirus serotypes 5, 6, 11, and 35 as anticancer agents. *Virology*, 394(2):311–320, 2009.

[174] Y. Chen, T. DeWeese, J. Dilley, Y. Zhang, Y. Li, N. Ramesh, J. Lee, R. Pennathur-Das, J. Radzyminski, J. Wypych, et al. Cv706, a prostate cancer-specific adenovirus variant, in combination with radiotherapy produces synergistic antitumor efficacy without increasing toxicity. *Cancer Research*, 61(14):5453–5460, 2001.

[175] M. Zaider and G. N. Minerbo. Tumour control probability: a formulation applicable to any temporal protocol of dose delivery. *Physics in Medicine & Biology*, 45(2):279, 2000.

[176] M. Zaider and L. Hanin. Tumor control probability in radiation treatment. *Medical Physics*, 38(2):574–583, 2011.

[177] Y. Kuramoto. *Chemical Oscillations, Waves, and Turbulence*. Springer-Verlag, New York, 1984.

[178] B. Sandstede and A. Scheel. *Spiral Waves: Linear and Nonlinear Theory*, volume 285. AMS, Providence, 2023.

[179] M. Breakspear, S. Heitmann, and A. Daffertshofer. Generative models of cortical oscillations: neurobiological implications of the kuramoto model. *Frontiers in Human Neuroscience*, 190(190):1–14, 2010.

[180] M. O. Gani and T. Ogawa. Spiral breakup in a rd system of cardiac excitation due to front–back interaction. *Wave Motion*, 79:73–83, 2018. ISSN: 0165-2125.

[181] B. Walker, A. Townsend, A. Chudasama, and A. Krause. Visualpde: rapid interactive simulations of partial differential equations. *Bulletin of Mathematical Biology*, 85(11):113, 2023.

[182] J. Awrejcewicz. *Bifurcation and Chaos in Coupled Oscillators*. World Scientific, London, 1991, page 256.

[183] C. Janeway, P. Travers, M. Walport, M. J. Shlomchik, et al. *Immunobiology: the immune system in health and disease*, volume 2. Garland Pub. New York, 2001.

[184] E. Urenda-Cázares, A. Gallegos, and J. E. Macías-Díaz. A mathematical model that combines chemotherapy and oncolytic virotherapy as an alternative treatment against a glioma. *Journal of Mathematical Chemistry*, 58:544–554, 2020.

[185] A. Das, H. K. Sarmah, D. Bhattacharya, K. Dehingia, and K. Hosseini. Combination of virotherapy and chemotherapy with optimal control for combating cancer. *Mathematics and Computers in Simulation*, 194:460–488, 2022.

[186] A. Nguyen, L. Ho, and Y. Wan. Chemotherapy and oncolytic virotherapy: advanced tactics in the war against cancer. *Frontiers in Oncology*, 4:145, 2014.

[187] E. Fraser. Long term respiratory complications of covid-19. *BMJ*, 370, 2020.

[188] A. D. Desai, M. Lavelle, B. C. Boursiquot, and E. Y. Wan. Long-term complications of covid-19. *American Journal of Physiology-Cell Physiology*, 322(1):C1–C11, 2022.

[189] K. Moelling. *Viruses: More Friends than Foes*. World Scientific, Berlin, 2017.

[190] J. Gunawardena. Some lessons about models from Michaelis and Menten. *Molecular Biology of the Cell*, 23(4):517–519, 2012.

[191] J. Malinzi, A. Eladdadi, and P. Sibanda. Modelling the spatiotemporal dynamics of chemovirotherapy cancer treatment. *Journal of Biological Dynamics*, 11(1):244–274, 2017.

[192] J. Malinzi, R. Ouifki, A. Eladdadi, D. F. M. Torres, and K. A. J. White. Enhancement of chemotherapy using oncolytic virotherapy: mathematical and optimal control analysis. *Mathematical Biosciences Engineering*, 15(6):1435–1463, 2018.

[193] C. M. Thirukkumaran and D. G. Morris. *Gene therapy of solid cancers: methods and protocols*. In Springer New York, 2015. Chapter Oncolytic Viral Therapy Using Reovirus.

[194] K. L. Norman, M. C. Coffey, K. Hirasawa, D. J. Demetrick, S. G. Nishikawa, L. M. DiFrancesco, J. E. Strong, and P. W. Lee. Reovirus oncolysis of human breast cancer. *Human Gene Therapy*, 13(5):641–652, 2002.

[195] V Bernstein, S. Ellard, S. Dent, D Tu, M Mates, S. Dhesy-Thind, L Panasci, K. Gelmon, M Salim, X Song, et al. A randomized phase II study of weekly paclitaxel with or without pelareorep in patients with metastatic breast cancer: final analysis of canadian cancer trials group ind. 213. *Breast Cancer Research and Treatment*, 167:485–493, 2018.

[196] B. J. Eigl, K. Chi, D. Tu, S. J. Hotte, E. Winquist, C. M. Booth, C. Canil, K. Potvin, R. Gregg, S. North, et al. A randomized phase II study of pelareorep and docetaxel or docetaxel alone in men with metastatic castration resistant prostate cancer: cctg study ind 209. *Oncotarget*, 9(8):8155, 2018.

[197] C. M. Thirukkumaran, M. J. Nodwell, K. Hirasawa, Z.-Q. Shi, R. Diaz, J. Luider, R. N. Johnston, P. A. Forsyth, A. M. Magliocco, P. Lee, et al. Oncolytic viral therapy for prostate cancer: efficacy of reovirus as a biological therapeutic. *Cancer Research*, 70(6):2435–2444, 2010.

[198] R. A. Adair, K. J. Scott, S. Fraser, F. Errington-Mais, H. Pandha, M. Coffey, P. Selby, G. P. Cook, R. Vile, K. J. Harrington, et al. Cytotoxic and immune-mediated killing of human colorectal cancer by reovirus-loaded blood and liver mononuclear cells. *International Journal of Cancer*, 132(10):2327–2338, 2013.

[199] J. P. Fernandes, F. Cristi, H. E. Eaton, P. Chen, S. Haeflinger, I. Bernard, M. M. Hitt, and M. Shmulevitz. Breast tumor-associated metalloproteases restrict reovirus oncolysis by cleaving the $\sigma 1$ cell attachment protein and can be overcome by mutation of $\sigma 1$. *Journal of Virology*, 93(22):e01380–19, 2019.

[200] F. Graw and A. S. Perelson. Modeling viral spread. *Annual Review of Virology*, 3:555–572, 2016.

[201] L. Ait Mahiout, B. Kazmierczak, and V. Volpert. Viral infection spreading and mutation in cell culture. *Mathematics*, 10(2):256, 2022.

[202] L. A. Mahiout, N. Bessonov, B. Kazmierczak, G. Sadaka, and V. Volpert. Infection spreading in cell culture as a reaction-diffusion wave. *ESAIM: Mathematical Modelling and Numerical Analysis*, 56(3):791–814, 2022.

[203] K. J. A. Excoffon, K. M. Guglielmi, J. D. Wetzel, N. D. Gansemer, J. A. Campbell, T. S. Dermody, and J. Zabner. Reovirus preferentially infects the basolateral surface and is released from the apical surface of polarized human respiratory epithelial cells. *The Journal of Infectious Diseases*, 197(8):1189–1197, 2008.

[204] M. Yamasaki, Y. Kanai, Y. Wakamura, T. Kotaki, S. Minami, R. Nouda, J. A. Nurdin, and T. Kobayashi. Characterization of sialic acid-independent simian rotavirus mutants in viral infection and pathogenesis. *Journal of Virology*, 97(1):e01397–22, 2023.

[205] V. Doceul, M. Hollinshead, L. van der Linden, and G. L. Smith. Repulsion of superinfecting virions: a mechanism for rapid virus spread. *Science*, 327(5967):873–876, 2010.

[206] R. Gallet, S. Kannoly, and I.-N. Wang. Effects of bacteriophage traits on plaque formation. *BMC Microbiology*, 11(1):1–16, 2011.

[207] P. H. Bauer, C. Cui, T. Stehle, S. C. Harrison, J. A. DeCaprio, and T. L. Benjamin. Discrimination between sialic acid-containing receptors and pseudoreceptors regulates polyomavirus spread in the mouse. *Journal of Virology*, 73(7):5826–5832, 1999.

[208] M.-P. Rubio, A. López-Bueno, and J. M. Almendral. Virulent variants emerging in mice infected with the apathogenic prototype strain of the parvovirus minute virus of mice exhibit a capsid with low avidity for a primary receptor. *Journal of Virology*, 79(17):11280–11290, 2005.

[209] A. López-Bueno, M.-P. Rubio, N. Bryant, R. McKenna, M. Agbandje-McKenna, and J. M. Almendral. Host-selected amino acid changes at the sialic acid binding pocket of the parvovirus capsid modulate cell binding affinity and determine virulence. *Journal of Virology*, 80(3):1563–1573, 2006.

[210] A. P. Byrnes and D. E. Griffin. Large-plaque mutants of sindbis virus show reduced binding to heparan sulfate, heightened viremia, and slower clearance from the circulation. *Journal of Virology*, 74(2):644–651, 2000.

[211] A. Z. Kapikian and R. E. Shope. Rotaviruses, reoviruses, coltiviruses, and orbiviruses. *Medical Microbiology. 4th edition*, 1996.

[212] X. Lai and X. Zou. Modeling HIV-1 virus dynamics with both virus-to-cell infection and cell-to-cell transmission. *SIAM Journal on Applied Mathematics*, 74(3):898–917, 2014.

[213] P. Marcato, M. Shmulevitz, D. Pan, D. Stoltz, and P. W. Lee. Ras transformation mediates reovirus oncolysis by enhancing virus uncoating, particle infectivity, and apoptosis-dependent release. *Molecular Therapy*, 15(8):1522–1530, 2007.

[214] C. B. Boyer. *History of Analytic Geometry*. Courier Corporation, 2012.

[215] A. A. Baabdulla and T. Hillen. Oscillations in a spatial oncolytic virus model. *Bulletin of Mathematical Biology*, 86:93, 2024.

Appendix A: Checkerboard Data

Here we present the raw-data as measured in the experiments by Hesung Now, Ju An Park, Woo-Jong Kim, Sungjune Jung, and Joo-Yeon Yoo. Table A.1 and A.2 represent the kinetics of influenza A virus separately in the homogeneous cell populations in a first and second experiment with triplicated data sets. In both experiments, the CT (HA) gene expression, CT (mGAPDH) gene expression, ΔCT, $\Delta\Delta CT$ and RQ have been measured for weak and strong infectivity cells at t=0, t=6, t=12 and t=24 hours respectively. See equations (2.1,2.2,2.3). The viral load is represented by the RQ value, where the RQ is the relative quantification as we mentioned in section 2.2.

Table A.3, represents the viral load for the checker board experiments at one day with three independent samples. In the micro-pattering experiment, the CT (HA) gene expression, CT (GAPDH) gene expression, RQ and the average RQ (average viral load) have been measured in the mix plate, 1.5 mm, 3 mm and 5 mm, respectively.

Sample name	**CT (HA) (Target gene)**	**CT (mGAPDH) (Reference gene)**	**ΔCT**	**ΔΔCT**	**RQ**
Weak 0h-1	32.906	13.687	N.D	N.D	N.D
Weak 6h-1	22.480	16.430	6.0500	0.1090	0.9272
Weak 12h-1	20.533	15.500	5.0330	-0.9080	1.8764
Weak 24h-1	20.008	14.719	5.2890	-0.6520	1.5713
Weak 0h-2	33.670	14.912	N.D	N.D	N.D
Weak 6h-2	22.681	16.685	5.9960	0.0550	0.9626
Weak 12h-2	20.690	15.757	4.9330	-1.0080	2.0111
Weak 24h-2	20.184	14.417	5.7670	-0.1740	1.1282
Weak 0h-3	33.175	15.184	N.D	N.D	N.D
Weak 6h-3	22.137	16.360	5.7770	-0.1640	1.1204
Weak 12h-3	20.611	15.687	4.9240	-1.0170	2.0237
Weak 24h-3	19.864	13.947	5.9170	-0.0240	1.0168
Strong 0h-1	33.714	14.757	N.D	N.D	N.D
Strong 6h-1	21.071	15.869	5.2020	-0.7390	1.6690
Strong 12h-1	9.745	15.780	3.9650	-1.9760	3.9340
Strong 24h-1	17.433	13.385	4.0480	-1.8930	3.7141
Strong 0h-2	34.002	13.825	N.D	N.D	N.D
Strong 6h-2	20.420	15.398	5.0220	-0.9190	1.8908
Strong 12h-2	19.875	15.901	3.9740	-1.9670	3.9095
Strong 24h-2	18.039	14.757	3.2820	-2.6590	6.3160
Strong 0h-3	34.402	14.588	N.D	N.D	N.D
Strong 6h-3	20.254	15.299	4.9550	-0.9860	1.9807
Strong 12h-3	19.902	15.728	4.1740	-1.7670	3.4035
Strong 24h-3	18.447	14.939	3.5080	-2.4330	5.4002

Table A.1: The growth rate of influenza A virus in weak and strong population in first experiment with three data sets for one day. N.D means not determined

Sample name	**CT (HA) (Target gene)**	**CT (mGAPDH) (Reference gene)**	**ΔCT**	**ΔΔCT**	**RQ**
Weak 0h-1	N.D	13.927	N.D	N.D	N.D
Weak 6h-1	24.539	19.245	5.2940	-0.3600	1.2834
Weak 12h-1	18.613	15.948	2.6650	-2.9890	7.9390
Weak 24h-1	20.678	14.778	5.9000	0.2460	0.8432
Weak 0h-2	N.D	14.059	N.D	N.D	N.D
Weak 6h-2	23.796	17.951	5.8450	0.1910	0.8760
Weak 12h-2	19.146	16.261	2.8850	-2.7690	6.8164
Weak 24h-2	20.581	15.002	5.5790	-0.0750	1.0534
Weak 0h-3	37.975	14.316	N.D	N.D	N.D
Weak 6h-3	23.748	17.925	5.8230	0.1690	0.8895
Weak 12h-3	19.805	17.057	2.7480	-2.9060	7.4950
Weak 24h-3	20.570	14.960	5.6100	-0.0440	1.0310
Strong 0h-1	N.D	14.942	N.D	N.D	N.D
Strong 6h-1	21.493	16.308	5.1850	-0.4690	1.3841
Strong 12h-1	16.076	14.713	1.3630	-4.2910	19.576
Strong 24h-1	15.642	14.052	1.5900	-4.0640	16.726
Strong 0h-2	36.907	14.285	N.D	N.D	N.D
Strong 6h-2	21.513	16.950	4.5630	-1.0910	2.1302
Strong 12h-2	16.607	15.885	0.7220	-4.9320	30.527
Strong 24h-2	16.010	13.580	2.4300	-3.2240	9.3437
Strong 0h-3	N.D	13.836	N.D	N.D	N.D
Strong 6h-3	20.211	15.401	4.8100	-0.8440	1.7950
Strong 12h-3	15.965	14.355	1.6100	-4.0440	16.495
Strong 24h-3	15.060	13.967	1.0930	-4.5610	23.605

Table A.2: The growth rate of influenza A virus in weak and strong population in second experiment with three data sets for one day. N.D means not determined

Size of inner square	**CT (HA)**	**CT (GAPDH)**	**RQ**	**Average RQ**
Mix-1	15.366	15.157	1.0669	
Mix-2	14.849	15.013	1.3816	1.2957
Mix-3	14.695	14.917	1.4387	
1.5 mm-1	15.148	14.845	1.0000	
1.5 mm-2	15.172	15.395	1.4396	1.3305
1.5 mm-3	15.461	15.793	1.5520	
3 mm-1	14.621	15.638	1.7034	
3 mm-2	15.266	15.087	1.2569	1.9304
3 mm-3	14.440	15.294	2.8308	
5 mm-1	14.191	15.060	2.2519	
5 mm-2	14.948	16.609	3.8978	3.3996
5 mm-3	14.547	16.262	4.0492	

Table A.3: The influenza A viral load on the micro-patterning for the different inner square sizes with three samples at one day.